

POLARIZATION MODE DISPERSION ANALYSIS VIA SPECTRAL
POLARIMETRY AND HIGH-ORDER CORRELATIONS

A Thesis

Submitted to the Faculty

of

Purdue University

by

Li Xu

In Partial Fulfillment of the

Requirements for the Degree

of

Master of Science in Electrical and Computer Engineering

August 2006

Purdue University

West Lafayette, Indiana

To my mother Maorong and my husband Zhi. Thank you for all your love and support.

ACKNOWLEDGMENTS

I would like to thank Prof. Weiner and Prof. Webb for the research opportunities and the valuable advice they provided me, Dr. Dan Leaird for his useful suggestion and help on the experiments, and group mates Dr. Mehmetcan Akbulut, Xiang Wang, Zhenyu Wang and Houxun Miao for all their educational discussions.

TABLE OF CONTENTS

	Page
LIST OF TABLES.....	vi
LIST OF FIGURES.....	vii
LIST OF ABBREVIATIONS.....	xiii
ABSTRACT.....	xv
1. INTRODUCTION.....	1
2. PMD THEORY.....	3
2.1 PMD Fundamental.....	3
2.1.1 Polarization of Light Beam.....	4
2.1.2 Birefringence in Optical Fiber.....	7
2.1.3 Polarization-Mode Coupling.....	10
2.1.4 Principle State of Polarization.....	11
2.1.5 PMD Vector.....	12
2.2 PMD in Polarization Maintaining Fibers (PMF).....	14
2.2.1 One-piece PMF.....	15
2.2.2 Two-piece PMF.....	15
2.2.3 Three-piece PMF.....	17
2.3 Multi-input SOP Method to Measure PMD Vector.....	20
3. EXPERIMENTAL SETUP.....	23
3.1 Multi-SOP producer and SOP component selector.....	24
3.2 Spatial Dispersion.....	26
4. EXPERIMENT RESULTS AND DATA PROCESSING.....	30
4.1 SOP Measurement.....	30
4.2 Data fitting and differential size choosing.....	34
4.2.1 Data fitting.....	35
4.2.2 Differential size choosing.....	37
4.2.3 Simulation.....	38

	Page
4.3 PMD Vector calculation.....	43
4.4 PMD Vector measurement result.....	44
4.4.1 Measurement of differential refractive index Δn	45
4.4.2 One-piece PMF.....	45
4.4.3 Two-piece PMF.....	51
4.4.4 Three-piece PMF.....	56
4.5 Discussion.....	58
4.5.1 Measurement efficiency.....	58
4.5.2 Independence on input SOP.....	58
4.5.3 Inter-pixel cross talk.....	58
4.5.4 PMD measurement limitation.....	59
4.5.5 Applications.....	59
5. RESEARCH ON PMD BY HIGH-ORDER CORRELATIONS.....	60
5.1 Introduction.....	60
5.1.1 Stochastic properties of PMD.....	60
5.1.2 Motivations.....	61
5.2 PMD simulation.....	62
5.3 Second-order correlations.....	64
5.3.1 Intensity of the x-direction component field.....	64
5.3.2 Output PMD vector.....	65
5.3.3 Output SOP.....	67
5.4 The Properties of the X-direction component of the Output Optical field.....	69
5.4.1 Simulation.....	69
5.4.2 pdf of x-direction component field.....	70
5.4.3 Experiment.....	73
6. CONCLUSION.....	78
REFERENCES.....	79

LIST OF TABLES

Table	Page
2.1 SOPs of different kinds.....	4
2.2 Stokes vectors for different SOPs.....	6
4.1 Compare the PMD measurement results and the estimation.....	54
5.1 The details of the PMF sections in the PMD emulator.....	75

LIST OF FIGURES

Figure	Page
2.1 Poincarè sphere.(Adapted from [9])	7
2.2 (a) Ideal fiber (b) Internal perturbation (c) External perturbation.....	8
2.3 (a) decompose a SOP to an orthogonal SOP pair. (b)SOP on a circle on the Poincarè sphere	9
2.4 Model long fibers by concatenation of wave plates with birefringence axes oriented randomly along the fiber length	10
2.5 (a) output principle state of polarization for an ideal short fiber is the birefringent axis and is the same for all frequency. (b) output PSP of a certain frequency for a long fiber.....	12
2.6 Concatenation rule of PMD vectors.....	14
2.7 (a) Concatenation of two-pieces of PMF with angle θ between two slow axes. (b) Concatenation of two PMD vector.....	16
2.8 the output SOP for a certain frequency changes from A to B if the length of one-piece PMF increases by half of its beat length.....	17
2.9 (a) Concatenation of three pieces of PMF. (b) The concatenation rule of the total PMD vector for three-piece PMF. (c) The total PMD vector of three-piece PMF for a certain frequency. (d) The total PMD vector of three PMF for another frequency	18
2.10 (a) the total PMD vector of 3-piece PMF for a certain frequency. (b) Compare to (a), only without the rotation operation , the total DGD remains the same with (a). (c) Using the operations in (b), the end of total PMD vector is on the circle.....	19

Figure	Page
2.11 The simulation result for the total DGD of three-piece PMF. In case 1 (solid curve), the length of each piece of PMF is 50cm, 80cm and 60cm, the slow axis angle offset between the first and the second PMF is 45° , and between the second and the third -50° . The beat length of the PMF is 3.7mm. We increase the length of the second PMF by half of the beat length to get the case 2 (dashed curve)	20
2.12 (a) Two set of output $SOP(\omega)$ on the Poincarè sphere for two different fixed input SOP. (b) If the frequency increases by a small span, the change of the output SOP at certain frequency is orthogonal to the output PSP of this frequency. This also works for other output SOP sets. (c) Extract DGD and output PSP from the output $SOP(\omega)$ sets	21
3.1 The PMD measurement setup	23
3.2 The fast axis of the FLC retarders: (a) +5v voltage applied. (b) +5v voltage applied	24
3.3 The truth table of the multi-SOP producer	25
3.4 The truth table for the SOP component selector	25
3.5 The spatial dispersion setup	26
3.6 Light diffracted by a grating.....	27
3.7 (a) the light is diffracted by the grating. (b) The concave lens focuses the beams on its focus plane	28
4.1 Use single frequency input to test the beam size on the CCD array. The FWHM of the intensity is about 2 pixels, or 200um.....	31
4.2 The measurement of 135° SOP for all frequencies (on Poincarè sphere): (a) before calibration. (b) After calibration.....	32
4.3 The output SOP measurement result for a short SMF without PMD. (a) The intensity of four SOP components vs. CCD pixel number. (b) The output SOP on the Poincarè sphere.....	32

Figure	Page
4.4 The output SOP measurement of one-piece PMF with 96.9cm length. (a) The intensity of four SOP components vs. CCD pixel number. (b) the output SOP traces a circle on the Poincarè sphere. (c) Zoom in the output SOP on the Poincarè sphere to see the differential SOP vector ΔSOP	33
4.5 The output SOP measurement of one-piece PMF with 96.9cm length. (a) the output SOP traces a small circle on the Poincarè sphere. (b) Zoom in the output SOP on the Poincarè sphere to see the differential SOP vector ΔSOP	34
4.6 (a) fit a polynomial of degree 1 to data. (b) fit a polynomial of degree 1 to every 4 continuous points	35
4.7 Use two angles to express SOP. (a) Angle ϕ and θ of a certain SOP. (b) The relation between ϕ, θ and Stokes vector	36
4.8 Apply data fitting to angle ϕ and θ respectively. The points are measured SOP on the Poincarè sphere, and black curve is the fitting curve ...	37
4.9 $\Delta SOP(\omega_0)$ for different differential sizes.....	37
4.10 The effect of data fitting and differential size choosing on PSP calculation. The size of the noise added: $error = 0.2$. The points on a circle are the theoretical PSPs. Others are from PMD calculation. (a) no data fitting, smallest differential size $2\Delta\omega$ (M=2). (b) with data fitting (N=10), smallest differential size $2\Delta\omega$ (M=2). (c) No data fitting, differential size $10\Delta\omega$ (M=10). (d) The PSP error parameter D (°) of (a), (b), (c).....	39
4.11 PSP calculated from output SOP with no error. (a) N=10, and M=2 (smallest differential size). (b) no data fitting, M=10.....	40
4.12 Plot of D' vs. $error$	41

Figure	Page
4.13 PSP calculated from measured output SOP. The fiber under test and frequency span as well as the sample numbers is the same with those in the simulation. (a) No data fitting and smallest differential size. (M=2). (b) N=10, M=2. (c) No data fitting and M=10. (d)N=10 and M=2 (PSP in (b) and (c) are also plotted in this figure).....	42
4.14 The component s_1 of output SOP Stokes vector (s_1, s_2, s_3) vs. wavelength.....	45
4.15 (a) Output SOP measured. (b)Output SOP after data fitting. (N=10).....	46
4.16 PMD calculated from fitting data (N=10) with differential size $2\Delta\omega$. (a)PSP (b) DGD.....	47
4.17 PMD calculated from fitting data (N=10) with larger differential size ($10\Delta\omega$). (a)PSP (b) DGD.....	48
4.18 Output PSP for one-piece PMF with length $l = 40.9cm$ (a) measured output SOP (b) Output SOP after data fitting (N=10).....	48
4.19 PMD calculated from fitting data (N=10). (a)PSP (b) DGD.	49
4.20 PMD calculated from fitting data (N=10) with larger differential size ($10\Delta\omega$). (a)PSP (b) DGD.....	49
4.21 PMD calculated from fitting data (N=10). (a)PSP (b) DGD.....	50
4.22 PMD calculated from fitting data (N=10) with larger differential size ($10\Delta\omega$). (a)PSP (b) DGD.....	51
4.23 (a) the PMD concatenation rule.(b)output PSP vs. frequency for two piece PMF traces a circle on the Poincare sphere.....	51
4.24 PMD vector measurement for PMF No.3 (70cm+70cm). (a)PSP (b) DGD.	54
4.25 PMD vector measurement for fiber No 1~No.5. (a) PSP (b)DGD.	55
4.26 PSP measurement result for Fiber No.1 and No.3.	55

Figure	Page
4.27 Result for three-piece PMF (a)measured output SOP (b) output PSP (c) DGD.....	57
5.1 The statistical properties of PMD vector extracted from simulation.....	63
5.2 (a)x-direction component intensity spectrum for $\Delta\tau = 3ps, 6ps$ respectively. (b)Second-order correlation of the x-direction component field intensity for $\Delta\tau = 1ps, 3ps, 6ps$ respectively.	65
5.3 Figure 5.3 The second-order correlations. (a) $\langle \tau_1(\omega)\tau_1(\omega + \Delta\omega) \rangle$ (τ_1 is the component of the PMD vector in stokes space) (b) $\langle \hat{\tau}(\omega) \bullet \hat{\tau}(\omega + \Delta\omega) \rangle$ (the second-order correlation on the dot product of PMD vectors.) (c) simulation and theoretical result for $\langle \hat{\tau}(\omega) \bullet \hat{\tau}(\omega + \Delta\omega) \rangle$ (d) the fluctuations on the base.	66
5.4 The second-order correlations. (a) $\langle S_1(\omega)S_1(\omega + \Delta\omega) \rangle$ (S_1 is the component of the SOP vector in stokes space) (b) $\langle \hat{S}(\omega) \bullet \hat{S}(\omega + \Delta\omega) \rangle$ (the second-order correlation on the dot product of SOP vectors.) (c) Simulation and theoretical result for $\langle \hat{S}(\omega) \bullet \hat{S}(\omega + \Delta\omega) \rangle$	68
5.5 Simulation on the properties of the output x-direction component field. (a) pdf of the field: $P_x(x), x = E_r \text{ or } E_i$ (b) pdf of the intensity: $P_I(I)$ (c) pdf of the phase: $P_\theta(\theta)$	70
5.6 (x,y) is distributed in the unit circle.....	71
5.7 pdf of the field. (The dot and square are from the simulation, the solid line is from the derivation.).....	72
5.8 The intensity of x-direction component field measurement setup.	73
5.9 PMD emulator.....	74

Figure	Page
5.10 Simulation on the emulator	
(a)one output SOP trajectory	
(b)twenty output SOP trajectories.....	74
5.11 The intensity spectrum of the output x-direction component field (The blue solid curve and red dashed curve are measurements for two different emulator states)..	76
5.12 The histogram of the output x-direction component intensity.....	77
5.13 The second-order correlation of the x-direction component output field intensity.....	77

LIST OF ABBREVIATIONS

ASE	Amplified Spontaneous Emission
BER	Bit Error Rate
CCD	Charge Coupled Device
DGD	Differential Group Delay
DUT	Device Under Test
FLC	Ferroelectric Liquid-Crystal
FUT	Fiber Under Test
FWHM	Full Width at Half Maximum
HWP	Half Wave Plate
LHC	Left-Hand Circular
JME	Jones Matrix Eigenanalysis
MMM	Müller Matrix Method
OSA	Optical spectrum Analyzer
PC	Polarization Controller
pdf	Probability Density Function
PDL	Polarization Dependent Loss
PMD	Polarization Mode Dispersion
PSP	Principle State of Polarization

PMF	Polarization Maintaining Fiber
QWP	Quarter Wave Plate
RHC	Right-Hand Circular
rms	Root Mean Square
SMF	Single Mode Fiber
SOP	State of Polarization
WDM	Wavelength Division Multiplexing

ABSTRACT

Xu, Li, M.S.E.C.E., Purdue University, August 2006. Polarization Mode Dispersion Analysis via Spectral Polarimetry and High-Order Correlations. Major Professors: Andrew M. Weiner and Kevin J. Webb.

Polarization Mode Dispersion (PMD) is a fundamental phenomenon that limits the bandwidth of high-speed optical fiber communication systems. It arises from the residual birefringence of the optical fiber and the random orientation of the birefringence axes. PMD causes a differential group delay between different polarizations. If the delay is comparable to a significant fraction of the bit period, adjacent bits may overlap, leading to an increase in bit error rate and decrease in system performance.

PMD monitoring is essential in PMD mitigation and compensation schemes for improving system performance. PMD is fully described by the PMD vector as a function of frequency. In our work, we demonstrate an efficient scheme to measure this vector. We use fast switching ferroelectric liquid crystals functioning as variable retarders to produce multiple input states of polarization (SOP), and measure the output SOP with our fast wavelength-parallel polarimeter. Then, we calculate the PMD vector from the differential output SOP vector. This technique allows PMD monitoring on a millisecond scale.

In the second part of this thesis, we demonstrate a statistical study of PMD. The stochastic nature of PMD arises from the change in environmental factors such as fiber stress and temperature variations. Here, we investigate to study PMD statistics by second order and third order frequency correlations and extract post-PMD signal phase. Our simulations show that the second order correlation on the output SOP or PSP contains the information on the mean differential group delay. From both simulation and experimental results we study the properties of the output optical field and show that an arbitrary component (for example, x-direction component) of the output optical field is not zero-mean circular complex Gaussian distributed. Based on this, we conclude that we cannot obtain phase of the intensity temporal response from third-order correlation on the field intensity of a certain component.

1. INTRODUCTION

Polarization mode dispersion (PMD) in optical fiber has become an important limitation in the high-capacity and long-haul optical communication systems. Usually the mean differential group delay (DGD) less than one tenth of the bit period is allowed. For modern low PMD fibers, the mean DGD coefficient is less than $0.1ps/\sqrt{km}$, which means that it only allows 5~10 Gb/s over transoceanic distances (up to 10,000 km) [1]. With the explosive development of current internet technique and the information exchange among personal computers, it is a must to compensate PMD and gain higher capacity in the optical communication systems. The knowledge of PMD has become a key issue in the design of the systems. In this thesis, we study PMD via a spectral polarimetry and high-order correlations.

In our work, we develop a scheme to measure the instantaneous PMD vector as a function of frequency, which fully describe PMD, using our fast wavelength-parallel polarimeter [2]. In this scheme, we produce four different input states of polarization (SOP) (each time the SOP is fixed for all frequencies) to the device under test by the fast switching ferroelectric liquid crystal cells, and measure the four output SOP sets. The PMD vector is calculated from the output SOP sets [3, 4]. This method measures 128 frequencies in parallel in a milliseconds scale. Moreover, the measurement is independent of the input SOP, unlike JME method [5], which gives it potential to be applied in the long-haul optical fiber communication systems. In addition to the measurement scheme, we also perform PMD simulations and investigate to study PMD by high-order correlations. We show that second-order correlation on several output parameters, such as x-direction component field intensity, output PMD vector, and output SOP, contains the information of mean DGD. We also study the properties of the output x-direction component optical field. From these properties, we conclude that the third-order correlation [6, 7] on the x-direction component of the output optical field intensity doesn't give the phase of the intensity temporal response.

This thesis includes 6 chapters. Except for the introduction in chapter 1, firstly we introduce the basic PMD theory in chapter 2, including PMD fundamentals (the polarization of light beam, the birefringence in optical fiber, polarization mode coupling,

and the PMD vector), PMD in polarization maintaining fiber (PMF) (1-piece, 2-piece, and 3-piece PMF), and our PMD vector measurement method. Then in chapter 3, we introduce our experimental setup for PMD vector measurement. The measurement result and the data processing details are shown in chapter 4. In chapter 5, we use second-order correlations on the output x-direction component intensity, output SOP (State of Polarization), and output PMD vector to study PMD in simulation. We also investigate and find that the third-order correlation on the x-direction field intensity does not give the phase of the temporal intensity response. Finally, in chapter 6, we make a short conclusion of this thesis.

2. PMD THEORY

The PMD basics are introduced in section 2.1, including polarization states of light beam, the two origins of PMD in optical fiber (birefringence and polarization mode coupling), the concept of principle state of polarization, and the PMD vector. We discuss in section 2.2 the PMD vector of PMF sections (1-piece, 2-piece and 3-piece), which are chosen to be the device under test (DUT) in our experiment. The PMD measurement fundamentals of our scheme are introduced in section 2.3.

2.1 PMD Fundamental

The polarization state is an important parameter of light beams. A device can change this polarization state. People use two different methods to describe the polarization state and the effect of a device in changing polarizations: Jones calculus (Jones vector and Jones matrix), and Stokes space (Stokes vector and Muller matrix)[8]. The details are shown in section 2.1.1. In optical fiber, the existence of the birefringence makes the two polarizations of the light beam lose their degeneracy in propagation constant, and thus cause the differential group delay (DGD) between different polarization states. Section 2.1.2 discusses the birefringence in optical fiber and its effect on polarization. Polarization mode coupling is another cause of polarization mode dispersion, as shown in section 2.1.3. This coupling together with birefringence make the PMD complicated in long fibers. However, the concept of principle state of polarization describes the PMD in a simple way. This important concept is introduced in section 2.1.4. People use PMD vector as a function of frequencies to fully describe PMD. Section 2.1.5 discusses the properties of PMD vector.

2.1.1 Polarization of Light Beam

As the light beam propagates in the z direction, the electric field, which lies in the x-y plane, can be viewed as the superposition of two orthogonal linearly polarized fields: x and y components. In time domain, for any point in space, the electric field is [8]:

$$\vec{E}(t) = \vec{a}_x E_{x0} \cos(\omega t + \phi_x) + \vec{a}_y E_{y0} \cos(\omega t + \phi_y) \quad (2.1)$$

In the above equation, E_{x0} and E_{y0} are the amplitudes of the x and y component respectively, while ϕ_x and ϕ_y are the phase of these two components. We can see that the electric field varies with time, but the variations are different due to the difference in amplitudes and phases of the components. We use State of Polarization (SOP) to name this variation. In the case $\phi_x = \phi_y$, the field direction, which is determined by the ratio of E_{x0} and E_{y0} , is constant, and we get linear polarization. In the case $\phi_x \neq \phi_y$, we get elliptical polarization, which means that the end of the electric field vector evolves on an ellipse in the x-y plane with time. If $\phi_x > \phi_y$, the ellipse is left-handed, which means the evolution is counter-clockwise, while if $\phi_x < \phi_y$, the ellipse is right-handed, which means the evolution is clockwise. (We always assume that the observer looks towards the propagation direction of the light.) Table 2.1 summarizes the SOPs in different cases.

Table 2.1
SOPs of different kinds

condition	$\phi_x = \phi_y$	$\phi_x > \phi_y$	$\phi_x < \phi_y$
SOP	linear polarization, $\tan \theta = \frac{E_{y0}}{E_{x0}}$, (θ is the field direction from +x axis)	Left-handed elliptical polarization.	Right-handed elliptical polarization.
		If $\phi_x = \phi_y + \frac{\pi}{2}$ and $E_{x0} = E_{y0}$, Left- hand circular (LHC)	If $\phi_y = \phi_x + \frac{\pi}{2}$ and $E_{x0} = E_{y0}$, Right- hand circular (RHC)

Jones calculus is a simple and clear way to describe SOP and the media where the light propagate and its SOP evolves. Jones calculus includes 1×2 Jones vectors which describe the SOP, and 2×2 Jones matrices which describe the media. In Jones calculus, the electric field of a certain SOP is written as:

$$E = \begin{bmatrix} E_x \\ E_y \end{bmatrix} = \begin{bmatrix} E_{x0} e^{j\phi_x} \\ E_{y0} e^{j\phi_y} \end{bmatrix} \quad (2.2)$$

If we normalize the Jones vector, all the SOP can be written as:

$$\begin{bmatrix} \cos \theta \\ \sin \theta e^{j(\phi_y - \phi_x)} \end{bmatrix} \quad (2.3)$$

The normalized Jones vector for horizontally and vertically linear polarization and the right-hand and left-hand circular polarization are:

$$\begin{bmatrix} 1 \\ 0 \end{bmatrix}, \begin{bmatrix} 0 \\ 1 \end{bmatrix}, \frac{1}{\sqrt{2}} \begin{bmatrix} 1 \\ j \end{bmatrix}, \frac{1}{\sqrt{2}} \begin{bmatrix} 1 \\ -j \end{bmatrix} \quad (2.4)$$

If the two SOPs E_1 and E_2 are orthogonal, this means these two Jones vector satisfies: $\text{Dot}(E_1, E_2^*) = 0$, where E_2^* is the conjugate of E_2 . Obviously, Horizontal linear polarization and vertical linear polarization, RHC and LHC are two orthogonal pairs. Any SOP can be decomposed to the combination of two orthogonal SOP pairs.

When the light propagate in a media, its SOP evolves. We use Jones matrix to describe how this media changes the input SOP into the output SOP. The relationship is :

$$\begin{bmatrix} E_{xout} \\ E_{yout} \end{bmatrix} = \begin{bmatrix} J_{11} & J_{12} \\ J_{21} & J_{22} \end{bmatrix} \begin{bmatrix} E_{xin} \\ E_{xout} \end{bmatrix} \quad (2.5)$$

where $J = \begin{bmatrix} J_{11} & J_{12} \\ J_{21} & J_{22} \end{bmatrix}$ is Jones Matrix. For example, here we introduce two simple but

frequently used Jones matrix. One is for the retarder (or waveplate) which has the fast axis at x axis:

$$R(\phi) = \begin{bmatrix} e^{j\frac{\phi}{2}} & 0 \\ 0 & e^{-j\frac{\phi}{2}} \end{bmatrix},$$

it retard the phase of y field component by ϕ . The other one is for rotating the coordinates by angle θ relative to the +x axis:

$$S(\theta) = \begin{bmatrix} \cos \theta & \sin \theta \\ -\sin \theta & \cos \theta \end{bmatrix}$$

For a complicated or composite optical device, to get its Jones matrix, we can just multiply the Jones matrix of the simple operations or the individual elements in order. In a system with no loss, the Jones matrix can be simply expressed as the products of the Jones matrix for retarders and axis rotations.

Similar to Jones calculus, stokes vector and Müller matrix in stokes space is another way to describe SOP and the media. Stokes parameters (s_0, s_1, s_2, s_3) are measurable parameters [9,18]:

$$\begin{aligned}
 s_0 &= I_0 + I_{90} = I_{45} + I_{135} = I_{RHC} + I_{LHC} = E_{x0}^2 + E_{y0}^2 \\
 s_1 &= I_0 - I_{90} = E_{x0}^2 - E_{y0}^2 \\
 s_2 &= I_{45} - I_{135} = 2E_{x0}E_{y0}\cos(\phi_y - \phi_x) \\
 s_3 &= I_{RHC} - I_{LHC} = 2E_{x0}E_{y0}\sin(\phi_y - \phi_x)
 \end{aligned} \tag{2.6}$$

where I_0 is the intensity of the horizontal component, and the meaning of I_{90} , I_{45} , I_{135} , I_{RHC} and I_{LHC} are similar. The stokes vector is the normalization of the vector (s_1, s_2, s_3) . This vector is always plotted on the unit sphere known as Poincarè sphere in 3-D space. By this tool, SOP can be visualized and conveniently analyzed. Figure 2.1 shows the SOPs denoted by different points on Poincarè sphere. (In this figure, the $+s_3$ axis points downward, but in the rest part of this thesis, we choose this axis upward.) Table 2.2 shows the stokes vector for some special SOPs.

Table 2.2
Stokes vectors for different SOPs

(s_1, s_2, s_3)	SOP
$(1, 0, 0)$	Horizontal linear polarization
$(-1, 0, 0)$	Vertical linear polarization
$(0, 1, 0)$	45 degree linear polarization
$(0, -1, 0)$	135 degree linear polarization
$(0, 0, 1)$	Right-hand circular polarization
$(0, 0, -1)$	Left-hand circular polarization
$s_3 = 0$	Linear polarization
$s_3 < 0$	Left-hand elliptical polarization
$s_3 > 0$	Right-hand elliptical polarization

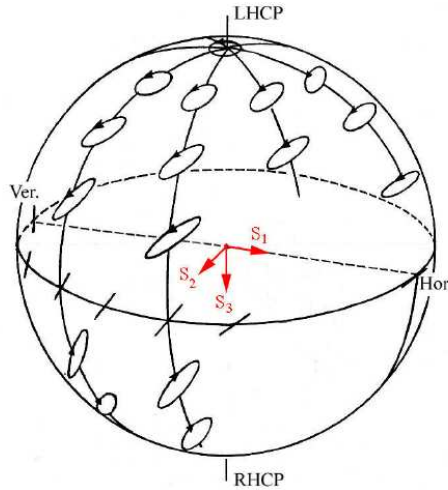


Figure 2.1 Poincaré sphere. (Adapted from [9])

On the Poincaré sphere, all the linear polarizations lie on the equator. The north pole and the south pole are LHC and RHC respectively. SOPs are left-hand elliptical on the north of the sphere, and right-hand elliptical on the south. Every pair of orthogonal SOPs are the two points symmetric about the center of the sphere.

In stokes space, a 3×3 matrix called Müller matrix describe the media's effect on the SOP evolution.

Jones calculus and the stokes vector have their own advantage comparing to each other. Jones vector and matrix are smaller in size, and they describe the field directly. However, Jones vector can only describe polarized light, while stokes vector can also describe partially polarized light and unpolarized light. Moreover, visualization is also an advantage of stokes space.

2.1.2 Birefringence in Optical Fibers

In optical fiber communication systems, although we call the optical fiber as single mode fiber (SMF), there actually exist two orthogonally polarized HE₁₁ modes[10,11]. If the fiber has not only perfectly symmetric core and cladding geometry but also perfectly isotropic material (as shown in Figure 2.2 (a)), these two modes have the same group delay. However, in the real world, symmetry of the fibers is broken according to the internal perturbation and/or the external perturbation. So that the degeneracy of the two orthogonally polarized modes is broken: birefringence exists, or in other words the phase and group velocities of the two modes are different.

The internal perturbation comes from the manufacturing process and has two kinds [1]. One kind is that the core is elliptical (as shown in Figure 2.2 (b)). In this case, geometric birefringence arises and the two HE₁₁ modes have different propagation constants. The other kind is that though the core is circular, there exist asymmetric internal stress (as shown in Figure 2.2 (c)), which causes the material density difference, and thus the difference of the propagation constant of the two modes.

The external perturbation [1,10] (as shown in Figure 2.2 (c)) includes Lateral stress, bending, and twist. The first two have the similar effects as the internal asymmetric stress, so they cause linear birefringence by introducing material density difference. Unlike all the other perturbation, fiber twist creates circular birefringence. We only discuss linear birefringence in this thesis.

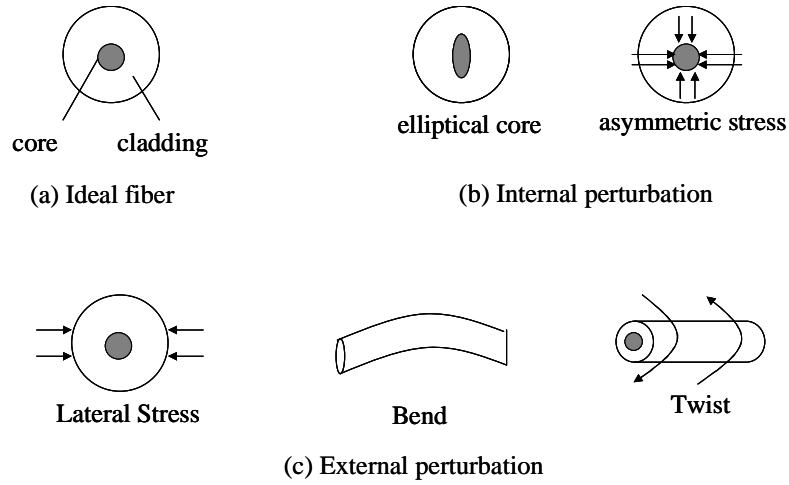


Figure 2.2 (a) Ideal fiber (b) Internal perturbation (c) External perturbation

The birefringence of single mode fibers is on the order of $10^{-5} \sim 10^{-7}$ [1,10], which is small compared to the refractive index of the core (~ 1.5), but in the long communication optical fiber it can cause large differential group delay between fast mode and slow mode compare to the pulse width of optical signal. The perturbation on single mode fiber is randomly distributed along the length. Ideally, in a short section of single mode fiber, the birefringence can be considered uniform. In this case, it can be viewed as a wave plate. The slow mode and the fast mode have difference in the propagation constant:

$$\Delta\beta = \beta_{slow} - \beta_{fast} = \frac{\omega n_{slow}}{c} - \frac{\omega n_{fast}}{c} = \frac{\omega \Delta n}{c} \quad (2.7)$$

Where c is the speed of light, ω is the angular frequency of light, and n_{slow} and n_{fast} are the effective refractive index of the slow mode and the fast mode respectively. If the input wave is linearly polarized along the birefringence axis, only one mode is excited, and the SOP is maintained along the length of the fiber. Otherwise, both of the fast and slow modes are excited, and the input SOP is decomposed to the two modes which are orthogonal. As shown in Figure 2.3 (a):

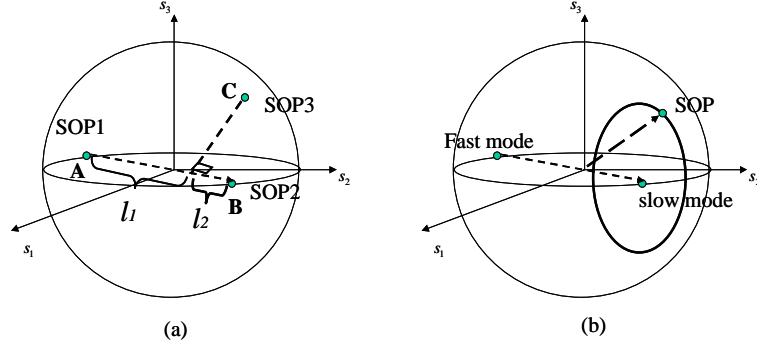


Figure 2.3 (a) decompose a SOP to an orthogonal SOP pair. (b) SOP on a circle on the Poincaré sphere.

Point A and point B denote the two orthogonal modes SOP1 and SOP2 on Poincaré sphere, and they are symmetric about the sphere center. Point C denotes an arbitrary SOP3. If we project C on the section AB, and cut it into two sections with length l_1 and l_2 . We get this relation: $E_3 = a_1 e^{j\phi} E_1 + a_2 e^{j\phi} E_2$, and $\frac{a_1^2}{a_2^2} = \frac{l_2}{l_1}$, where the Jones

vector of SOP3 is written as the combination of this orthogonal pair. The intensity ratio of each components is determined by the ratio of l_1 and l_2 . With fixed intensity ratio, if the phase difference of the two components changes, SOP3 evolves on a circle, as shown in Figure 2.3 (b). We know that as the two excited mode propagate along the fiber, the phase difference between them increases while the intensity ratio remains the same. So the SOP evolves on the circle with line AB as its axis and return to its original SOP after a length named “Beat Length”[10] along the fiber.

The beat length is:

$$L_B = \frac{2\pi}{\beta_{slow} - \beta_{fast}} = \frac{2\pi}{\omega \Delta n / c} = \frac{\lambda}{\Delta n} \quad (2.8)$$

For 1550nm wavelength and $\Delta n \sim 10^{-7}$, the beat length is $\sim 15m$, and for polarization maintaining fiber (PMF) with $\Delta n \sim 4 \times 10^{-4}$, the beat length is about 3mm.

If the input SOP is fixed, but the light frequency varies, the output SOP for a fixed length short fiber evolves in a similar way. In the case that only one mode is excited, then the output SOP from this ideal short birefringence maintains the same with the input SOP for all frequencies. While when two modes are excited, the output SOP traces the circle on the Poincarè sphere surface as the frequency is varied. The circle also has line AB as its axis.

For this ideal short fiber, considering the two modes in time domain, there is differential group delay (DGD) $\Delta\tau$ between them. The birefringence is considered uniform along the fiber length, and the DGD is proportional to the fiber length. Naturally, the polarization mode dispersion (PMD) is usually characterized as:

$$\frac{\Delta\tau}{L} = \frac{d\beta_{slow}}{d\omega} - \frac{d\beta_{fast}}{d\omega} = \frac{d}{d\omega} \left(\frac{\Delta n \omega}{c} \right) = \frac{\Delta n}{c} + \frac{\omega}{c} \frac{d\Delta n}{d\omega} \quad (2.9)$$

Where the first term is independent of frequency and the second term is the dispersion of Δn . In this thesis, we ignore the second term in our simulation.

2.1.3 Polarization-Mode Coupling

In the short length of single mode fiber, where the perturbation is considered uniform, the DGD is deterministic. However, in the long-haul optical fiber communication system, the perturbation on fiber is random. Not only the scale of the birefringence is not uniform, but also the axes of the birefringence are random. These random axes cause polarization mode coupling. The slow and fast polarization modes from one segment are both decomposed to the slow and fast mode in the next segment. People use the concatenation of wave plates with random oriented birefringence axes to model this long fiber[10]. As shown in Figure 2.4.

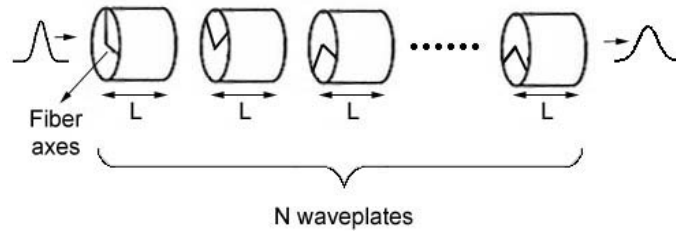


Figure 2.4 Model long fibers by concatenation of wave plates with birefringence axes oriented randomly along the fiber length.

In such a long fiber, DGD does not accumulate linearly with fiber length. The perturbation on fiber can be affected by the environment temperature and the stress added, so the DGD changes randomly with these factors. So statistics is needed to analyze PMD in long fiber. The average DGD of a long fiber is proportional to the square root of the fiber length [12].

2.1.4 Principle State of Polarization

In time domain, when pulse propagates along a long fiber, it has random mode coupling as the birefringence axes changes. The pulse splits at every axis change and thus become complicated. In frequency domain, the output SOP for different frequencies traces an irregular trajectory on Poincarè sphere. In 1986, Poole and Wagner developed the Principle States Model for long fibers [13]. It characterizes PMD both in time domain and frequency domain. In time domain, when people launch the signal of different SOP into the long fiber which has PMD much smaller than the pulse width and has no polarization dependent loss (PDL), there exist two orthogonal launch SOP so that the bit-error rate are minimum. In these two cases, the pulses are undistorted, and are the slowest and the fastest pulses of the entire different SOPs launched. These two SOP is called principle state of polarization (PSP). In frequency domain, input PSP is defined as the input SOP such that the output SOP is independent of frequency over a small span to the first order. The corresponding output SOP is called output PSP. Without PDL in system, the input PSPs and output PSPs are two orthogonal pairs. The output PSP is related to the input PSP by the transmission matrix of the fiber. In Jones calculus, the relation is $E_{out}(\omega) = JE_{in}(\omega)$. In stokes space, the relation is:

$$S_{out}(\omega) = R(\omega)S_{in}(\omega) \quad (2.10)$$

For ideal short fibers, the PSPs are just the birefringence axes. As shown in Figure 2.5(a). The output PSP is the same for all the frequency. For a fixed input SOP, the output SOPs for different frequencies are on a circle that is symmetric about the birefringent axis. Though for long fibers, with a fixed input SOP the output SOP for different frequencies traces an irregular trajectory rather than a circular on Poincarè sphere, but within a small frequency span centered at certain frequency, the SOP is approximately on an arc which is a part of the circle symmetric about the PSP for this certain frequency. As shown in

Figure 2.5(b), for a certain frequency ω_1 and a small span $\Delta\omega$, $SOP(\omega_1 - \frac{\Delta\omega}{2})$ and $SOP(\omega_1 + \frac{\Delta\omega}{2})$ are approximately on the circle symmetric about $PSP(\omega_1)$.

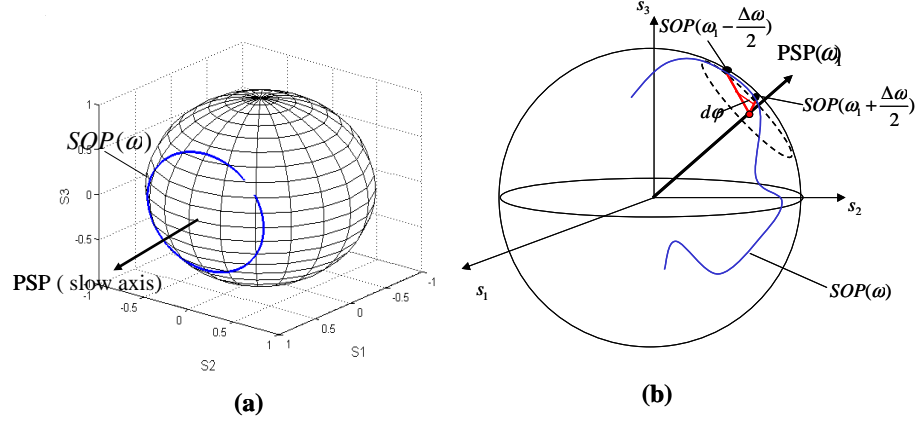


Figure 2.5 (a) output principle state of polarization for an ideal short fiber is the birefringent axis and is the same for all frequency. (b) output PSP of a certain frequency for a long fiber.

Assume that the angle of the arc between $SOP(\omega_1 - \frac{\Delta\omega}{2})$ and $SOP(\omega_1 + \frac{\Delta\omega}{2})$ is $d\varphi$, then the DGD between the two orthogonal PSP of frequency ω_1 is:

$$\tau(\omega) = \left| \frac{d\varphi}{d\omega} \right| \quad (2.11)$$

2.1.5. PMD Vector

In Principal States Model, PSP and DGD are the two key parameters to characterize PMD. We use PMD vector $\vec{\tau}$ to combine these two parameters together [10]. This vector is a vector in Stokes space. Its direction is the slower PSP, and its magnitude is the DGD between the two PSP. That is $\vec{\tau} = \Delta\tau \hat{p}$, where $\Delta\tau$ is DGD and \hat{p} is slower PSP. Correspondingly, the other PSP, the faster PSP, is $-\hat{p}$. If we choose the output PSP as the direction, then we get the output PMD vector, and if we choose input PSP, we get the input PMD vector. They are related by $\vec{\tau}_{out} = R \vec{\tau}_{in}$.

PMD vector also has mathematical definition. Equation 2.10 gives the relation between the input SOP and the output SOP. If the input SOP is fixed for different frequencies, after differentiate both side of this equation, we get [10]:

$$\frac{dS_{out}(\omega)}{d\omega} = \frac{dR(\omega)}{d\omega} S_{in} \quad (2.12)$$

Using Equation 2.10, we can replace the input SOP and get:

$$\frac{dS_{out}(\omega)}{d\omega} = \frac{dR(\omega)}{d\omega} R^{-1}(\omega) S_{out}(\omega) \quad (2.13)$$

In the Equation 2.13, $\frac{dR(\omega)}{d\omega} R^{-1}(\omega)$ can be replaced by $\vec{\tau}(\omega) \times$, and we get [10]:

$$\frac{dS_{out}(\omega)}{d\omega} = \vec{\tau}(\omega) \times S_{out}(\omega) \quad (2.14)$$

Where $\vec{\tau}(\omega)$ is the PMD vector at frequency ω . This equation gives the mathematical definition of PMD vector. The PMD vector describes how the output SOP precesses around the PSP as the frequency varies given the fixed input SOP. The relative direction of $S_{out}(\omega)$ and $\vec{\tau}(\omega)$ determine the local radius of the trajectory, and the magnitude of PMD vector, or the DGD $\Delta\tau$ between two PSPs determine the rate of the precessing of $S_{out}(\omega)$ around $\vec{\tau}(\omega)$. The relation is $\phi = \Delta\tau\Delta\omega$, where ϕ is the rotation angle. If the $S_{out}(\omega)$ is aligned with $\vec{\tau}(\omega)$ or $-\vec{\tau}(\omega)$, then $\frac{dS_{out}(\omega)}{d\omega} = 0$, and the output SOP is frequency independent.

PMD vector is a function of optical angular frequency. If we apply Taylor-series expansion on PMD vector around the carrier frequency ω_0 with span $\Delta\omega$, we get [14]:

$$\vec{\tau}(\omega) = \vec{\tau}(\omega_0) + \frac{d\vec{\tau}(\omega_0)}{d\omega} \Delta\omega + \dots \quad (2.15)$$

We call the first term as the first order PMD, the second term the second order PMD, and etc. If the bandwidth $\Delta\omega$ is small enough so that the second order and higher order PMD can be ignored, then the PMD vector is considered to be constant in this range. We call this bandwidth as PMD vector bandwidth, $\Delta\omega_{psp}$, which is estimated as [10]:

$$\Delta\omega_{psp} = \frac{\pi}{4} \frac{1}{\langle \Delta\tau \rangle} \quad (2.16)$$

Where $\langle \Delta\tau \rangle$ is the mean DGD for the fiber.

PMD vector concatenation rule is a powerful rule to determine the total PMD vector of concatenated elements concatenation when the PMD vector for each element is known. For concatenation of two elements with output PMD vector $\vec{\tau}_1$ and $\vec{\tau}_2$ respectively, the total output PMD vector is [10, 15]:

$$\vec{\tau}(\omega) = \vec{\tau}_2(\omega) + R_2(\omega) \vec{\tau}_1(\omega) \quad (2.16)$$

Where $R_2(\omega)$ is the transmission matrix of the second element. Figure 2.6 gives a simple interpretation. Furthermore, if we apply this equation repeatedly, we can get the total PMD vector for the concatenation of more than two elements.

Similarly, there is also a concatenation rule on the input PMD vector:

$$\vec{\tau}_{in}(\omega) = \vec{\tau}_{1in}(\omega) + R_1(\omega)^{-1} \vec{\tau}_{2in}(\omega)$$

where $\vec{\tau}_{1in}(\omega)$ and $\vec{\tau}_{2in}(\omega)$ is the input PMD vector of the first and the second element respectively, $R_1(\omega)$ is the transmission matrix of the first element.

The relation between the output PMD vector and the input PMD vector is:

$$\vec{\tau}(\omega) = R_2(\omega) R_1(\omega) \vec{\tau}_{in}(\omega)$$

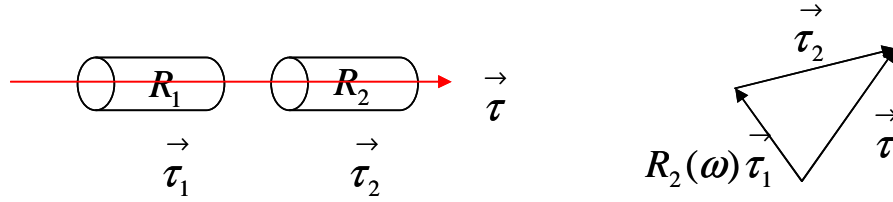


Figure 2.6 Concatenation rule of PMD vectors

2.2. PMD in polarization maintaining fiber (PMF)

For regular single mode fiber, the differential refractive index Δn is $\sim 10^{-7}$, and even if there is no mode coupling to reduce the mean DGD, the 3000-meter long fiber only has 1ps mean DGD. However, for polarization maintaining fiber (PMF), higher differential refractive index is intentionally introduced in the manufacture process. The differential refractive index of PMF Δn is $\sim 10^{-4}$. So only 3 meter such PMF can have 1ps mean DGD. In our PMD vector measurement experiment, we choose PMF as device under test (DUT), because in this case we don't need PMF of very long length, and thus we can measure the fiber length and splice the fiber needed more easily and accurately.

In our experiment, we test three kind of PMF: one-piece PMF, concatenation of two-piece PMF, and concatenation of three-piece PMF, and measure their output PMD vectors.

2.2.1. One-piece PMF

One-piece PMF is modeled by a wave plate. For a fixed input SOP for all the frequencies, the output SOP traces a circle on the Poincarè sphere as the frequency varies. This circle is symmetric about the slow axis of the PMF. If the length of this one-piece PMF is l and the differential refractive index is Δn , then the frequency span $\Delta\omega$ within which the output SOP traces exactly one circle satisfies:

$$\frac{\Delta\omega\Delta nl}{c} = 2\pi \quad (2.17)$$

From this equation we know that this frequency span is:

$$\Delta\omega = \frac{2\pi c}{l\Delta n} \quad (2.18)$$

The PMD vector of this one-piece PMF is the same for all the frequencies: $\vec{\tau} = \Delta\vec{\varphi}$. The direction of the PMD vector or the PSP \hat{p} is the slow axis, and for all the frequencies it is one point on the Poincarè sphere. The DGD $\Delta\tau$ satisfies:

$$\Delta\tau = \frac{\partial\varphi_f(\omega) - \partial\varphi_s(\omega)}{\partial\omega} = \frac{(-\omega n_f l) - (-\omega n_s l)}{c} = \frac{l\Delta n}{c} \quad (2.19)$$

2.2.2. Two-piece PMF

The PMD vector of the concatenation of two pieces of PMF can be obtained from the concatenation rule. As shown in Figure 2.7 (a), we splice two pieces of PMF together. The length of them is l_1 and l_2 respectively, and the angle between two slow axes is θ . From the concatenation rule: $\vec{\tau}(\omega) = \vec{\tau}_2(\omega) + R_2(\omega)\vec{\tau}_1(\omega)$, firstly we rotate the PMD vector of the first PMF by the rotation matrix of the second PMF, and then add it to the PMD vector of the second PMF so that we get the total PMD vector. By applying the rotation matrix of the second PMF, the first PMD vector is rotated around the second PMD vector. As shown in Figure 2.7 (b), the rotation matrix R_2 is different as the frequency varies, as a result $R_2\vec{\tau}_1$ traces on the circle C_1 for different frequencies. After adding $R_2\vec{\tau}_1$ to $\vec{\tau}_2$, we get the total PMD vector, which traces on the circle C_2 .

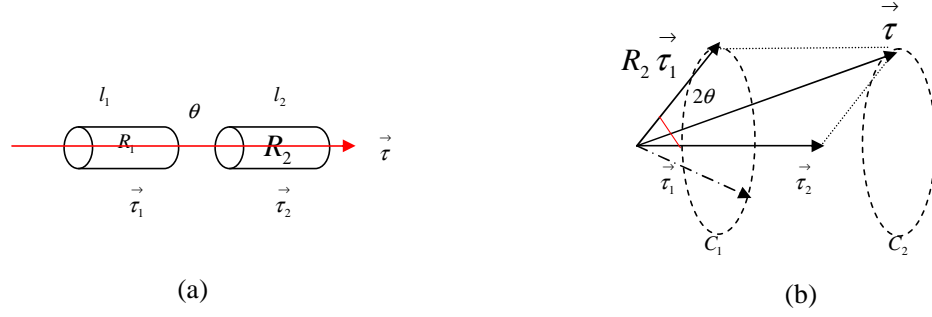


Figure 2.7 (a) Concatenation of two pieces of PMF with angle θ between two slow axes. (b) Concatenation of two PMD vectors.

The PMD vector of two-piece PMF has the following properties:

1. PSP for all frequency in a certain span on Poincaré sphere is on a circle. This is similar to how the output SOP traces around the slow axis in one-piece PMF. The span $\Delta\omega$ with which the PSP traces exactly one circle also satisfies Equation (2.16), and it is: $\Delta\omega = \frac{2\pi c}{\Delta n l_2}$.
2. The radius of this PSP circle is determined by θ and $\frac{|\vec{\tau}_1|}{|\vec{\tau}_2|}$. As shown in Figure 2.7 (b). For example, if $2\theta = 90^\circ$, then the larger is $\frac{|\vec{\tau}_1|}{|\vec{\tau}_2|}$, the larger is the radius.
3. DGD is the same for all the frequency, because the angle between $R_2 \vec{\tau}_1$ and $\vec{\tau}_2$ remains the same for all the frequencies.

Except for the above properties, there is another one interesting phenomena caused by the rotation matrix R_2 of the second PMF, and it should be considered in our PMD vector measurement experiment. We know that, for one-piece PMF, if the input SOP of a certain frequency is not aligned with the birefringent axes, the SOP evolves repeatedly along the fiber length. The beat length, with which the SOP returns to itself, is about 3mm with $\Delta n \sim 4 \times 10^{-4}$. This means that the rotation matrix of one-piece PMF changes repeatedly with length of the PMF, and return to itself with the increase of one beat length. Therefore, if the length difference is a fraction of beat length, even as small as 1mm, the rotation matrix R_2 changes in an obvious way. As shown in Figure 2.8, if we assume that the SOP along the length of one-piece of PMF evolves on a circle on Poincaré sphere, with one more half of the beat length, the SOP can be rotated from point

A to point B by the rotation matrix. Unfortunately, in our lab, the measurement error is $\sim 1mm$ when measuring the length of one-piece PMF. As a result, we don't know the exact location of $R_2\vec{\tau}_1$ for a certain frequency on the circle C_1 (Figure 2.7 (b)), and thus neither exact location of $\vec{\tau}$ on circle C_2 . However, we are still confident that $R_2\vec{\tau}_1$ for all frequency is on circle C_1 , and $\vec{\tau}$ is on circle C_2 .

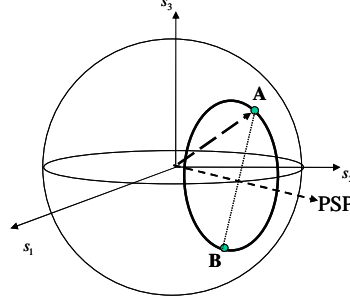


Figure 2.8 the output SOP for a certain frequency changes from A to B if the length of one-piece PMF increases by half of its beat length.

2.2.3. Three-piece PMF

The PMD vector of the concatenation of three-piece PMF is much more complicated than two-piece PMF. Figure 2.9 (a) shows the concatenation of three-piece PMF, and Figure 2.9 (b) shows the concatenation rule of the total PMD vector. We can see that the total PMD vector $\vec{\tau}$ is determined by the PMD vector of each PMF, the rotation matrix of the second, and the third PMF. From the concatenation rule for two-piece PMF, we know that the total PMD vector $\vec{\tau}'(\omega)$ of the first two-piece PMF is on the circle C_2 with different location for different frequency. Then this PMD vector is rotated by the rotation matrix of the third PMF and then added to the PMD vector of the third piece PMF to get the total PMD vector. For example, (as shown in Figure 2.9 (c)), for a certain frequency ω_1 , the total PMD vector $\vec{\tau}'(\omega_1)$ of the first two-piece PMF, whose end is on the circle C_2 , is rotated by the rotation matrix $R_3(\omega_1)$ of the third PMF and added to the PMD vector $\vec{\tau}_3$ to get the total PMD vector $\vec{\tau}(\omega_1)$ of three-piece PMF. However, the total PMD vector $\vec{\tau}(\omega_2)$ varies much for frequency ω_2 , as shown in Figure 2.9 (d).

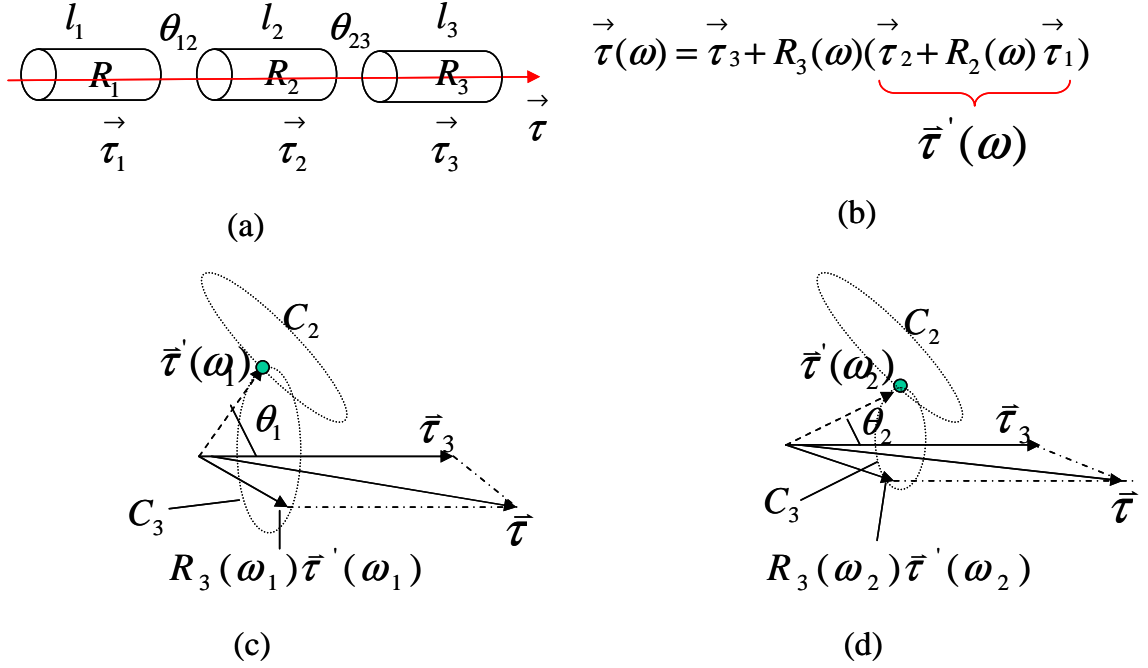


Figure 2.9 (a) Concatenation of three pieces of PMF. (b) The concatenation rule of the total PMD vector for three-piece PMF. (c) The total PMD vector of three-piece PMF for a certain frequency. (d) The total PMD vector of three PMF for another frequency.

Though the total PMD vector $\vec{\tau}'(\omega_2)$ of the first two PMF has the same length with $\vec{\tau}'(\omega_1)$, the end of this vector is at different location on the circle C_2 due to the frequency dependence of rotation matrix $R_2(\omega)$. The rotation matrix of the third PMF $R_3(\omega_2)$ for frequency ω_2 also rotates $\vec{\tau}'(\omega_2)$ in a different way. As a result, the total PMD vector $\vec{\tau}$ varies with frequency in a complicated way, especially the direction of the vector.

However, the length of the total PMD is a periodic function:

$$|\vec{\tau}(\omega + \Delta\omega)| = |\vec{\tau}(\omega)| \quad (2.20)$$

where $\Delta\omega = \frac{2\pi c}{\Delta n l_2}$. This can be easily understood by Figure 2.10:

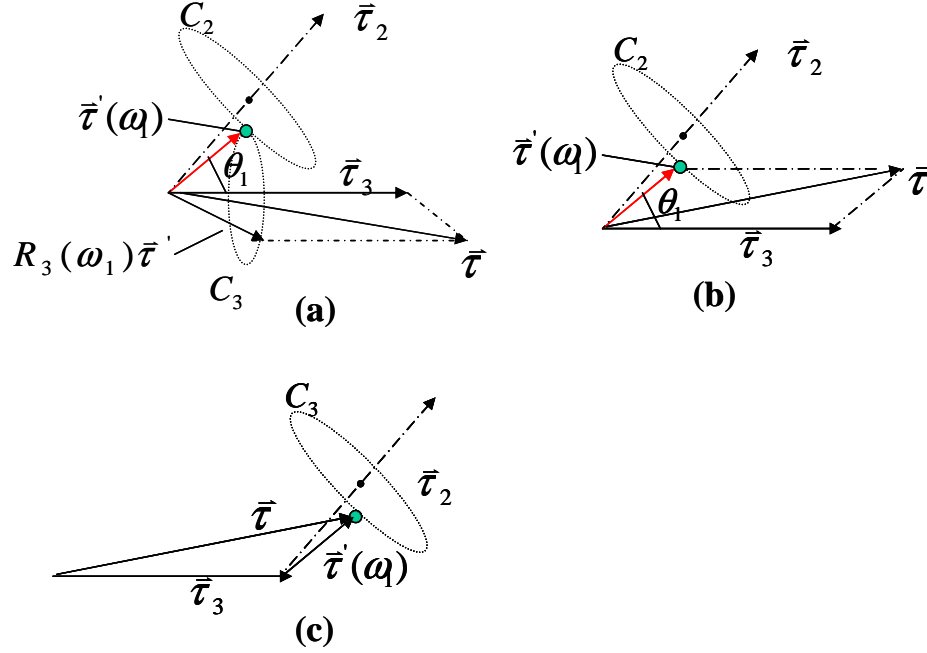


Figure 2.10 (a) the total PMD vector of 3-piece PMF for a certain frequency. (b) Compare to (a), only without the rotation operation, the total DGD remains the same with (a). (c) Using the operations in (b), the end of total PMD vector is on the circle.

Figure 2.10 (a) shows that the end of total PMD vector $\vec{\tau}'$ of the first two PMF lies on the circle C_2 , and for a certain frequency ω_1 , the angle between $\vec{\tau}'(\omega_1)$ and $\vec{\tau}_3$ (the PMD vector of the third PMD) is θ_1 . Apply the rotation matrix $R_3(\omega_1)$ on $\vec{\tau}'(\omega_1)$, the angle between $R_3(\omega_1)\vec{\tau}'(\omega_1)$ and $\vec{\tau}_3$ is still θ_1 . Since the rotation doesn't change the length of $\vec{\tau}'$ either, we can get this equation:

$$|\vec{\tau}| = |R_3(\omega)\vec{\tau}'(\omega) + \vec{\tau}_3(\omega)| = |\vec{\tau}'(\omega) + \vec{\tau}_3(\omega)| \quad (2.21)$$

This equation means that, if we omit the rotation operation R_3 , as shown in Figure 2.10 (b), we still get the same DGD, though the direction of $\vec{\tau}$ have changed. Figure 2.10 (c) shows that by the operation in Figure 2.10 (b), the end of $\vec{\tau}$ lies on the different location of circle C_3 for different frequency. The circle C_3 is the shift of C_2 by $\vec{\tau}_3$ in 3-D space (stokes space). So just like the end of $\vec{\tau}'$ varies with frequency evenly on circle C_2 , the end of $\vec{\tau}$ varies with frequency evenly on circle C_3 . So $|\vec{\tau}|$ changes with frequency repeatedly and the period is the same with the period of $\vec{\tau}'$: $\Delta\omega_p = \frac{2\pi c}{\Delta n l_2}$.

The simulation result also confirms the periodic property of $|\vec{\tau}(\omega)|$, the total DGD, as shown in Figure 2.11. In the simulation, we apply the PMD vector concatenation rule in the computer program to get the DGD of the concatenation of three-piece PMF.

The length of each PMF is 50cm, 80cm and 60cm, the slow axis angle offset between the first and the second PMF is 45° , and between the second and the third -50° . The differential refractive index of the PMF is $\Delta n = 4.1434 \times 10^{-4}$, and the beat length is 3.7mm. The wavelength span is from 1542.86nm to 1556.86nm. In this optical frequency span, the second PMF can rotate a fixed input SOP to about one and one half circles on the Poincarè sphere. The total DGD is the solid curve in this figure. It is a periodic function (not sinusoidal, because $a \neq b$, as shown in the figure.) with the period

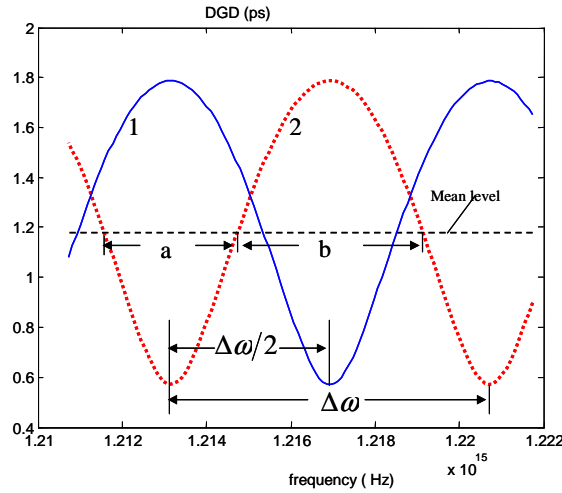
$$\Delta\omega_p = \frac{2\pi c}{\Delta n l_2} \approx 7.58 \times 10^{12} \text{ Hz}.$$


Figure 2.11 The simulation result for the total DGD of three-piece PMF. In case 1 (solid curve), the length of each piece of PMF is 50cm, 80cm and 60cm, the slow axis angle offset between the first and the second PMF is 45° , and between the second and the third -50° . The beat length of the PMF is 3.7mm. We increase the length of the second PMF by half of the beat length to get the case 2 (dashed curve).

If we increase the length of the second PMF by one-half of the beat length, 1.85mm, we get the dashed curve, which is shifted by $\Delta\omega/2$ from the solid curve. This is because that the $R_2(\omega)$ gives one more half circle's rotation, and let the end of the vector $\vec{\tau}'$ rotate one more half circle on the circle C_2 (as shown in Figure 2.10 (a)) for each frequency. This makes the curve of DGD vs. frequency shifts one-half period.

2.3. Multi-input SOP Method to Measure PMD vector

For the fiber under test (FUT), we give a fixed input SOP for all the frequencies in a span, and measure the output SOP for each frequency. We repeat this process several

times by giving different fixed input SOP and measuring the output SOP sets. Then we can calculate the PMD vector for each frequency from the output SOP sets [3, 4]. The principle is shown in Figure 2.12.

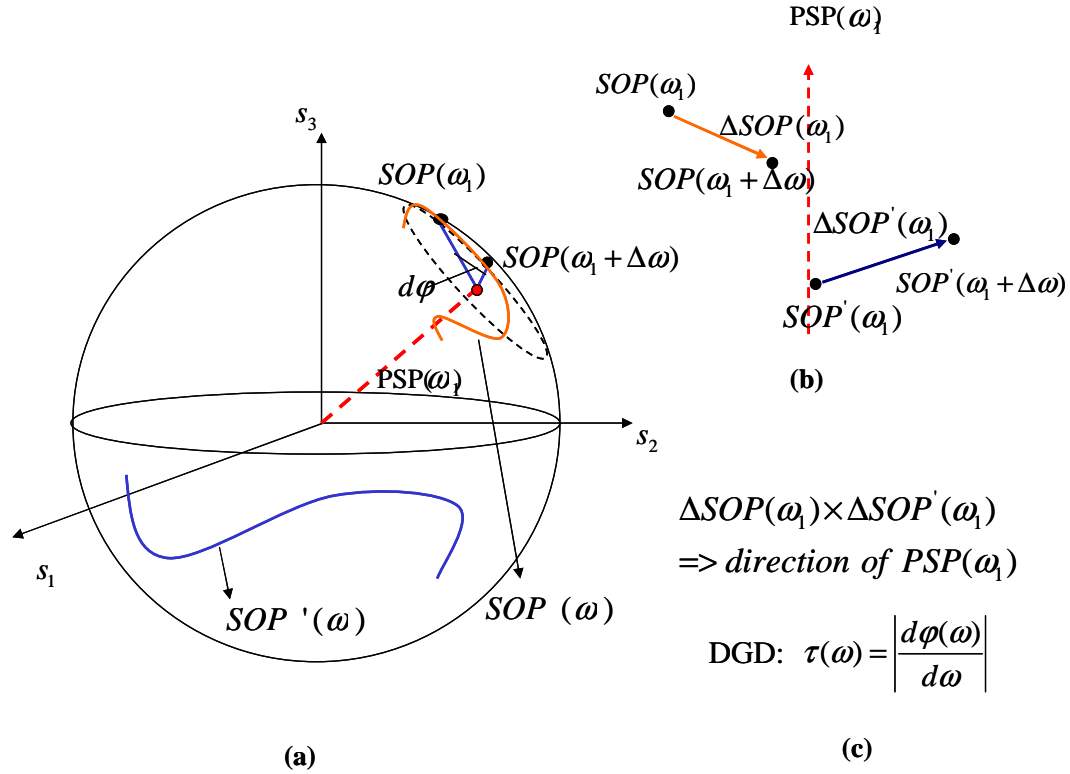


Figure 2.12 (a) Two set of output $SOP(\omega)$ on the Poincaré sphere for two different fixed input SOP. (b) If the frequency increases by a small span, the change of the output SOP at certain frequency is orthogonal to the output PMP of this frequency. This also works for other output SOP sets. (c) Extract DGD and output PMP from the output $SOP(\omega)$ sets.

As shown in Figure 2.12 (a), in the case that the input SOP is fixed for all the frequencies, the output SOP for all the frequencies traces a curve on the Poincaré sphere. Within a small frequency span $\Delta\omega$, $SOP(\omega)$ can be approximated by an arc on the Poincaré sphere. The axis of the arc is along the direction of the output PMD vector $\vec{\tau}(\omega)$. The angle of the arc is proportional to the DGD $\tau(\omega)$. These rules hold for other output SOP sets no matter what the fixed input SOP is. As a result, the differential output SOP vectors such as $(SOP(\omega_1 + \Delta\omega) - SOP(\omega_1))$ and $(SOP'(\omega_1 + \Delta\omega) - SOP'(\omega_1))$ are all orthogonal to the output PMD vector $\vec{\tau}(\omega_1)$, as shown in Figure 2.12 (b). So the output

PSP at frequency ω_1 can be obtained by the direction of the cross product of the differential SOP vectors $(SOP(\omega_1 + \Delta\omega) - SOP(\omega_1))$ and $(SOP(\omega_1 + \Delta\omega) - SOP(\omega_1))$. Moreover, the DGD is obtained by the ratio of the arc angle to the differential span $\Delta\omega$ [3, 4], as shown in Figure 2.12 (c).

We can give more input fixed SOP, and measure the output SOP sets. Then we can calculate PSP from each pair of differential output SOP vectors and improve the result by averaging. In addition, the DGD is obtained from each output SOP sets and averaged to get result that is more accurate.

Since PMD vector is frequency dependent, we should choose small enough step size $\Delta\omega$ to calculate PMD. We are safe to choose the PSP bandwidth given by $\Delta\omega = \frac{\pi}{4\langle\tau\rangle}$ [10], where $\langle\tau\rangle$ is the mean DGD. Within this bandwidth, the PMD vector is constant reasonably.

We disperse the light frequencies to an array in free space by grating and lens set, as a result the output SOP can be measured for all the frequency simultaneously. So we can get the PMD vector for all the frequency efficiently.

3. EXPERIMENTAL SETUP

We use the multi-input SOP method to measure PMD vector of the device under test (DUT). As shown in Figure 3.1, our experimental setup includes several parts (in the order of the light propagation): ASE (Amplified Spontaneous Emission) source, single mode fiber, collimator A, multi-SOP producer, collimator B, PMD emulator, collimator C, SOP components selector, telescope, grating, lens, one-dimensional CCD(Charge Coupled Device) camera.

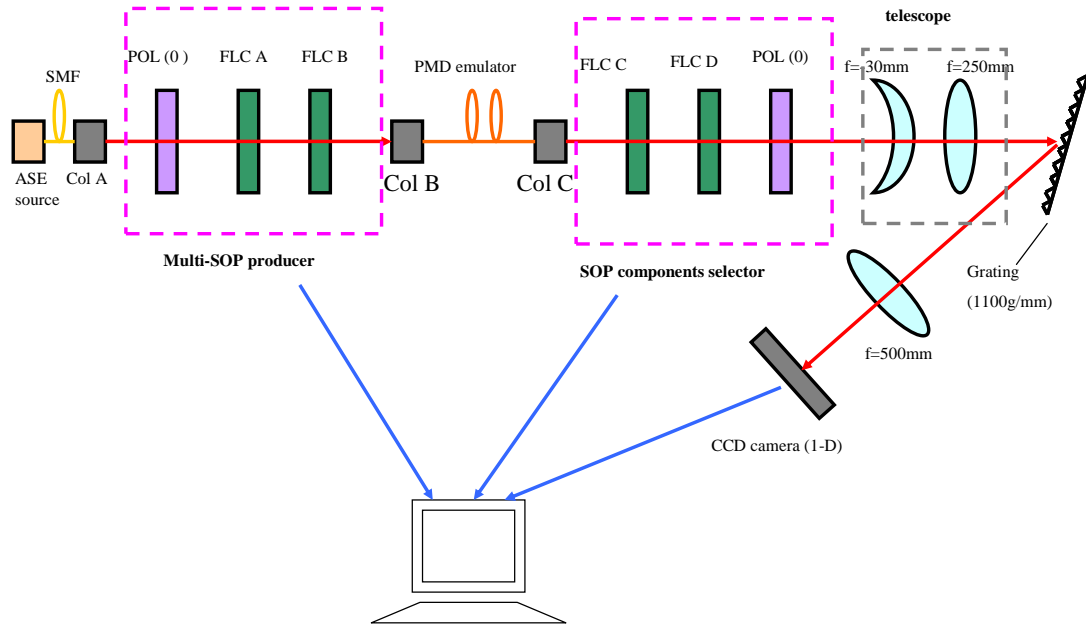


Figure 3.1 The PMD measurement setup

We choose ASE source because it can provide high power and broad bandwidth. Single mode fiber of suitable length is used to connect the laser and the collimator A. Collimators can be used to couple a free space laser beam into an optical fiber as well as to collimate a laser beam propagating out of the end of an optical fiber. In our setup, collimators play an important role in transforming the light propagating between the free space and optical fibers. Collimator transforms the laser beam to free space so that the

multi-SOP producer can be applied. Collimator B is exactly the same with collimator A so as to reduce the coupling loss as much as possible. We made a simple PMD emulator by splicing PMF, and then connect it with collimator B and C by single mode fiber. Collimator C also provides a free space laser beam. The telescope, grating and lens are to disperse different light frequency to an array in free space. The one dimensional CCD camera is used as detector. We use computer to control the multi-SOP producer, SOP component selector and the camera by DAQ board.

We show more details about the main components of the setup in the following content.

3.1 Multi-SOP producer and SOP component selector

The multi-SOP producer and SOP component selector are very similar. They both contain two quarter wave plate (QWP) retarders made from ferroelectric liquid crystal (FLC) [16, 2] and one linear Polarizer.

When we add voltage to the FLC cells, the molecules changes their orientation, and so is the polarization vector. The birefringent axis can be switched between two stable states, which are designed to be 45° apart. As shown in Figure 3.2, the fast axis switches when we apply two different voltage $+5v$ and $-5v$, and the switching time can be less than $100\mu s$. We use a voltage driver to provide the $\pm 5v$ voltage. Computer via DAQ board controls the driver.

In the multi-SOP producer, first we use one polarizer (with extinction ratio 1000:1) to produce horizontal linear polarization. After the horizontal polarizer, we use two FLC retarders to change the state of the polarization. Since the fast axes of FLC cells can be switched, we can produce four different SOP. The truth table is as shown in Figure 3.3.

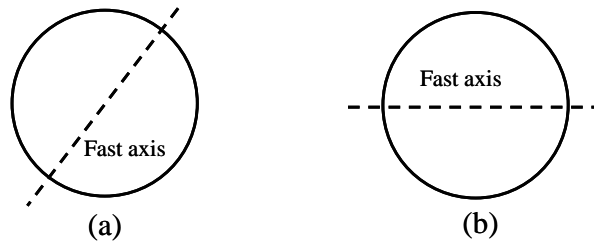


Figure 3.2 The fast axis of the FLC retarder: (a) $+5v$ voltage applied. (b) $-5v$ voltage applied.

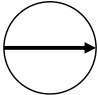
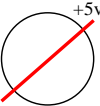
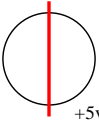
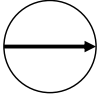
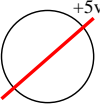

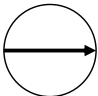
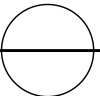
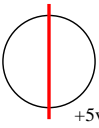
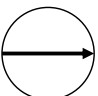
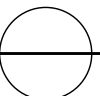
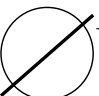
	Polarizer (0°)	Fast axis of FLC A	Fast axis of FLC B	Output SOP
(a)				135°
(b)				90°
(c)				0°
(d)				RHC

Figure 3.3 The truth table of the multi-SOP producer.

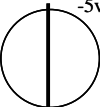
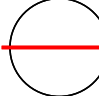
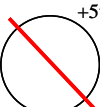
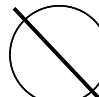
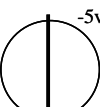

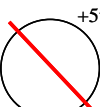
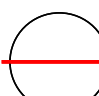
	Input SOP	Fast axis of FLC A	Fast axis of FLC B	Output SOP
(a)	0°			0°
(b)	90°			
(c)	45°			
(d)	RHC			

Figure 3.4 The truth table for the SOP component selector.

In our SOP component selector, we put a horizontal polarizer after two FLC cells. The input SOPs 0° , 45° , 90° and RHC are transformed into horizontal linear SOP

respectively by switching the fast axes of FLC cells [2]. The truth table is as shown in Figure 3.4. As a result, the intensity of these components ($I_0, I_{45}, I_{90}, I_{RHC}$) can be selected by the horizontal polarizer. These intensity components are just what we need to determine the Stokes vector of the SOP under test.

3.2 Spatial Dispersion

In order to measure the PMD of all frequencies simultaneously, we use a grating to disperse the different frequency component of the light beam to an array. To design this dispersion device, we should consider two aspects:

(i) The beam size should be comparable to the size of the camera pixel. We use one-dimension CCD camera as detector. This camera has 128 pixels that are aligned in an array, and the size of width of each pixel is $50\mu\text{m}$. So the beam on the CCD array should have the diameter comparable to $50\mu\text{m}$.

(ii) The light should be dispersed enough so that the measurement has high enough frequency resolution. The frequency resolution at the CCD array is determined by the both the grating and the focus length of the lens after the grating.

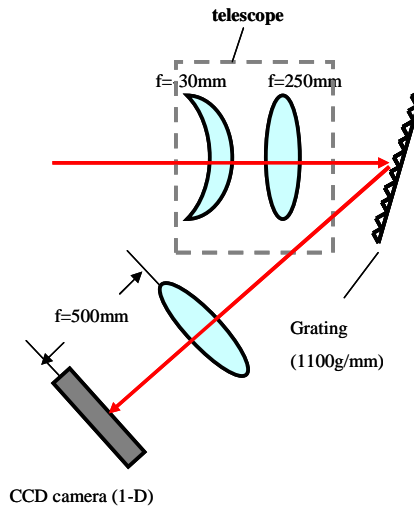


Figure 3.5 The spatial dispersion setup.

Our design is shown in Figure 3.5. The diameter of the light beam before the telescope is 2.7mm . The telescope contains a concave lens with focus length of -30mm and a convex lens with focus length 250mm . We put the focuses of these two lenses together so that they form a telescope that can enlarge the beam size by $25/3$ times. As a result, the beam's diameter becomes 22.5mm after the telescope. Then a grating

(25mm×25mm), as shown in Figure 3.6 diffracts the light beam. We use the -1 order diffraction, which means that the output light and the input light are on the same side of the normal. So the grating equation is:

$$\sin \theta_i + \sin \theta_d = \frac{\lambda}{d} \quad (3.1)$$

Where θ_i and θ_d are the input angle and the diffraction angle respectively, and d is the grating constant, which is determined by the groove frequency of the grating. Our grating has 1100 grooves per millimeter, so $d = (1/1100)\text{mm}$. This equation shows that the diffraction angle is different for different wavelength, and this is how the grating disperses the input beam to a spatial array.

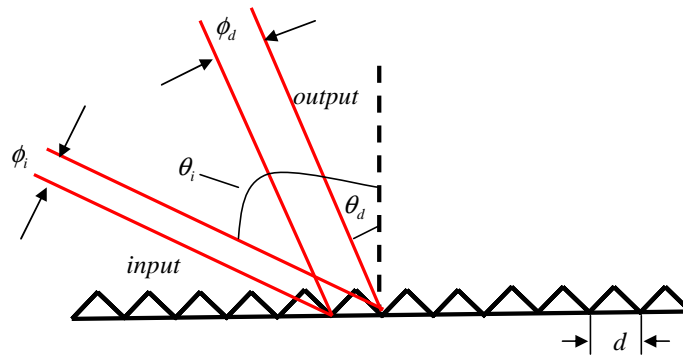


Figure 3.6 Light diffracted by a grating.

The grating also changes the beam size, as shown in Figure 3.6. Assume that the diameter of the input beam and the output beam is ϕ_i and ϕ_d respectively, they satisfy the equation:

$$\frac{\phi_i}{\cos \theta_i} = \frac{\phi_d}{\cos \theta_d} \quad (3.2)$$

We choose $\theta_i > \theta_d$ to enlarge the beam size.

After the grating, we use a concave lens with focus length $f = 500\text{mm}$ to focus the beams. The beam waists are approximately on the focus plane of the lens, where we locate the CCD array of the camera. By the lens, we can reduce the beam size. The relation between the beam size before and after the lens is:

$$\phi_{out} = \frac{4\lambda f}{\phi_{in}} \quad (3.3)$$

From this equation, we can see that the larger is the input beam size; the smaller is the output beam size. This is why previously we not only use the telescope but also choose large input angle of the grating to enlarge the beam size.

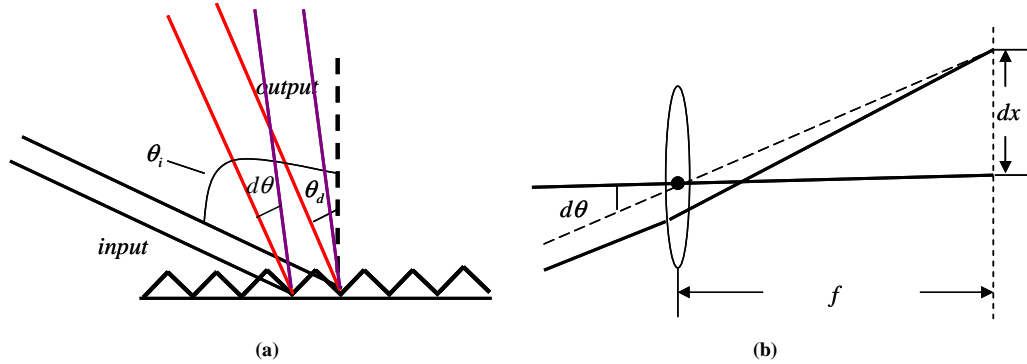


Figure 3.7 (a) The light is diffracted by the grating. (b) The concave lens focuses the beams on its focus plane.

Both the grating and the lens determine the frequency span on the CCD array after the grating. By differentiating both sides of the grating Equation (3.1), we get:

$$\frac{\partial \theta_d}{\partial \lambda} = \frac{1}{(\cos \theta_d) d} \quad (3.4)$$

So the larger is θ_d , or the smaller is θ_i , the larger is the differential diffraction angle. However, we also need a large θ_i to enlarge the beam size, so there is a tradeoff about θ_i .

After the grating, the concave lens transforms the differential diffraction angle into the differential length on the focus plane, or the CCD array, as shown in Figure 3.7 (a). The transformation is :

$$\partial x = f \partial \theta \quad (3.5)$$

Finally, our measurement setup has the following parameters:

- (i) The beam is about 200 μm , and covers two CCD pixels.

In our design, the beam size is supposed to be 100 μm . However, in the experiment, we try our best and get 200 μm beam size. Since the setup works, we just leave the improvement to the future work.. We show how we calculate the design beam size in the following: (1) 2.7 mm (the width at $1/e^2$ of the maximum intensity) beam size after collimator C. (2) 22.5mm beam size after the telescope that enlarges the beam size by 25/3 times. (3) 32.0 mm beam size after the grating that enlarges the beam size by

$\frac{\cos \theta_d}{\cos \theta_i} = \frac{\cos 53.0^\circ}{\cos 65.0^\circ} = 1.42$ times. (4) 97 μm beam size after the focus lens and on the camera pixels (obtained from Equation (3.3)).

The camera has CCD 256 pixels, and each pixel is 50 μm in width. The control on 128 odd numbers of pixels and the control on 128 even numbers of pixels are independent. Moreover, the sensing value has obvious jump between even and odd pixels even the input optical field intensity is the same for all pixels. Currently we just open half of the pixels by choosing all the odd numbers, and will choose all 256 pixels in the future. So 200 μm beam size covers 2 of the 128 pixels we choose.

(ii) On the CCD array: 1542.9~1556.9nm over 128 pixels, or 13.6G Hz / pixel

The diffractive angle of the grating is 53.0°. The focus length of the lens before the camera is 500mm. The grating constant is $d = 1/1100\text{mm}$. The 128 pixels of the camera cover 12.8 mm in width. From Equation (3.4) and (3.5), we get the wavelength span on these 128 camera pixels is $\partial\lambda = 14\text{nm}$. We tune the camera, and have the span be 1542.9~1556.9nm.

4. EXPERIMENT RESULTS AND DATA PROCESSING

In our PMD vector measurement method, we give a fixed input SOP for all the frequency in a span and measure the output SOP set. Then by giving multi-SOP input, we measure several output SOP sets. After the measurement, we calculate the PMD vector for each frequency from the differential output SOP vector. Briefly speaking, our job includes two parts:

- (i) Output SOP measurement.
- (ii) Data processing.

Though we try to reduce the measurement error caused by the FLCs and the camera noise, the error can still ruin the calculation of PMD vector, because the differential SOP vector is not large enough compared to error. Therefore, we use data fitting technique to smooth the measurement data. We also perform simulation to see the effect of noise and how the data fitting works. However, except for the measurement error, there is some output SOP itself not suitable to calculate PMD vector, and so we need to make a rule to get rid of the ‘bad’ SOP.

After the measurement and data processing, we get the PMD vectors and compare them with the estimation from the PMD vector concatenation rules. They show good agreement to each other, making sure that our measurement method works well.

4.1 SOP Measurement

Our SOP component selector can select the intensity of four components of SOP: $I_{0^\circ}, I_{90^\circ}, I_{45^\circ}, I_{RHC}$ by switching the birefringent axis of two FLC cells. We use grating to diffract the different frequency components of the light beam to a spatial array, and adjust the beam size to CCD sensing pixels by lenses. We use 128 pixels of the camera, and thus we have 128 evenly distributed samples of the frequency span that covers the CCD array. We check the beam size on the CCD array by giving a single wavelength input. The intensity of one of the four SOP components measured by the camera is as shown in Figure 4.1:

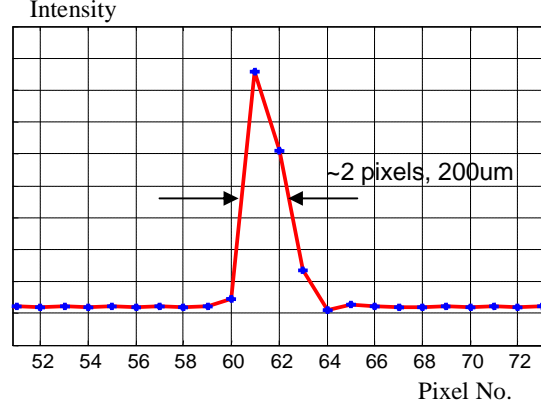


Figure 4.1 Use single frequency input to test the beam size on the CCD array. The FWHM of the intensity is about 2 pixels, or 200um.

From this picture, we can see that the full width of half maximum of the intensity covers about 2 pixels, or 200um. So the intensity provide by a certain pixel is not a pure intensity from a certain frequency ω_0 which centers on this pixel, it also contains the contribution of other frequencies near this certain frequency. If we assume that the frequency span covering one pixel is $\Delta\omega$, the intensity of the frequencies from $\omega_0 - 2\Delta\omega$ to $\omega_0 + 2\Delta\omega$ contributes. As a result, if the SOP changes much from $\omega_0 - 2\Delta\omega$ to $\omega_0 + 2\Delta\omega$, the SOP measurement can have large error. However, even if the SOP changes in this span are small, they still cause measurement error.

Another error is from the background noise in the camera. This noise is random and cannot be subtracted. As to reduce the effect of the noise, we increase the signal to noise ratio by tuning the intensity as high as possible so far as the camera is not saturated.

The two FLC cells in the SOP component selector can also cause error in the following two ways:

- (i) In our setup design, for each FLC cell, the switched angle of the slow axis is 45° . However, actually one is 44° , and the other one is 44.3° .
- (ii) The FLC cells are supposed to be quarter wave plate (QWP). But except for the center wavelength $1550nm$, they are not exact QWP for other wavelength.

We use a calibration matrix M_c to correct the measurement error from FLC cells [2]. Let the relation between the measurement $I = (I_{0^\circ}, I_{90^\circ}, I_{45^\circ}, I_{RHC})^T$ (the intensity of four components) and the real SOP $S = (S_0, S_1, S_2, S_3)^T$ (four Stokes parameters) be: $SM_c = I$, and obviously we can get $S = IM_c^{-1}$. The calibration matrix M_c is a

4×4 matrix, so it has 16 parameters. We give six known input SOPs to the FLC cells: $0^\circ, 90^\circ, 45^\circ, 135^\circ, RHC, LHC$, and measure $I = (I_{0^\circ}, I_{90^\circ}, I_{45^\circ}, I_{RHC})^T$. By the relation $SM_c = I$, we can get 24 equations about 16 unknown parameters. By solving these equations in the least square sense, we can get the calibration matrix. Figure 4.2 shows the measurement result of 135° SOP before and after the calibration:

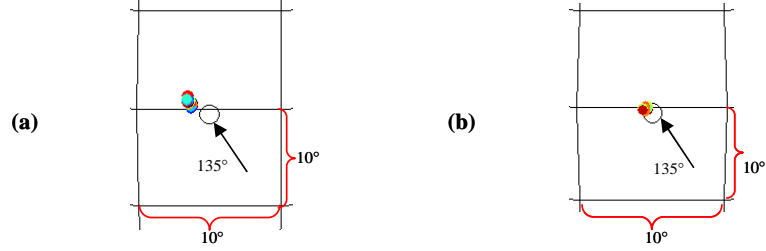


Figure 4.2 The measurement of 135° SOP for all frequencies (on Poincaré sphere): (a) before calibration. (b) After calibration.

Actually the calibration matrix itself has error. Because to get the calibration matrix, we have to produce 6 known input SOPs by the combination of polarizer and quarter wave plate and can't avoid error. For example, the error can be caused not only by the rough scale of the rotation stage of the polarizer and the QWP, but also by the frequency dependence of the QWP. However, Figure 4.2 shows that this calibration increases the accuracy of the SOP measurement significantly.

After all the improvement of the SOP measurement, our result is shown in Figure 4.3, Figure 4.4 and Figure 4.5.

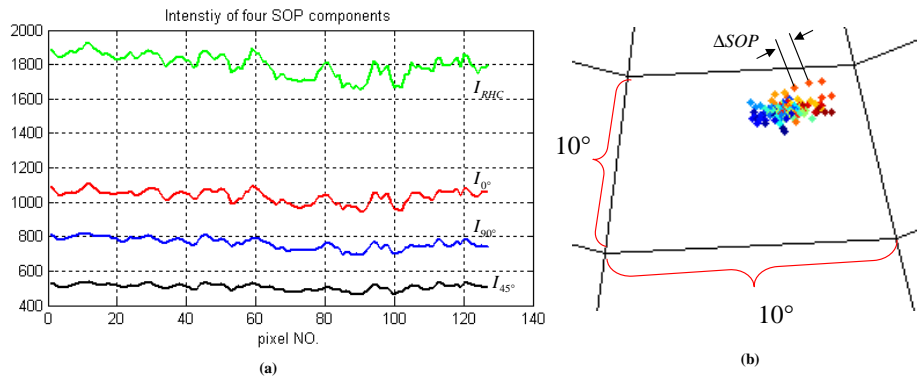


Figure 4.3 The output SOP measurement result for a short SMF without PMD. (a) The intensity of four SOP components vs. CCD pixel number. (b) The output SOP on the Poincaré sphere.

In Figure 4.3, we use a short section of single mode fiber as the device under test (DUT). This means that there is no PMD in the DUT, though the single mode fiber can change the input SOP, the output SOP remains the same for all the frequency. So the output SOP is supposed to converge to one point on the Poincarè sphere. Figure 4.3 (a) shows the intensity of four SOP components measured by the camera. Each curve has fluctuations. This can be explained in two ways. One reason is that after the ASE source go through the polarizer in the multi-sop producer the spectrum is not constant. The other reason is that the camera CCD pixels have different ability to transform light intensity to electrical voltage. Therefore, the measurement error is not shown in these intensity fluctuations, but shown in the SOP on the Poincarè sphere. Figure 4.3 (b) shows the SOP on the Poincarè sphere. Due to the measurement error, the SOPs do not converge to one point, and thus introduce extra differential SOP vector ΔSOP . We call this as error of ΔSOP .

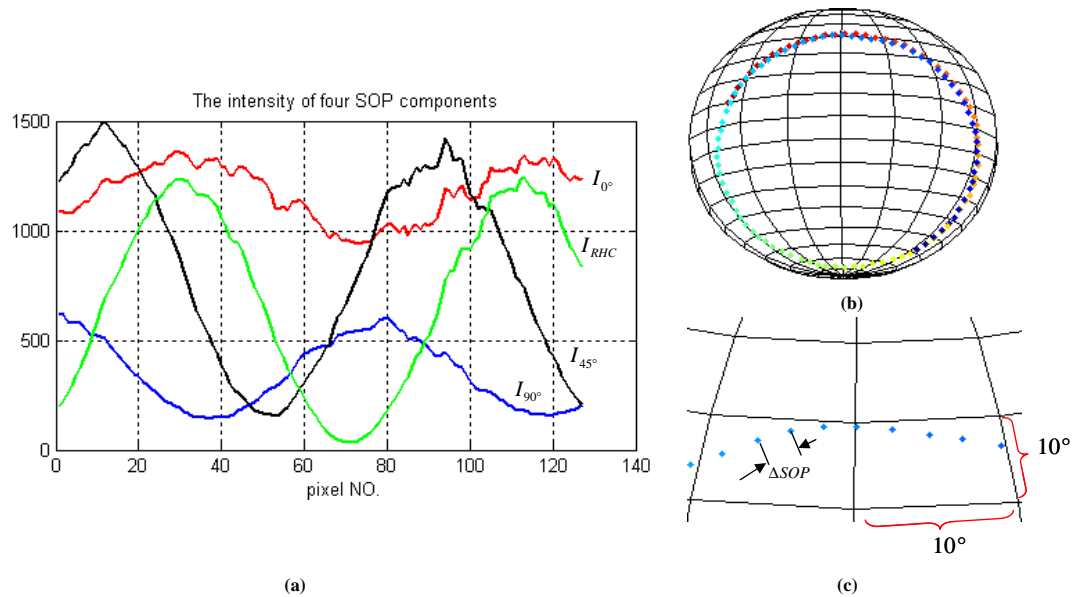


Figure 4.4 The output SOP measurement of one-piece PMF with 96.9cm length. (a) The intensity of four SOP components vs. CCD pixel number. (b) the output SOP traces a circle on the Poincarè sphere. (c) Zoom in the output SOP on the Poincarè sphere to see the differential SOP vector ΔSOP .

Figure 4.4 shows the output SOP measurement for one-piece PMF with 96.9 cm length. The wavelength span on the CCD array is $1543.4 \sim 1553.0nm$. The differential refractive index Δn of the PMF is 4.15×10^{-4} . In Figure 4.4 (a), except for the fluctuations similar to Figure 4.3 (a), each curve is approximate to a sinusoidal function.

This can be explained by Figure 4.4(b), where the output SOP on the Poincaré sphere traces on a circle, and the trajectory is about one and one half circles, so the intensity of an arbitrary component is a sinusoidal function with one and one half periods. Zoom in the Figure 4.4 (b), we get Figure 4.4 (c). It shows that the differential SOP vector ΔSOP is very small and can be affected by the error of ΔSOP shown in Figure 4.3 (b).

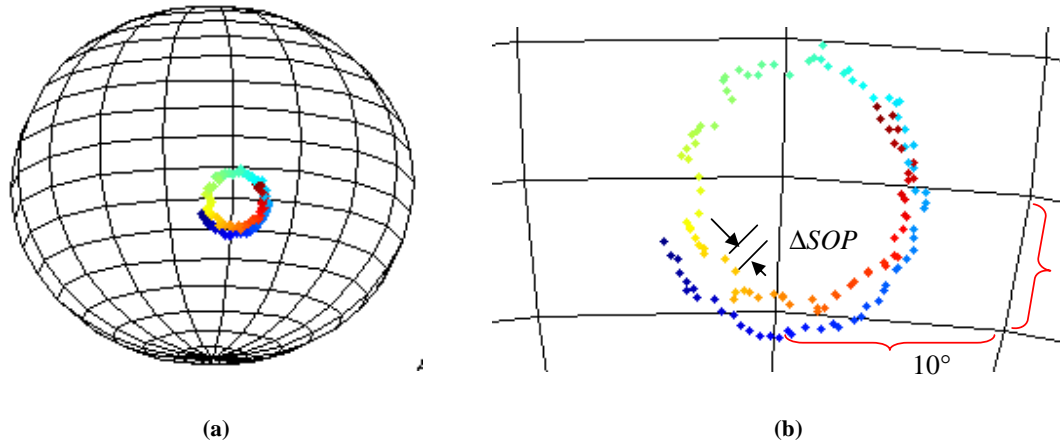


Figure 4.5 The output SOP measurement of one-piece PMF with 96.9cm length. (a) the output SOP traces a small circle on the Poincaré sphere. (b) Zoom in the output SOP on the Poincaré sphere to see the differential SOP vector ΔSOP

Figure 4.5 is the output SOP measurement of the same one-piece PMF as in Figure 4.4. The only difference is that we give a different fixed input SOP for all the frequencies. The output SOP is near to one of the birefringence axis, or the PSP direction, and thus the output SOP trace a small circle on the Poincaré sphere. In this case, the differential SOP vector ΔSOP is as small as the error of ΔSOP , and the circle is distorted significantly. It is obvious that we can hardly get accurate PMD vector from this kind of ΔSOP .

4.2 Data fitting and differential size choosing.

The differential SOP vector is very small, so that error in the measurement can ruin the calculation result of PMD vector. We consider three ways to reduce the effect of measurement error:

- (i) Use data fitting technique to reduce the measurement error.

- (ii) Choose larger differential size $\Delta\omega$, so that the differential SOP vector $\Delta SOP(\omega) = SOP(\omega + \Delta\omega) - SOP(\omega - \Delta\omega)$ is large enough compare to the measurement error.
- (iii) Combine (i) and (ii).

We will study these three cases by simulation and choose a suitable one.

4.2.1 Data fitting

Our purpose is to use data fitting to reduce the error of ΔSOP . In this thesis, we use polynomials of 1 degree to fit the data in a least-squares sense. For example, a series of number y_1, y_2, \dots, y_n is fitted by $y_n = a_1 n + a_0$. In other words, if we plot y_n vs. n in a plane, they are a series of points, and we use straight line to fit this series of points.

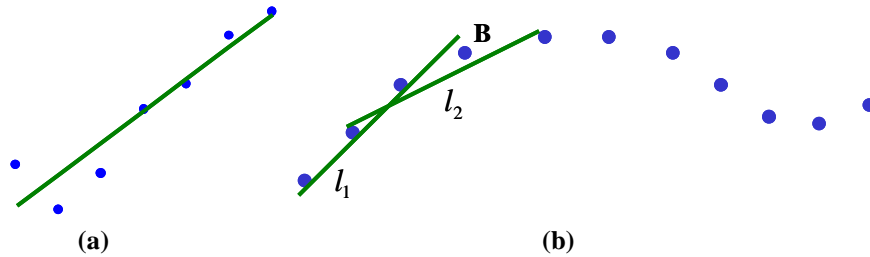


Figure 4.6 (a) fit a polynomial of degree 1 to data. (b) fit a polynomial of degree 1 to every 4 continuous points.

Figure 4.6 (a) shows an example of the fitting of 7 points. The data is smoothed significantly. We also noticed that the fitting is quite different from the original data. If these points are measurement results with error of unknown magnitude, it is hard to say that the smooth data obtained from this fitting has less error than original data.

In our measurement, we have 128 points, and these points sometimes trace a complicated curve. Thus, it is reasonable to fit the data piece by piece rather than use one straight line to fit all the points, and in each piece, data are approximately on a line. We also need to sew these pieces together smoothly.

Due to all above considerations, we choose to fit every N continuous point and average them. The choosing of N depends on the measurement data. If the error of ΔSOP is large, we should choose large N . While if ΔSOP is large, we choose small N to make sure this N points are still approximately on a line. This method can introduce small extra error to the 'real' measurement data while reducing the noise. As shown in Figure 4.6 (b), we fit a straight line to every continuous 4 points. Line l_1 fit the points

from No.1 to No.4, while line l_2 fit the points from No. 2 to No.5. B is the No.4 point. We can see that point B is below l_1 and above l_2 . By averaging, the final fitting result at point B is approximate to B.

In our experiment, we measure the intensity of four SOP components $I_{0^\circ}, I_{90^\circ}, I_{45^\circ}, I_{RHC}$ and calculate the Stokes vector (S_1, S_2, S_3) . The SOPs on the Poincaré sphere are points in three-dimension space. We can also use two angle ϕ and θ to express a certain SOP, as shown in Figure 4.7. Thus when we consider applying data fitting on the measured SOP, we try these two schemes:

- (i) Fit each component of the Stokes vector (S_1, S_2, S_3) respectively.
- (ii) Fit angle ϕ and θ respectively.

Actually we are supposed to fit the SOP itself rather than fit its parameters respectively, but we can not find a math tool to fit 3-D points directly and have to take these two schemes. Scheme (ii) seems better than scheme (i), because only two parameters are fitted respectively. However later we find that scheme (ii) can introduce big error. In this scheme first we transform the Stokes vector expression into ϕ and θ , and then fit these two parameter respectively. For the north or the south pole, angle ϕ is arbitrary. So for the point near the north of the south pole, angle ϕ has large error, and this error can affect the data fitting. As shown in Figure 4.8, the points on the Poincaré sphere is the measured SOP, and the black curve is the fitting result after we fit ϕ and θ respectively. We can see that thought this fitting works for the points far from the pole, the error caused by the fitting is significant for the points near to the pole. So we choose scheme (i) rather than scheme (ii). We will use simulation to confirm scheme (i) in chapter 4.2.3.

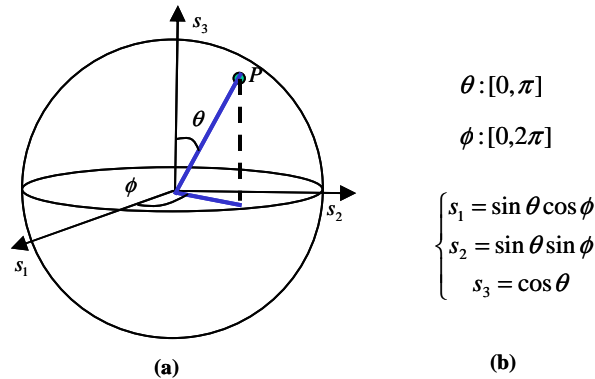


Figure 4.7 Use two angles to express SOP. (a) Angle ϕ and θ of a certain SOP. (b) The relation between ϕ, θ and Stokes vector.

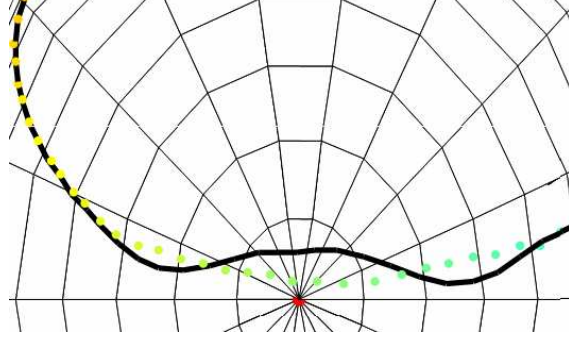


Figure 4.8 Apply data fitting to angle ϕ and θ respectively. The points are measured SOP on the Poincaré sphere, and black curve is the fitting curve.

4.2.2 Differential size choosing

We can also choose large differential size to enlarge ΔSOP to reduce the effect of error of ΔSOP . Assume that the frequency span on each pixel is $\Delta\omega$, if we choose the differential size as $M\Delta\omega$ (M is an even number), the ΔSOP for a certain frequency ω_0 is written as in the equation $\Delta SOP(\omega_0) = SOP(\omega_0 + \frac{M}{2}\Delta\omega) - SOP(\omega_0 - \frac{M}{2}\Delta\omega)$.

Figure 4.9 shows ΔSOP in the case of differential size $2\Delta\omega$ and $6\Delta\omega$ respectively. The latter one is more robust to measurement error. However, the differential size shouldn't be too large. We need to make sure that within the differential size the PSP is reasonably constant, otherwise the PMD vector calculated from ΔSOP can have noticeable error. More details are show in the simulation in the chapter 4.2.3.

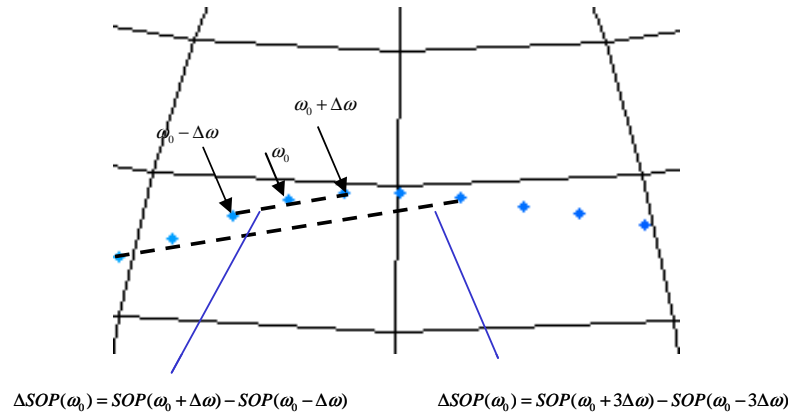


Figure 4.9 $\Delta SOP(\omega_0)$ for different differential sizes.

4.2.3 Simulation

We use simulation to study the effect of data fitting and differential size choosing. In the simulation, the fiber under test is the concatenation of two pieces of PMF with the following parameters:

- (i) The length of the first PMF is 47.5cm, and the second one 67cm.
- (ii) Their slow axes are 45° apart.
- (iii) The differential refractive index is $\Delta n = 4.15 \times 10^{-4}$.

We give four different fixed input SOP ($0^\circ, 90^\circ, 135^\circ, RHC$) for all frequencies, and calculate the corresponding four output SOP sets. Just like our measurement in the lab, we give 128 samples in the wavelength span from 1543.45nm to 1553nm. The PSP of this two-piece PMF in this span traces a circle on the Poincare sphere and the trace is a little bit more than one circle. We add noise to the output SOPs, and then apply data fitting to them. The noise added is in this form:

$$S_i' = S_i(1 + r \times error), \quad i = 1, 2, 3 \quad (4.1)$$

Where r is a random variable uniformly distributed from -1 to 1, $error$ defines the size of the noise. S_i' and S_i are the Stokes vector elements after and before adding noise.

As mentioned in chapter 4.2.1, we fit the three components of the Stokes vector respectively. More specifically, we use one degree polynomial to fit every N continuous points and average them to get the final fitting. After data fitting, we choose a differential size $M\Delta\omega$ to calculate the differential SOP vectors and use them to calculate the output PSP (The calculation details are in chapter 4.3). By changing N and M, we can see their effects in PMD vector calculation.

We also define a parameter D to describe the error of the PSP:

$$D = \sqrt{\frac{\sum_{i=1}^n \theta_i^2}{n}} \quad (4.2)$$

Where θ_i is the angle between the theoretical PSP and the calculated PSP, n is the number of all the frequencies. D is the root mean square of θ_i .

In Figure 4.10, we add random noise to the output SOP with the parameter $error = 0.2$, which defines significant noise. In Figure 4.10 (a), we don't apply data fitting, and just use the smallest differential $2\Delta\omega$ as the differential size to calculate the PSP for each frequency, and show them on the Poincare sphere. We use different color points to indicate different frequencies. To make a comparison, we display the calculated PSP and the real PSP on the same Poincare sphere. We can see that the

calculated PSP is far from the real PSP. The root mean square of the angle between the calculated PSP and the real PSP is $D = 17.4^\circ$. In Figure 4.10 (b), we choose $N=10$, and $M=2$, which means that we apply data fitting to every 10 continuous points while not choosing larger differential size. We can see that, the calculated PSP is significantly improved. In this case $D = 2.5^\circ$. In Figure 4.10 (c), we don't apply data fitting, but choose larger differential size $10\Delta\omega$. The calculated PSP is also improved, with $D = 4.3^\circ$. Both methods improve the PSP calculation a lot.

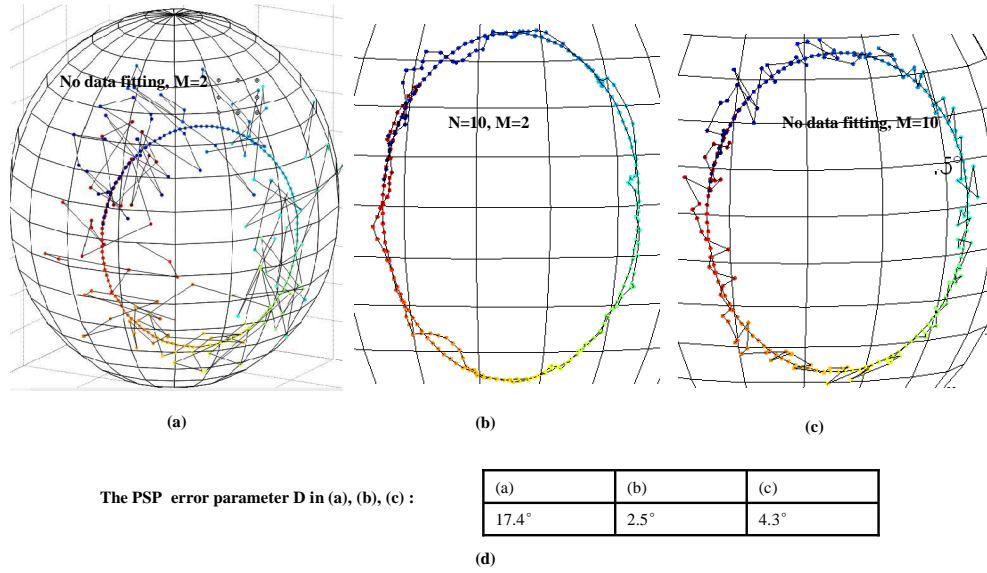


Figure 4.10 The effect of data fitting and differential size choosing on PSP calculation. The size of the noise added: $error = 0.2$. The points on a circle are the theoretical PSPs. Others are from PMD calculation. (a) no data fitting, smallest differential size $2\Delta\omega$ ($M=2$). (b) with data fitting ($N=10$), smallest differential size $2\Delta\omega$ ($M=2$). (c) No data fitting, differential size $10\Delta\omega$ ($M=10$). (d) The PSP error parameter D ($^\circ$) of (a), (b), (c).

We note that though the noise given in Figure 4.10 ($error = 0.20$) is very large (In our experiment $error = 0.037$. We will talk about the method to estimate $error$ in this chapter later.), these two methods reduce the effect of noise efficiently. They are very robust to noise. However, they also have defects. The first defect is that these methods cannot recover the real PSP even if the noise is zero. As shown in Figure 4.11, we add no noise to the output SOP. In Figure (a), we choose $N=10$, and $M=2$ (smallest differential size), the error between the calculated PSP and the real PSP is $D = 0.24^\circ$. This error is very small. In Figure (b), we choose large differential size ($M=10$) without data fitting, the error is $D = 0.7^\circ$, which has become noticeable. The reason is that when we choose large differential size $10\Delta\omega$, in the span the PSP changes noticeably and so the SOP

trajectory is not an accurate arc. As a result, the differential SOP $\Delta SOP(\omega_0) = SOP(\omega_0 + 5\Delta\omega) - SOP(\omega_0 - 5\Delta\omega)$ is not strictly orthogonal to the PSP at frequency ω_0 . We also try to choose $N=10$ and $M=10$ simultaneously. In this case the error is even larger: $D = 0.75^\circ$.

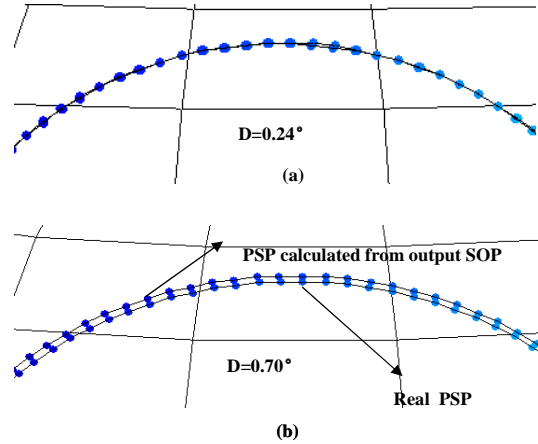


Figure 4.11 PSP calculated from output SOP with no error. (a) $N=10$, and $M=2$ (smallest differential size). (b) no data fitting, $M=10$

We also simulate another case with noise. We choose $error = 0.05$. Firstly we choose no data fitting and no larger differential size. The error of PSP is $D = 4.22^\circ$. Secondly we choose $N=10$ with no larger differential size. We get the error $D = 0.68^\circ$. Then we choose $M=10$ without data fitting, and get $D = 1.11^\circ$. If we choose $N=10$ and $M=10$, the PSP error is $D = 0.80^\circ$. In conclusion, applying data fitting only is the best choice in this case.

The second defect of these two methods is that they treat the edging frequencies unfairly. As for the data fitting, say $N=10$, we fit every continuous 10 points and average to get the final fitting result. However, the first 10 and the last 10 are only fitted less than 10 times which the middle points enjoy. So the fitting effect is less for these points. If we choose large differential size, say $M=10$, we can't get ΔSOP of the first 5 and the last 5 points. From these, we know that N and M shouldn't be too large.

By comparing these two methods we have the following points of view:

- (i) They are both efficient and robust in reducing the effect of noise
- (ii) In the case of no noise, choosing larger differential size may introduce noticeable error. While data fitting only introduce minor error.
- (iii) If choosing larger differential size introduce noticeable error, then using these two methods simultaneously doesn't work better than using data fitting only.

(iv) They neither give good result for the edging points

From these points, we tend to choose only data fitting in priority to reduce the effect of measurement error. Only if the differential SOP vector is too small so that we can not reduce the measurement error by data fitting only, we consider choosing larger differential size simultaneously.

We estimate the measurement error by the relation between noise and data fitting effect on the SOP. In our simulation, we choose $N=10$ and apply data fitting to the output SOP with 8 different size noise. ($error=0.01, 0.02, \dots, 0.08$). We calculate the root mean square of angle between the SOP after and before fitting for all the frequencies,

say $D' = \sqrt{\frac{\sum_{i=1}^n \theta_i'^2}{n}}$. We plot the figure of D' vs. $error$, as shown in Figure 4.12. The

points are approximately on a straight line. In our experiment, our fiber under test is a two-piece PMF having the same parameters as in the simulation, and the frequency span on the 128 CCD camera pixels is also consistent with the simulation. We measure the output SOP, and apply data fitting ($N=10$), and get $D' = 0.365^\circ$. According to the fitting line in Figure 4.12, $error$ is 0.0373 for our measurement.

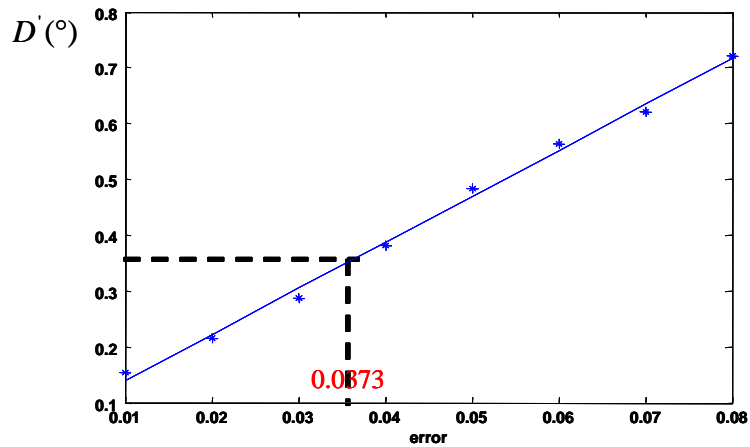


Figure 4.12. Plot of D' vs. $error$.

This method to evaluate the measurement error is not strict, because the measurement error has different properties from the random noise we simulated. For example, the measurement error caused by the inter-pixel cross talk of camera CCD does not cause the random variation of the measurement. However, this evaluation at least gives us a reference. We use this evaluation in our simulation, and find that the data

fitting on every 10 continuous points ($N=10$) without choosing larger differential size works well. We apply the same data fitting on our experiment data, and analyze the result.

We calculate PSP from our measurement output SOP and confirm the conclusion from the simulation. Figure 4.13 is the calculation result. The real PSP traces a circle on the Poincare sphere. However, we cannot estimate the exact location of this circle, because the single mode fiber using as leads can shift the location, and moreover the estimation error of the length stop us from determining the location of PSP for different frequencies on the circle. So we just observe the shape of the PSP trace. In (a) we don't apply data fitting ($N=2$) and neither choose larger differential size ($M=2$). The calculated PSP traces a distorted circle with bumps. The distortion is due to the measurement error. In (b), we apply data fitting ($N=10$) while not choosing larger differential size ($M=2$), we can see that the PSP is approximately on a circle. This means that the effect of measurement error is reduced significantly. In (c), we don't apply data fitting ($N=2$) but choosing larger differential size ($M=10$), the effect of measurement error is also reduced obviously. In (d), we put the traces in (b) and (c) together. Furthermore, we add the trace in the case of $N=10$ and $M=10$ simultaneously. It shows that these three trace are very close. In conclusion, applying data fitting only is enough in this case. This also shows that though the error estimation is not strict, it still works anyway.

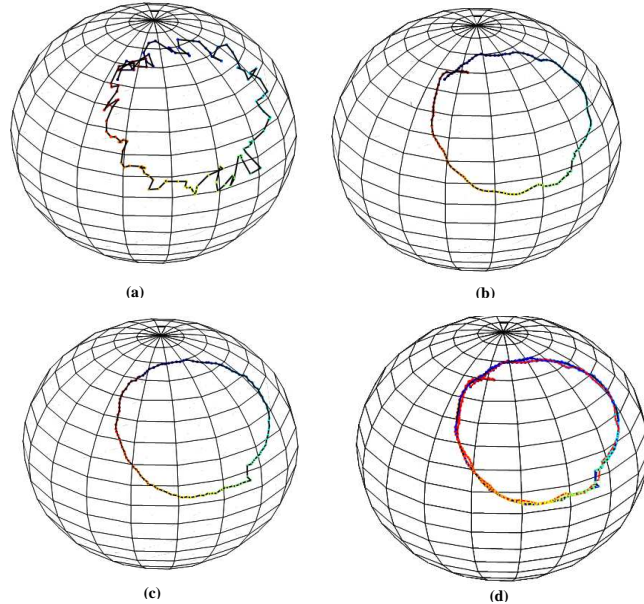


Figure 4.13 PSP calculated from measured output SOP. The fiber under test and frequency span as well as the sample numbers is the same with those in the simulation. (a) No data fitting ($N=2$) and smallest differential size. ($M=2$). (b) $N=10$, $M=2$. (c) No data fitting and $M=10$. (d) $N=10$ and $M=2$, and PSP in (b) and (c) are also plotted in this figure).

4.3 PMD Vector calculation

PMD vector $\vec{\tau} = \Delta\hat{p}$ contains the differential group delay $\Delta\tau$ and the slow PSP \hat{p} . We can calculate output PMD vector from the output SOP measured. After we measure the four different output SOP sets and apply data fitting to them, we choose $2\Delta\omega$ as differential size to calculate the differential SOP vectors for each frequency $\Delta SOP(\omega_0) = SOP(\omega_0 + \Delta\omega) - SOP(\omega_0 - \Delta\omega)$. This differential SOP vector is orthogonal to the output PSP, and this property holds for all the output SOP sets. So if we choose a pair of differential SOP vector $\Delta SOP_i(\omega_0)$ and $\Delta SOP_j(\omega_0), (i \neq j)$ from different output SOP set, their cross product $\Delta SOP_i(\omega_0) \times \Delta SOP_j(\omega_0)$ gives the direction of output PSP [3].

We can decide the differential group delay after the PSP direction is determined. In the frequency span $2\Delta\omega$ the output SOP is approximately on a circle with the PSP as its axis. Assuming that within the frequency span $\partial\omega$, the angle of the SOP arc is ϕ , we can calculate the differential group delay as $\Delta\tau = \left| \frac{\partial\phi}{\partial\omega} \right|$.

We have four output SOP set, so we have six combination of $\Delta SOP_i(\omega_0) \times \Delta SOP_j(\omega_0)$, and four $\left| \frac{\partial\phi}{\partial\omega} \right|$. We can average to get more accurate PSP and differential group delay.

However, we can't decide whether the direction of $\Delta SOP_i(\omega_0) \times \Delta SOP_j(\omega_0)$ is the slow PSP or fast PSP. We solve this problem by calculating PMD vector as a whole rather than calculating PSP and DGD respectively. From the relation between the output SOP and the output PMD vector: $\frac{dS_{out}(\omega)}{d\omega} = \vec{\tau}(\omega) \times S_{out}(\omega)$ and the vector identity $a \times (b \times c) = (a \bullet c)b - (b \bullet a)c$, we get:

$$\begin{aligned} \frac{dS_i}{d\omega} \times \frac{dS_j}{d\omega} &= (\vec{\tau} \times S_i) \times (\vec{\tau} \times S_j) \\ &= [(\vec{\tau} \times S_i) \bullet S_j] \vec{\tau} - [\vec{\tau} \bullet (\vec{\tau} \times S_i)] S_j \\ &= [(\vec{\tau} \times S_i) \bullet S_j] \vec{\tau} \\ &= \left[\frac{dS_i}{d\omega} \bullet S_j \right] \vec{\tau} \end{aligned}$$

Where S_i is the SOP vector in stokes space for one of the four output SOP set. Thus we immediately express the PMD vector from a pair of output SOP by Equation (4.3):

$$\vec{\tau} = \frac{\frac{dS_i}{d\omega} \times \frac{dS_j}{d\omega}}{\frac{dS_i}{d\omega} \bullet S_j} \quad (4.3)$$

In our calculation $\frac{dS_i(\omega_0)}{d\omega}$ is $\frac{SOP_i(\omega_0 + \Delta\omega) - SOP_i(\omega_0 - \Delta\omega)}{2\Delta\omega}$.

Though we have applied data fitting to the measured output SOP before PMD calculation, big errors occur in two cases:

- (i) The cross product of $\Delta SOP_i(\omega_0) \times \Delta SOP_j(\omega_0)$ is too small, or in other words, the angle between $\Delta SOP_i(\omega_0)$ and $\Delta SOP_j(\omega_0)$ is too small.
- (ii) The output SOP $SOP_i(\omega_0)$ is near to one of the slow and fast output PSP.

We use the following criteria to choose good pairs from the bad pairs before averaging [4]:

$$\frac{|\Delta SOP_i(\omega_0) \times \Delta SOP_j(\omega_0)|}{|\Delta SOP_i(\omega_0)| |\Delta SOP_j(\omega_0)|} > 0.707, \quad \text{and}$$

$$|\hat{p}_{ij}(\omega_0) \times SOP(\omega_0)_i| > 0.707,$$

where $\hat{p}_{ij}(\omega_0)$ is the direction of $\vec{\tau}$ calculated by Equation (4.3)

4.4 PMD Vector measurement result

We calculate PMD vector and compare the result to the estimation by PMD vector concatenation rules. For the estimation, we measured the differential refractive index Δn using our setup. We also need to measure the length of the each piece PMF. However, the length measurement has error about 1 millimeter, which is a significant fraction of the beat length of the PMF. This length error make it impossible to estimate the PMD vector of n piece PMF ($n > 3$). So we only analyze three kind of fiber under test: one-piece PMF, two-piece PMF and three-piece PMF. We use single mode fiber as lead to insert these PMF into our measurement setup. As a result, the output PSP vs. frequency is rotated by the single mode fiber on the Poincare sphere as a whole with its shape unchanged. So we can only estimate the whole shape of the output PSP vs. frequency rather than the exact PSP for each frequency.

4.4.1 Measurement of differential refractive index Δn

We splice PMF pieces and use them as device under test. To evaluate our PMD vector measurement, we plan to compare the result with the estimation from the PMD vector concatenation rule. So we need to know the differential refractive index Δn of the PMF.

We can measure this in our setup. The DUT is one-piece PMF with 96.9cm length. We give a fixed input SOP for all frequency, and measure the output SOP. It traces a circle on the Poincarè sphere. So any one component of the Stokes vector is a sinusoidal function, as shown in our measurement result in Figure 4.14. This sinusoidal function has a period of $\Delta\omega_p = \frac{2\pi c}{l\Delta n}$, where l is the length of this one-piece PMF. Obviously by this relation we can easily calculate Δn , and the result is $\Delta n = 4.15 \times 10^{-4}$.

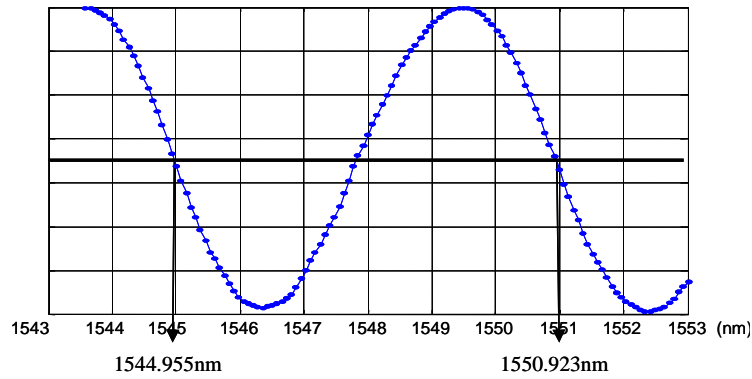


Figure 4.14 The component s_1 of output SOP Stokes vector (s_1, s_2, s_3) vs. wavelength.

4.4.2 One-piece PMF

For one-piece PMF, the output PMD vector is independent of frequency. This means the output PSP vs. frequency is a point on Poincare sphere, and the DGD vs. frequency is constant. We estimate the DGD from the length of PMF l and the differential refractive index Δn :

$$\Delta\tau = \frac{\Delta n l}{c} \quad (4.4)$$

As for PSP, the single mode fiber leads of one-piece PMF rotate it on the Poincare sphere so that we cannot estimate the exact location. We just check if it converges to one point on the Poincare sphere.

We measured a series of one-piece PMF of different length. The wavelength range over 128 pixels is from 1543.45nm to 1553nm. Differential refractive index of PMF is $\Delta n = 4.15 \times 10^{-4}$. Our PMD vector measurement result is as follows:

(1) One-piece PMF with length $l = 17.8\text{cm}$.

The output SOP is about one third of a circle on the Poincare sphere. Figure 4.15 (a) shows one of the four output SOP sets. Zoom in the SOP, we can see that, the differential SOP is very small, and the fluctuation is obvious. We apply data fitting to every 10 continuous points, as shown in Figure 4.15 (b), the output SOP is smoothed significantly while remaining its whole shape.

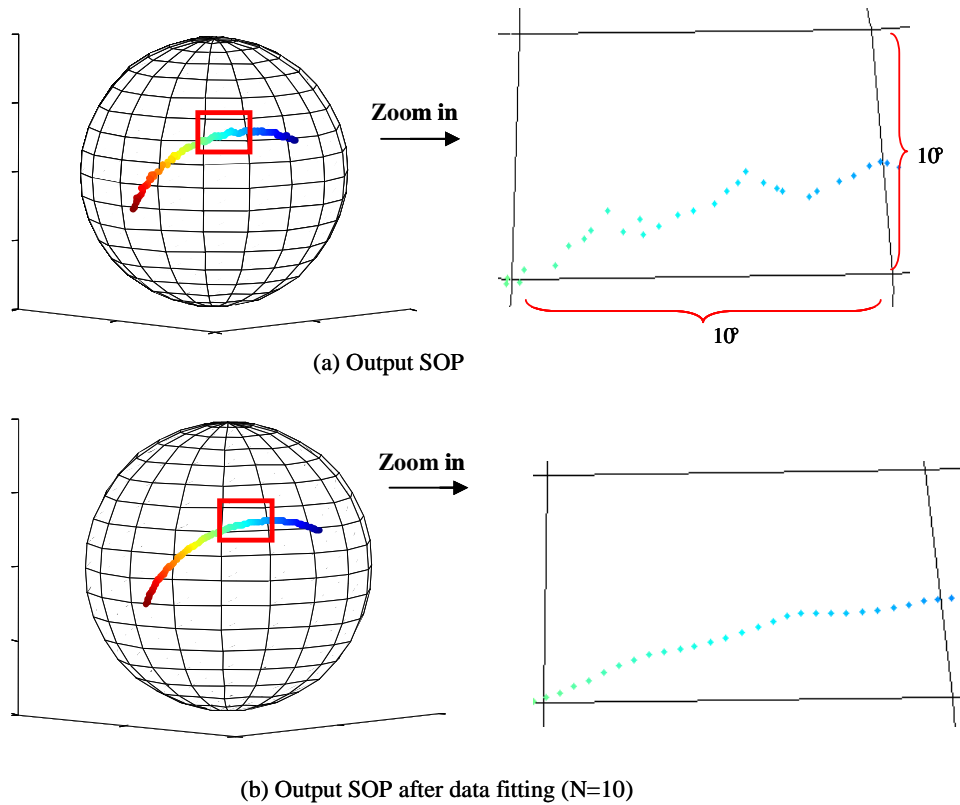


Figure 4.15 (a) Output SOP measured. (b) Output SOP after data fitting. (N=10)

We calculate the PMD vector from the fitting data (N=10), as shown in Figure 4.16:

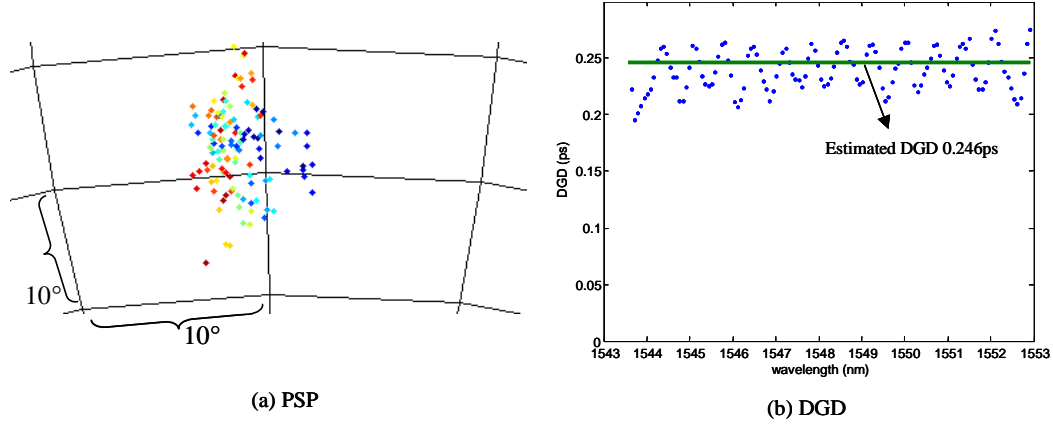


Figure 4.16 PMD calculated from fitting data ($N=10$) with differential size $2\Delta\omega$. (a)PSP
(b) DGD

The PSP vs. frequencies is estimated to converge to one point, and the DGD is estimated to be $\Delta\tau = \frac{\Delta nl}{c} = \frac{4.15 \times 10^{-4} \times 0.178}{3 \times 10^8} = 0.246 \times 10^{-12}$ second. Nevertheless, the result in Figure 4.16 shows obvious error. As for the PSP for different frequencies, they cover a range about $10^\circ \times 10^\circ$ on the Poincare sphere (each grid is $10^\circ \times 10^\circ$). As for DGD, the root mean square error is 15.4% of the estimated DGD. The mean DGD for all frequencies is 0.244 ps , with the standard deviation $9\% \times 0.244 \text{ ps}$. This is because differential SOP vector ΔSOP is too small so that the measurement error can compare to it. As a result, even if we apply data fitting to smooth the data, there still exists residual error.

Now we try to choose larger differential size $10\Delta\omega$ for the fitting data in order to reduce the effect of measurement error. In this case of one-piece PMF, since the PMD vector is estimated to be independent of frequency, so large differential size won't introduce extra error. Figure 4.17 shows that PMD vector calculation is improved significantly. In (a), the output PSP cover a range about $3^\circ \times 3^\circ$ on the Poincare sphere. In (b), the measured DGD is very close to the estimated value. The root mean square error is 2.2% of the estimated DGD. The mean DGD for all frequencies is 0.242 ps with the standard deviation $3.2\% \times 0.242 \text{ ps}$.

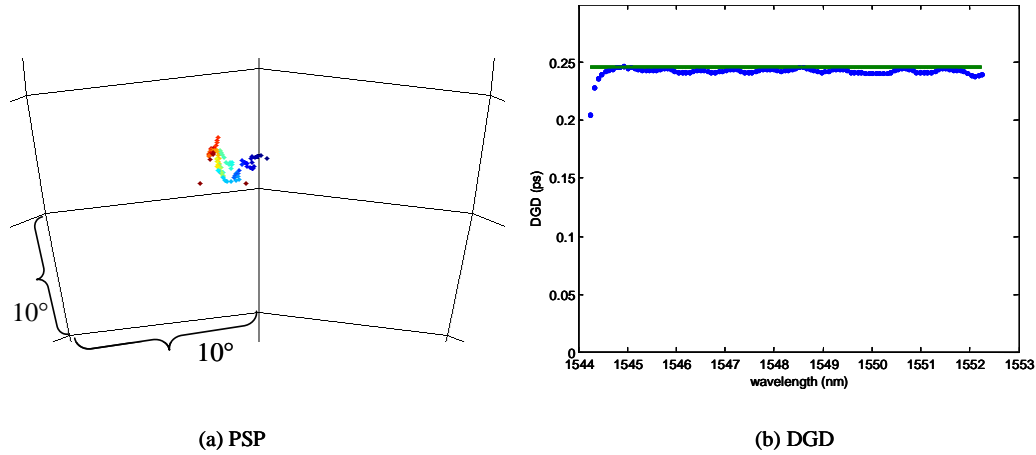


Figure 4.17 PMD calculated from fitting data ($N=10$) with larger differential size ($10\Delta\omega$). (a)PSP (b) DGD

(2) One-piece PMF with length $l = 40.9\text{cm}$.

The output SOP traces about two thirds of a circle on the Poincare sphere. Figure 4.18 (a) shows the measurement. Zooming in on the figure, we can see that the differential SOP is larger than in Figure 4.15 (a), and the trace is also smoother. This is because the error becomes smaller compare to the differential SOP. The data fitting ($N=10$) result is shown in Figure 4.18 (b). The trace is smoothed while its shape is retained.

We calculate the PMD vector from the fitting data ($N=10$) without larger differential size (just choose $2\Delta\omega$). The result is shown in Figure 4.19. In (a), the PSP covers a range about $6^\circ \times 6^\circ$. In (b), the estimated DGD is 0.566ps , and the root mean square of the calculated DGD is 6.5% of the estimated DGD. The mean DGD for all frequencies is 0.571ps with the standard deviation $6.4\% \times 0.571\text{ps}$.

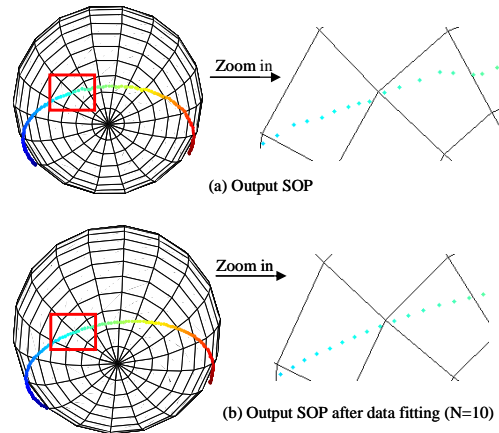


Figure 4.18 Output PSP for one-piece PMF with length $l = 40.9\text{cm}$ (a) measured output SOP (b) Output SOP after data fitting ($N=10$)

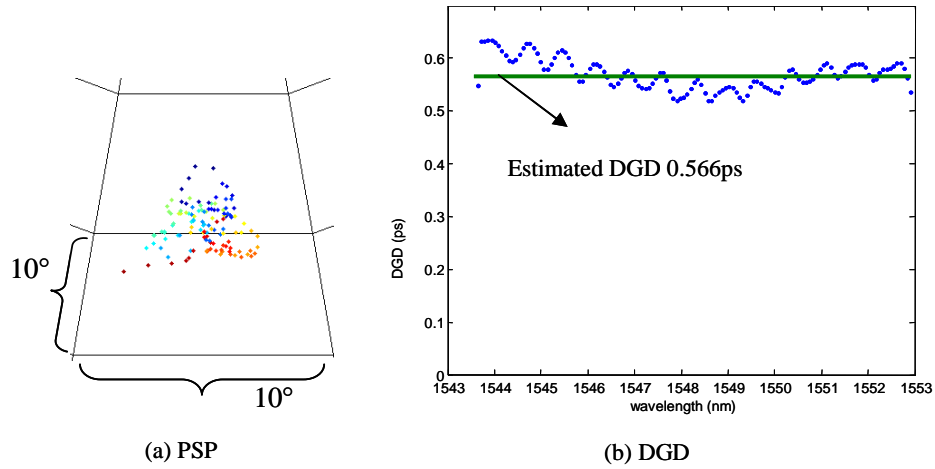


Figure 4.19 PMD calculated from fitting data (N=10). (a)PSP (b) DGD

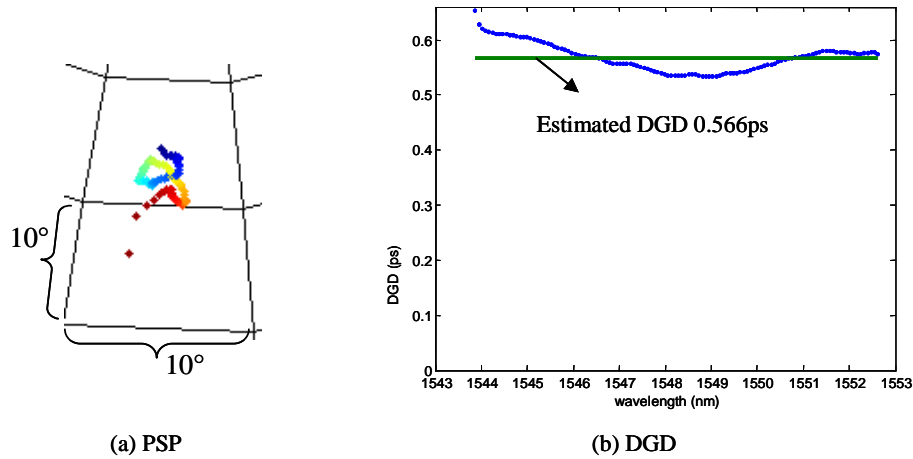


Figure 4.20 PMD calculated from fitting data (N=10) with larger differential size ($10\Delta\omega$). (a)PSP (b) DGD

To improve the calculation, we can also choose larger differential size ($10\Delta\omega$) on the fitting data without introducing extra error. The result is shown in Figure 4.20. In Figure 4.20 (a), the PSP covers a range about $4^\circ \times 4^\circ$. In Figure 4.20 (b), the root mean square of the DGD is about 4.53% of the estimated DGD. The mean DGD for all frequencies is 0.568ps , with the standard deviation $4.5\% \times 0.568\text{ps}$. The PMD calculation result is improved by choosing larger differential size, but the improvement is not as much as in (1). This is because the differential SOP is larger in this case so that data fitting itself is approximate to be enough.

(3) One-piece PMF with length $l = 96.9\text{cm}$.

We apply data fitting (N) on the measurement, and calculate the PMD vector. The result is shown in Figure 4.21. In (a), the PSP cover a range about $5^\circ \times 5^\circ$, and in (b) the root mean square of DGD is 5.4% of the estimated DGD 1.340ps. The mean DGD for all frequencies is 1.345ps, with the standard deviation $5.4\% \times 1.345\text{ps}$. We also choose larger differential size ($10\Delta\omega$) to calculate PMD from the fitting data. The result is shown in Figure 4.22. In (a), the PSP cover a range about $5^\circ \times 5^\circ$. In (b), the root mean square of DGD is 4.7%. The mean DGD for all frequencies is 1.345ps, with the standard deviation $4.65\% \times 1.345\text{ps}$. Because the differential SOP between two camera pixel is even larger here than in (2), so choosing larger differential size on the fitting data or not doesn't make significant difference.

We observe fluctuation of DGD both in Figure 4.20 and Figure 4.22. The fluctuation in Figure 4.22 is even larger. We expect this due to the inter-pixel cross talk of CCD camera. The beam size covers two pixels, so the larger is the SOP change between two continuous pixels; the larger is the cross talk. The measurement error caused by cross talk can hardly removed by data fitting and choosing larger differential size.

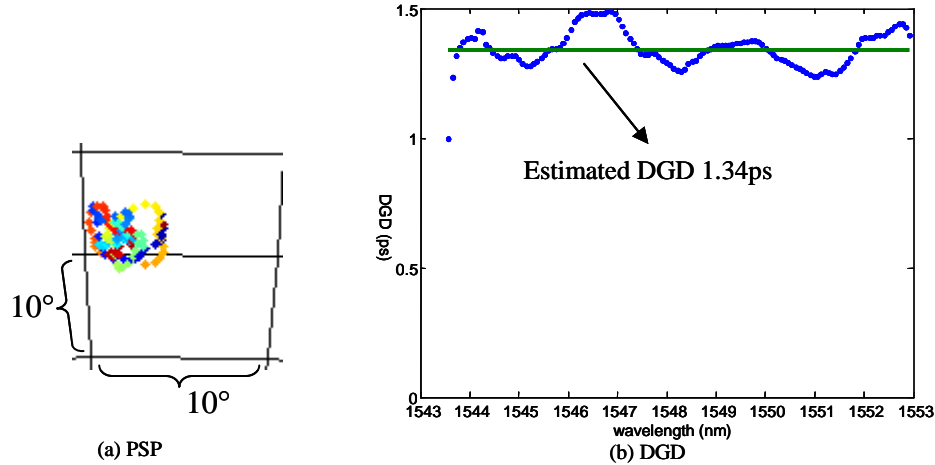


Figure 4.21. PMD calculated from fitting data (N=10). (a)PSP (b) DGD

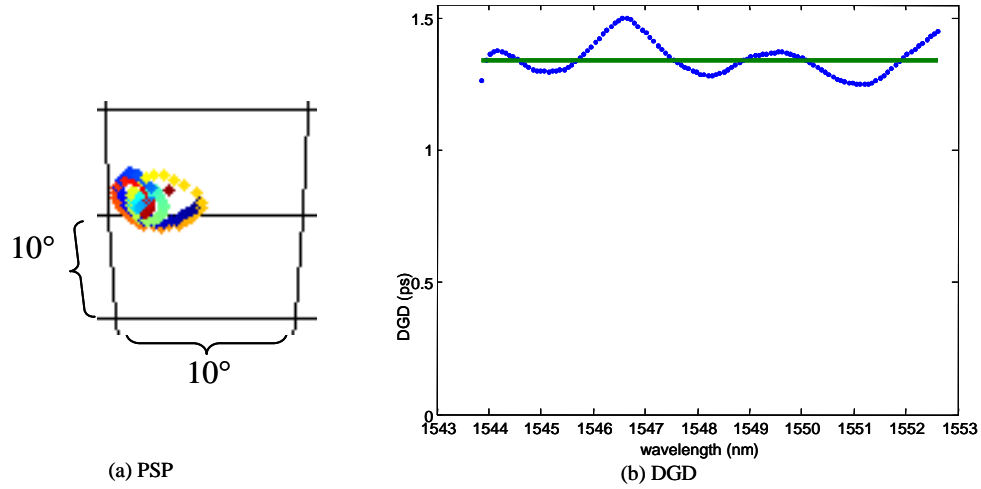


Figure 4.22 PMD calculated from fitting data ($N=10$) with larger differential size ($10\Delta\omega$). (a)PSP (b) DGD

4.4.3 Two-piece PMF

In this experiment, we calculate the PMD vector from the output SOP and compare DGD and PSP with the estimated value. The PMD vector of two-piece PMF has the following properties:

- (i) PSP vs. frequency traces a circle on the Poincare sphere.
- (ii) The DGD is constant for all frequency.

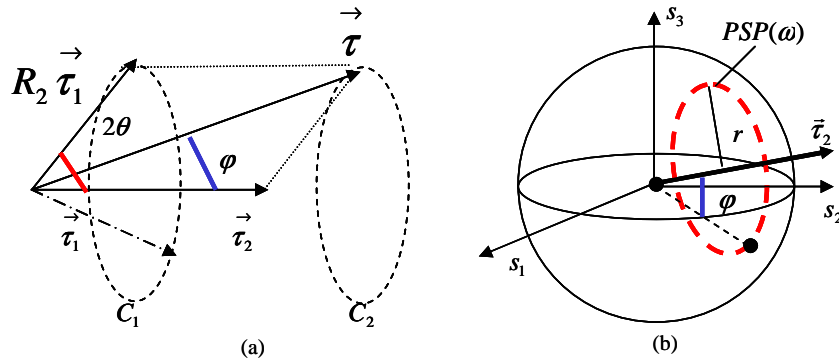


Figure 4.23. (a) the PMD concatenation rule.(b)output PSP vs. frequency for two-piece PMF traces a circle on the Poincare sphere.

These properties are interpreted by Figure 4.23. Two PMF piece with length l_1 and l_2 are spliced together. The angle between their slow axes is θ , the PSP vector of them is $\vec{\tau}_1$ and $\vec{\tau}_2$ respectively, and the rotation matrix (in stokes space) is R_1 and R_2 . The total

PMD vector is $\vec{\tau}$. (a) gives a visualization of concatenation rule of PMD vector. In the Stokes space, the angle between $\vec{\tau}_1$ and $\vec{\tau}_2$ is 2θ . $\vec{\tau}_1$ is rotated by the rotation matrix of the second PMF around $\vec{\tau}_2$. For different frequency, the rotation is different, so that the end of the vector $R_2(\omega)\vec{\tau}_1$ traces on circle C_1 . Then $R_2(\omega)\vec{\tau}_1$ and $\vec{\tau}_2$ is added to get the total PMD vector $\vec{\tau}$. The end of this total vector is on circle C_2 . It has the same length for all the frequency. The angle between $\vec{\tau}$ and $\vec{\tau}_2$, say φ , is determined by 2θ and l_1/l_2 . On the Poincare sphere, the total PSP is on a circle with radius $r = \sin \varphi$, as shown in (b). We use the angle φ to describe the radius.

From the analysis above, the PMD vector can be theoretically estimated if we know the following parameters: l_1 , l_2 , θ , the slow axis of each PMF and the differential refractive Δn . However, in our experiment, we have the following problems:

- (i) SMF is used as lead, so that the output PSP is rotated as a whole on the Poincare sphere in an unknown way.
- (ii) The measurement of l_2 has error ~ 1 millimeter due the ruler we use. This little length difference affects the rotation matrix R_2 significantly. Because the rotation matrix for a certain varies with the fiber length and repeat itself after a beat length (~ 3 millimeter in our experiment). As a result, we can't determine the accurate location of PSP for a certain frequency on the PSP trajectory.
- (iii) The span $\Delta\omega$ within which the PSP traces exactly one circle also satisfies Equation (2.17), and it is: $\Delta\omega = \frac{2\pi c}{\Delta n l_2}$, which is determined by l_2 .

The key parameters of our experiment are:

- (i) The wavelength span is 1542.9~1556.9 nm (1.748THz) over 128 camera pixels, or 13.6GHz/pixel.
- (ii) The beam size covers 2 pixels.
- (iii) The differential refractive index of the PMF is $\Delta n = 4.15 \times 10^{-4}$.
- (iv) The angle between the two birefringence axes is 45° (given by the fiber splicer, and need to be checked).
- (v) The length of the second PMF is 70 cm. This makes the output PSP traces about 1.68 circles. $(1.748 \times 10^{12} \text{ rad/s}) / \frac{c}{\Delta n l_2} = 1.68$
- (vi) The length series of the first PMF is: (1)102 cm (2)81 cm (3)70 cm (4)60 cm (5)50 cm. (We cut back the first PMF to perform 5 experiments.)

We apply data fitting ($N=10$) on the output SOP and choose the smallest differential SOP size $2\Delta\omega$ to calculate PMD vector. Figure 4.24 shows the result for fiber No.3 (70cm+70cm). We study this PMF first, because the two PMF piece have the same length. So by the PMD vector concatenation rules in Figure 4.23, $\varphi = \theta$. So we can estimate the angle between the two birefringence axes. In Figure 4.24(a), we show the PSP vs. frequency. The trajectory is on a circle with $\varphi = 39.6^\circ$, and the trajectory is about 1.6 circles. This is close to the estimation value, 1.68 circles. So we take $\theta = \varphi = 39.6^\circ$ rather than the angle given by the fiber splicer ($\theta = 45^\circ$). By this angle, we estimate the DGD to be 1.49ps. As shown in Figure 4.24(b), the DGD fluctuate around 1.49ps with the root mean square error 4.0%. From the calculation, we also get that the mean DGD for all frequencies is 1.489ps, and the standard deviation is $3.98\% \times 1.489ps$. So the estimation of θ is reasonable.

The PMD vector calculation result for all the five measurements are shown in Figure 4.25. In Figure 4.25 (a) PSP for fiber No.1~No.3 are approximately on concentric circles. And just as expected, the PSP for a certain frequency has the similar location on each circle. (We use different color to indicate different frequency.) Figure 4.26, which only contains PSP trajectory of fiber No.1 and No.3, shows this more clearly. In Figure 4.25 (a), PSP for fiber No.4~No.5 are also approximately on concentric circle, but they are rotated away from No.1~No.3. This is because the lead at the second piece PMF side are touched a little bit when I cut back the first PMF piece from fiber No.3 to get fiber No.4. Figure 4.25 (b) shows the DGD measurement result. The straight lines are the estimated DGD in the case $\theta = 39.6^\circ$. The measurement DGD fluctuated around the estimated DGD. We can see that, as we cut back the first PMF, both the radius of the PSP trajectory and the DGD become smaller. The specific numbers are shown in Table 4.1. The estimation on both DGD and PSP is based on $\theta = 39.6^\circ$. We use root mean square of the error from the estimation to describe DGD measurement error. The DGD error in these five cases is in a reasonable range. We also calculate the mean DGD for all frequencies and the standard deviation. They are very close to the estimated DGD and measurement error (based on the estimated DGD) respectively. The angle φ is used to describe the radius of PSP trajectory by $r = \sin \varphi$. The error of φ is also reasonable. We think that the error of φ and DGD arise from the inter-pixel cross talk of the camera CCD. We also note that, if we take the angle between the two axes given by the fiber splicer, $\theta = 45^\circ$, the measurement error of DGD and φ are both as high as 15% in all five cases. Especially the DGD are above the estimation instead of fluctuating around the estimation. So our estimation of θ is much more accurate than the fiber splicer.

Table 4.1
Compare the PMD measurement results and the estimation

PMF No.	1	2	3	4	5
Length (cm)	102+70	82+70	70+70	60+70	50+70
Estimated DGD (ps) by PMD vector concatenation rule	1.85	1.61	1.49	1.39	1.29
Root mean square of difference between measured DGD and estimated DGD (percentage of estimated DGD)	5.4%	5.1%	4.0%	2.9%	4.1%
Mean DGD $\langle \Delta\tau \rangle$ (ps)	1.87	1.61	1.49	1.38	1.30
std of DGD (percentage of $\langle \Delta\tau \rangle$)	5.3%	5.1%	4.0%	2.8%	4.0%
Estimated φ	48.3°	43.0°	39.6°	36.0°	31.8°
Measured φ	48.8°	42.4°	39.6°	38.5°	33.7°
Error of φ	1.0%	1.4%	N/A	4.2%	6.0%

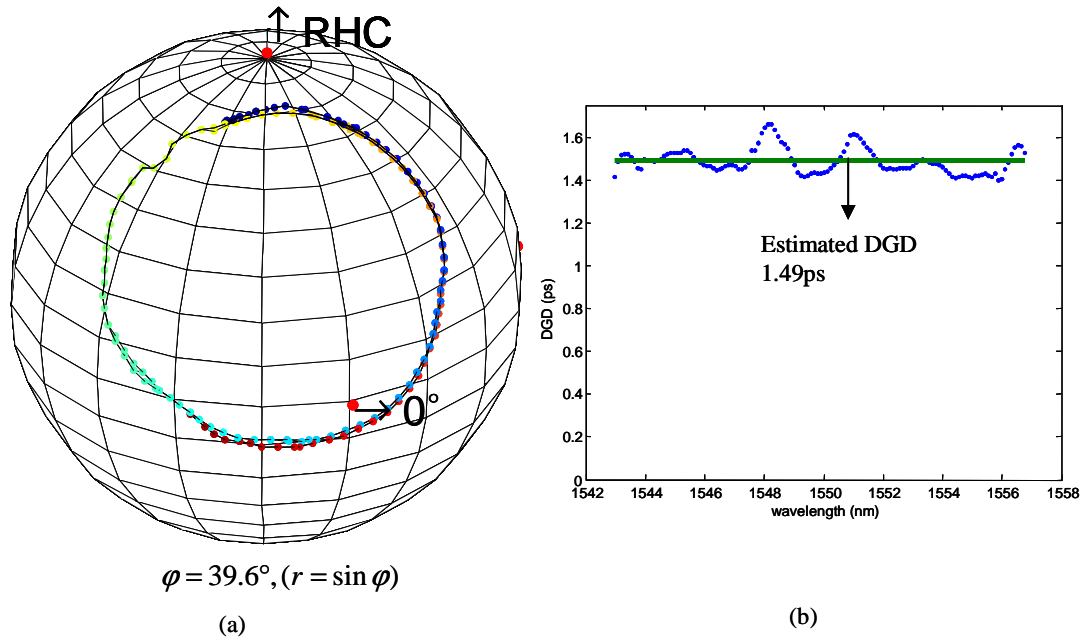


Figure 4.24 PMD vector measurements for PMF No.3 (70cm+70cm). (a)PSP (b) DGD

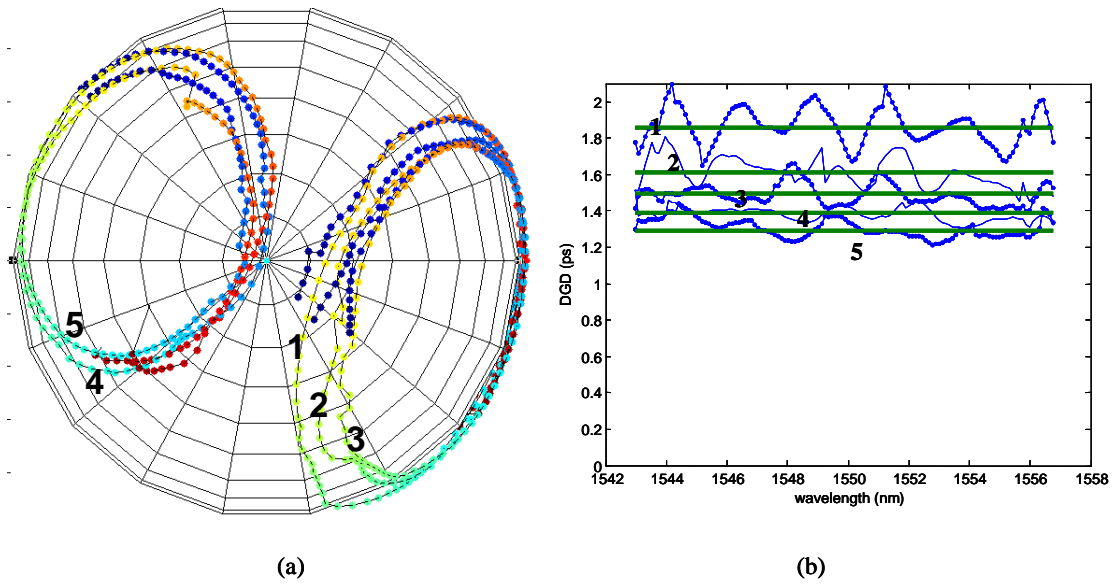


Figure 4.25 PMD vector measurement for fiber No 1~No.5. (a) PSP (b)DGD

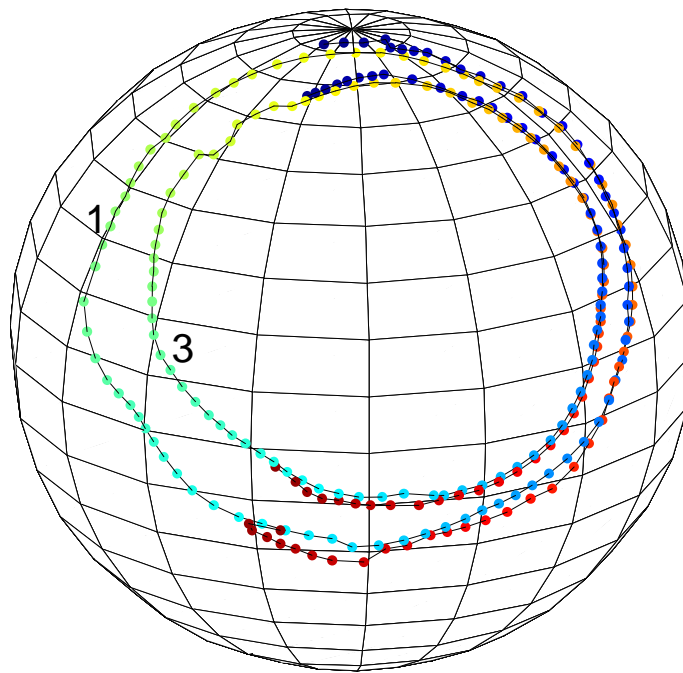


Figure 4.26 PSP measurement result for Fiber No.1 and No.3.

4.4.4 Three-piece PMF

Our experiment parameters are as follows:

- (i) The wavelength span is 1542.9~1556.9 nm (1.748THz) over 128 camera pixel, or 13.6GHz/pixel.
- (ii) The beam size covers 2 pixels.
- (iii) The differential refractive index of the PMF is $\Delta n = 4.15 \times 10^{-4}$.
- (iv) The length of three PMF piece are: 59.3cm, 118.5cm and 83cm.
- (v) As a reference, the fiber splicer gives the angles between the slow birefringence axes: 45° and 125°.

As we have discussed in chapter 2.2.3, because the length measurement error is a non trivial fraction of the beat length (~1 millimeter error comparing with ~ 3 millimeters beat length), the rotation matrix of the second and the third PMF can't be estimated. As a result, we can't derive the accurate PSP and DGD from the PMD vector concatenation rules. The only thing we can check is that the DGD is a periodic function of frequency with the period $\Delta\omega_p = \frac{2\pi c}{\Delta n l_2}$, where l_2 is the length of the second PMF piece. From this

relation, we expect the DGD period for our three-piece PMF is
$$\Delta\omega_p = \frac{2\pi \times 3 \times 10^8}{4.15 \times 10^{-4} \times 1.185} = 3.83 \times 10^{12} \text{ rad} / \text{s}.$$

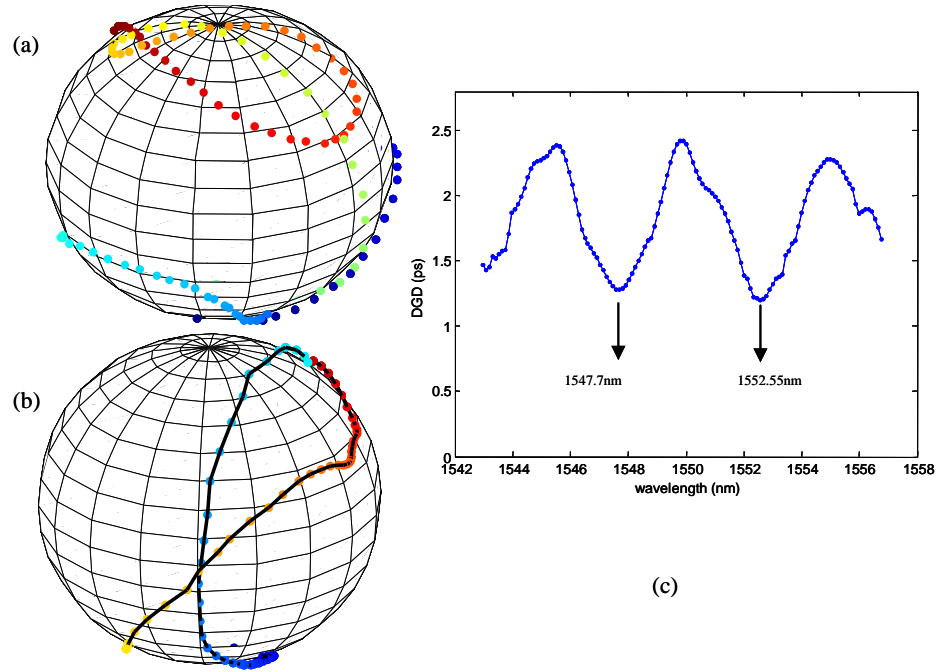


Figure 4.27 Result for three-piece PMF (a)measured output SOP (b) output PSP (c) DGD

Our measurement result is shown in Figure 4.27. (a) shows the output SOP. It traces a complicated curve on the Poincare sphere. The differential SOP is large so that the effect of noise can be reduced, however, the inter-pixel cross talk is more in concern. We apply data fitting ($N=10$) to the output SOP, and calculate PMD vector with differential size $2\Delta\omega$. (b) shows the calculated output PSP. This trajectory is more complex than a circle. (c) shows the DGD. It is approximate to a periodic function as expected. The period is:

$$\Delta\omega_p = 2\pi\left(\frac{1}{\lambda_1} - \frac{1}{\lambda_2}\right) = 2\pi \times 3 \times 10^8 \times \left(\frac{1}{1547.7 \times 10^{-9}} - \frac{1}{1552.55 \times 10^{-9}}\right) = 3.80 \times 10^{12} \text{ rad/s}$$

Comparing to the estimation $3.83 \times 10^{12} \text{ rad/s}$, the error is only 0.8%.

We can estimate the DGD by the PMD concatenation rules only if we know the exact angle between the birefringence axes. This is possible if we perform experiment to calibrate the angle given by the fiber splicer. For example, if we splice two PMF section with the same length, the angle φ (PSP circle has radius $r = \sin \varphi$) is exactly the angle between two birefringence axes.

However, for the concatenation of more than 4 pieces of PMF, the estimation can hardly provide any parameter for comparing. We have to turn to other PMD measurement

method such as Muller Matrix Method (MMM) [17] and the Jones Matrix Eigenanalysis (JME) [5]. These are our possible work plans in the future.

4.5 Discussion

4.5.1 Measurement efficiency

In our scheme, we measure 128 wavelengths in parallel within 80ms and have the potential for 256 wavelengths in parallel within 4ms. Currently, the speed is limited by the computer, which gives slow timing signal to control FLC cells and read data from the camera. If we make a circuit to produce fast timing signal, we can improve the measurement speed significantly. Since the time limit of FLC switching is 100us, and the camera sensing time is a little bit less than 100us, For every output SOP set, we need 1 millisecond to measure (FLC switches 5 times, and take data 4 times.) We measure 4 output SOP sets to get PMD vector, and thus 4 ms is the shortest time we can reach. Moreover, 256 pixels of the camera CCD can be used in the future, thus improving the spectral resolution.

4.5.2 Independence on input SOP

This method calculates the output PMD from the output SOP. The input SOP can be arbitrary as far as they remain the same for all the frequency and almost unchanged within the measurement time. We also don't need to know what the input SOP is. While for Jones Matrix Eigenanalysis [5] people need to choose known input SOPs to measure the transmission matrix first in Jones Space and then calculate PMD from this matrix. Our method is thus more convenient to measure the long-haul optical fiber.

4.5.3 Inter-pixel cross talk

Since the beam size covers two camera pixels, there exists inter-pixel cross talk. The cross talk increases with the increase of SOP difference between two adjacent pixels. Unlike random noise, the SOP measurement error caused by this cross talk can hardly be reduced by data fitting.

4.5.4 PMD measurement limitation

In our scheme, we choose frequency step size $\Delta\omega$ to calculate frequency dependent PMD. However, within this step size, the PMD should reasonably constant. To satisfy this condition, the relation between the mean DGD and the frequency step size is: $\Delta\omega = \frac{\pi}{4\langle\tau\rangle}$ [10]. By this, the largest mean DGD we can measure in our experiment setup is $\sim 9\text{ps}$.

4.5.5 Applications

Our PMD measurement scheme has the following potential applications:

- (i) Mean DGD measurement. Mean DGD is an important parameter to describe the PMD and its effect in optical communication system [10]. We can calculate the mean DGD over the frequency span from the PMD vector measured in our scheme. If we perform the measurement many times in a long period, we can calculate the mean DGD over this period.
- (ii) Second-order PMD. Since we measure the PMD vector as a function of frequency, by differentiating this function, we can get the second-order PMD.
- (iii) All-order PMD compensation. For example, it is potential to compensate all order PMD by rotating the PSP for all frequency to one direction and then compensating the DGD [4].

5. RESEARCH ON PMD BY HIGH-ORDER CORRELATIONS

The stochastic nature of PMD arises from the change in environmental factors such as fiber stress and temperature variations. Here, we investigate to study PMD statistics by the second order and third order frequency correlations and try to extract the information of PMD, and even the post-PMD signal phase by getting the intensity pulse response. Our simulations show that the second order correlations on the output x-direction component of the field intensity, output SOP and output PMD vector contain the information of the mean differential group delay (DGD). While from both simulation and theoretical analysis we show that the x-direction component of the output optical field is not zero-mean circular complex Gaussian distributed.

In this chapter, firstly we introduce the stochastic properties of PMD and our research motivation in 5.1. Then we show the details of our simulation in 5.2. By this simulation tool, we perform second-order correlations in 5.3. Finally, in 5.4, we study the properties of the x-direction component of the output optical field.

5.1 Introduction

5.1.1 Stochastic properties of PMD

In long single-mode fibers, polarization varies randomly from fiber to fiber due to the randomness birefringence caused by intrinsic and extrinsic stress and elliptical core. The extrinsic stress varies with the fiber environment along the length such as pressure and temperature. So PMD varies randomly with carrier frequency and the environment. The stochastic properties of PMD vector is derived by Foschini and Poole [14]. According to their research, the probability density of a component τ_i of PMD vector $\vec{\tau} = (\tau_1, \tau_2, \tau_3)$ is:

$$P_{\tau_i}(\tau_i) = \frac{2}{\pi T} e^{-(2\tau_i/T)^2/\pi}, \text{ Gaussian} \quad (5.1)$$

$$\text{with } E\{\tau_i\} = 0 \quad (5.2)$$

$$\text{and } \sigma^2 = E\{\tau_i^2\} = \frac{\pi}{8} T \quad (5.3)$$

where T is the mean DGD $\langle \Delta\tau \rangle$. These three components of the output PMD vector

are independent and identically distributed (i.i.d.). So the probability density of the length of the PMD vector, or DGD $\langle \Delta \tau \rangle$ ($\langle \Delta \tau \rangle = |\vec{\tau}|$), is Maxwellian:

$$\frac{8}{\pi^2 T} \left(\frac{2x}{T} \right)^2 e^{-(2x/T)^2/\pi}; x \geq 0 \quad (5.4)$$

For such a long fiber, the output SOP is randomly distributed on the Poincare sphere if we give a fixed input SOP for all the frequencies. The x-direction component and y-direction component of the output optical field also varies randomly with frequency. These can be interpreted by Equation (5.5):

$$\begin{bmatrix} E_x(\omega) \\ E_y(\omega) \end{bmatrix}_{out} = \begin{bmatrix} J_{11}(\omega) & J_{12}(\omega) \\ J_{21}(\omega) & J_{22}(\omega) \end{bmatrix} \begin{bmatrix} E_x \\ E_y \end{bmatrix}_{in} \quad (5.5)$$

where the Jones matrix of the fiber varies randomly.

5.1.2 Motivations

We are encouraged by the research on laser speckle via high-order correlations [6,7], and investigate to study PMD by high-order correlations. In laser speckle research, the laser beam is scattered by a random media, and on the image plane the interference of partially coherent beams has spatial fluctuations, and thus forms a field-intensity pattern called speckle pattern. The statistics such as correlations on the speckle pattern carries the information on the scattering media. Especially, the intensity temporal response $P(t)$ of a random media can be obtained by second-order and third-order intensity correlations together, provided that the probability density function of the complex amplitude $E = x + jy$ of the field is a zero-mean Gaussian[6], as shown in Equation (5.6):

$$p_{xy}(x, y) = \frac{1}{2\pi\sigma^2} \exp\left[-\frac{1}{2} \frac{x^2 + y^2}{\sigma^2}\right] \quad (5.6)$$

Equivalently, if we express the complex amplitude in the term of intensity I and phase θ : $E = \sqrt{I} \cos \theta + j\sqrt{I} \sin \theta$, the marginal probability density functions for intensity and phase are:

$$p_I(I) = \frac{1}{2\sigma^2} \exp\left(-\frac{I}{2\sigma^2}\right), I \geq 0 \quad (5.7)$$

$$p_\theta(\theta) = \frac{1}{2\pi}, -\pi \leq \theta < \pi \quad (5.8)$$

These statistical properties of the field enable us to obtain the Fourier magnitude of $P(t)$ by second-order intensity correlations, and the Fourier phase of $P(t)$ by third-order intensity correlations.

Similarly to the random media which causes the speckle pattern, optical fiber with random PMD causes the random properties of output PMD vector, SOP and x-direction component (y-direction has the same properties with x-direction) of the output field. This means that it is potential to extract the information on PMD of the FUT (fiber under test) by the statistical treatment in laser speckle, such as second-order and third-order correlations. So we investigate to apply these high order correlations on PMD by simulation, and the information we wish to extract is the mean DGD $\langle \Delta\tau \rangle$, and the intensity temporal response.

5.2 PMD simulation

We use wave plate model in our PMD simulation. Long fibers are simulated by the concatenation of wave plates with random oriented birefringence axes [10]. We calculate the Jones matrix for all the frequencies. Then we can extract the output PMD vector by Jones matrix eigenanalysis. Moreover, if we give a fixed SOP for all the frequencies, we can calculate the output SOP and the field of x-direction and y-direction components. We realize this simulation many times with different random oriented birefringence axes in each time; so that we can use statistical tools to analyze the output PSP and SOP, and x-direction component of the output field and intensity (y-direction component has the similar properties, so we only choose x-direction component).

The key parameters in our simulation are as following:

- i. Choose N wave plates. Here $N=5000$ or more to make sure the statistics of PMD in our simulation agree with the PMD theory.
- ii. Each wave plate has equal length L . We choose different L to simulate different mean DGD $\langle \Delta\tau \rangle$, because the mean DGD is expected to be [19]:

$$\langle \Delta\tau \rangle = \sqrt{\frac{8N}{3\pi}} \left(\frac{\Delta n}{c} L \right) \quad (5.9)$$

where $\left(\frac{\Delta n}{c} L \right)$ is the DGD of each wave plate.

- iii. The slow axis of each wave plate is randomly oriented. For each realization of simulation we choose different random number set.
- iv. Simulation is realized M times, so that we have enough data to apply statistical data processing

- v. 1024 or more Sample points ω_i in frequency span of 1545nm~1555nm.
- vi. Input vertical polarization for all frequencies

In our simulation, we apply statistics on PMD vector to check this simulation tool. We calculate the PMD vector, and apply statistical analysis on the 500 simulations and over all 1024 frequencies. Thus we have 500×1024 sample points. Figure 5.1 shows the result. We plot the simulation result and the theoretical result together. We choose the mean DGD to be 800fs according to Equation (5.9), and by Equation (5.1) and (5.4) we can calculate the theoretical pdf function of τ_i and $\Delta\tau$, which are the solid curves shown in (a), (b), (c), and (d) respectively. The probability density of these parameters calculated from simulation is expressed by the histograms. We normalize both the simulation and the theoretical result by set their maximum to be 1. We can see that the simulation results match the theoretical result very well, showing that the simulation works.

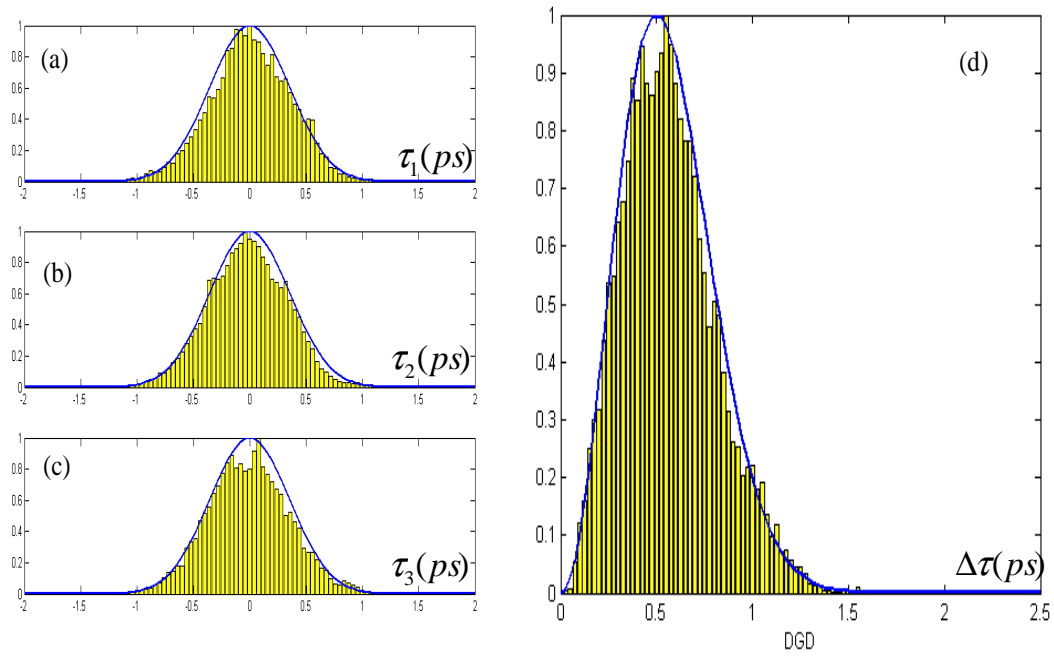


Figure 5.1 The statistical properties of PMD vector extracted from simulation.

5.3 Second-order correlations

Mean DGD $\langle \Delta\tau \rangle$ is an important parameter to describe the PMD of a the optical fiber communication system. The larger is the mean DGD $\langle \Delta\tau \rangle$, the more serious is the PMD in system. We also know that the output parameters, such as output field, output SOP, and output PMD vector, are functions of frequencies. These functions vary with frequencies more intensely if the PMD is larger. Therefore, we investigate the relation between the mean DGD $\langle \Delta\tau \rangle$ and these output parameters via second-order correlation.

By simulation, we apply second-order correlations on the x-direction component field intensity, output PMD vectors, and output SOPs respectively. Then we study if these correlations contain the information of mean DGD $\langle \Delta\tau \rangle$. The parameters chosen in the simulation are as follows:

- (i) Fixed input SOP and intensity for all frequencies
- (ii) 5000 wave plates, 1000 simulations, the stochastic properties of PMD vector from (5.1) to (5.4) are maintained.
- (iii) 4,096,000 points in total. (4096 frequencies in the span 1510nm~1590nm for each simulation).
- (iv) Apply the second-order correlations, and average them over all 1000 simulations
- (v) Choose different $\langle \text{DGD} \rangle$ (1ps, 3ps, 6ps), and repeat (i)~(iv).

5.3.1 Intensity of the x-direction component field

For each of the 1000 simulations, the output x-direction component intensity is a function of frequency fluctuating between 0 and 1. Figure 5.2 (a) shows the intensity spectrum for $\langle \Delta\tau \rangle = 3ps, 6ps$ respectively. We perform second-order correlation on this intensity, and get $\langle I(\omega)I(\omega + \Delta\omega) \rangle$ by averaging $I(\omega)I(\omega + \Delta\omega)$ over all 4096 frequencies and in all 1000 simulations. Figure 5.2 (b) shows the correlations for $\langle \Delta\tau \rangle = 1ps, 3ps, 6ps$ respectively. For each case, there exists a narrow smooth peak near $\Delta\omega = 0$. The width of this pulse is related to the mean DGD $\langle \Delta\tau \rangle$ in this way: the larger is $\langle \Delta\tau \rangle$, the smaller is the width (the FWHM $\Delta\omega_{FWHM}$ for $\langle \Delta\tau \rangle = 1ps, 3ps, 6ps$ is $\sim 3.2 \times 10^{12} rad/s$, $\sim 0.65 \times 10^{12} rad/s$ and $\sim 0.45 \times 10^{12} rad/s$). Though the relation is not strictly inverse proportion, the product $\Delta\omega_{FWHM} \langle \Delta\tau \rangle$ has the magnitude ~ 1 . This can be interpreted by the fluctuation of the intensity spectrum. In Figure 5.2 (a), the fluctuation is more dense for $\langle \Delta\tau \rangle = 6ps$ than for $\langle \Delta\tau \rangle = 3ps$.

According to C. D. Poole's study [19], the density of the crossings on the mean level of the x-direction component intensity spectrum is proportional to the mean DGD. So the small peaks in the spectrum are narrower for larger $\langle \Delta\tau \rangle$. As a result the pulse in the intensity correlation is narrower.

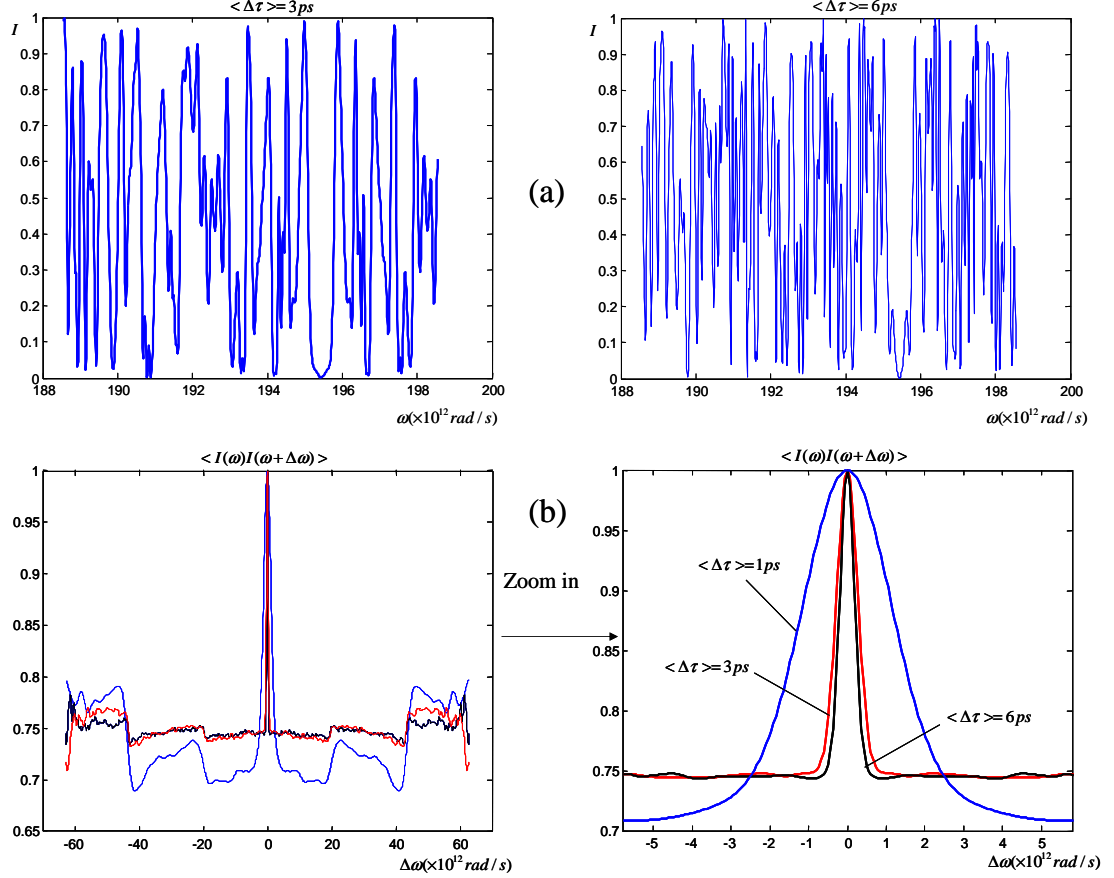


Figure 5.2 (a) x-direction component intensity spectrum for $\langle \Delta\tau \rangle = 3 \text{ ps}, 6 \text{ ps}$ respectively. (b) Second-order correlation of the x-direction component field intensity for $\langle \Delta\tau \rangle = 1 \text{ ps}, 3 \text{ ps}, 6 \text{ ps}$ respectively.

5.3.2 Output PMD vector

We also apply second-order correlation on the output PMD vectors. For the PMD vector $\hat{\tau} = (\tau_1, \tau_2, \tau_3)$, we have two kinds of correlations: $\langle \tau_i(\omega) \tau_i(\omega + \Delta\omega) \rangle$ (where $\tau_i (i=1,2,3)$ is the component of PMD vector) and $\langle \hat{\tau}(\omega) \bullet \hat{\tau}(\omega + \Delta\omega) \rangle$ (The correlation of the dot product of PMD vectors). Since $\tau_i (i=1,2,3)$ are i.i.d., we just choose one of them to study $\langle \tau_i(\omega) \tau_i(\omega + \Delta\omega) \rangle$, say τ_1 . We notice

that, $\hat{\tau}(\omega) \bullet \hat{\tau}(\omega + \Delta\omega) = \sum_{i=1}^3 \tau_i(\omega) \bullet \tau_i(\omega + \Delta\omega)$ so we expect that $\langle \tau_i(\omega) \tau_i(\omega + \Delta\omega) \rangle$ and $\langle \hat{\tau}(\omega) \bullet \hat{\tau}(\omega + \Delta\omega) \rangle$ are close to each other if the maximum of the correlation is set to 1. The simulation result is shown in Figure 5.3 for $\langle \Delta\tau \rangle = 1ps, 3ps, 6ps$ respectively. In both (a) and (b), the larger is the mean DGD $\langle \Delta\tau \rangle$, the narrower is the width of the peak. However, the peaks in (a) are not exactly the same as in (b) as expected. Firstly, the base in (a) has larger fluctuation. Secondly, the peak in the case of $\langle \Delta\tau \rangle = 3ps$ is narrower in (a) than in (b). This is probably due to $\hat{\tau}(\omega) \bullet \hat{\tau}(\omega + \Delta\omega) = \sum_{i=1}^3 \tau_i(\omega) \bullet \tau_i(\omega + \Delta\omega)$, which makes the $\langle \hat{\tau}(\omega) \bullet \hat{\tau}(\omega + \Delta\omega) \rangle$ based on more samples so that it is more smooth and more close to the real value.

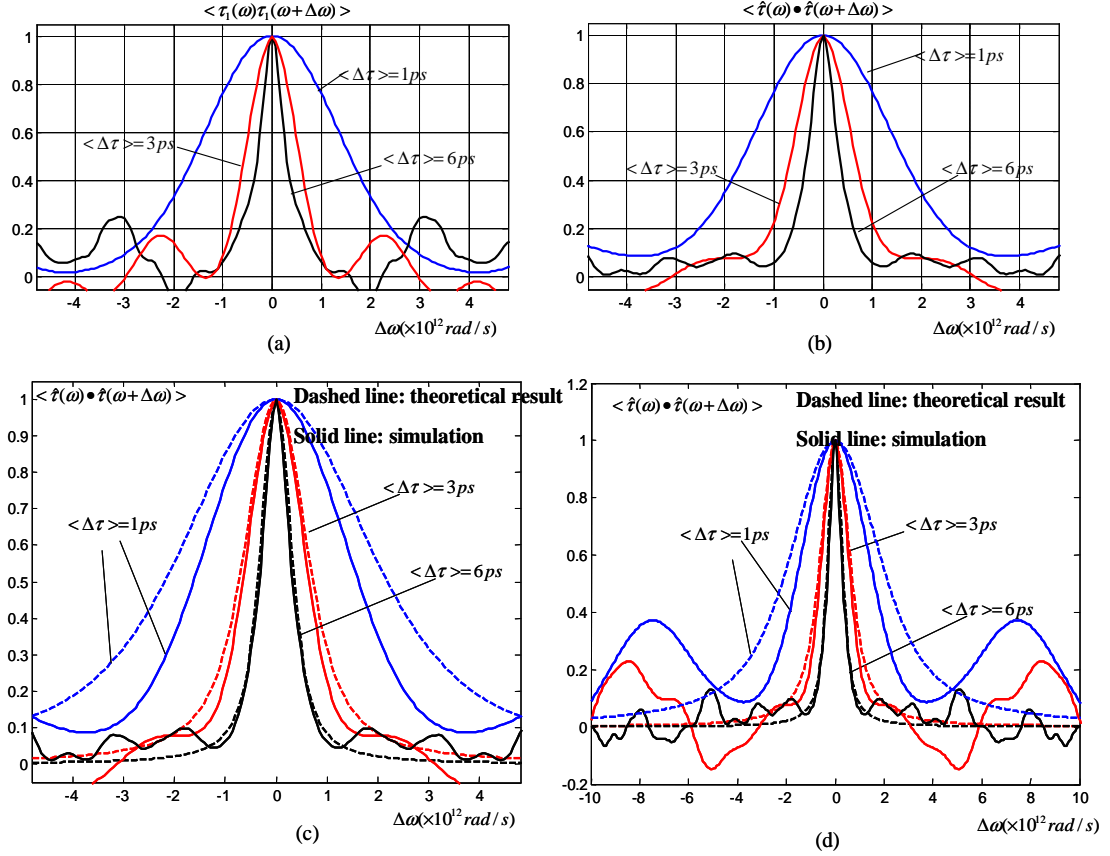


Figure 5.3 The second-order correlations. (a) $\langle \tau_i(\omega) \tau_i(\omega + \Delta\omega) \rangle$ (τ_i is the component of the PMD vector in stokes space) (b) $\langle \hat{\tau}(\omega) \bullet \hat{\tau}(\omega + \Delta\omega) \rangle$ (the second-order correlation on the dot product of PMD vectors.) (c) simulation and theoretical result for $\langle \hat{\tau}(\omega) \bullet \hat{\tau}(\omega + \Delta\omega) \rangle$ (d) the fluctuations on the base.

We notice that Magnus Karlsson [20] and Mark Shtaif [21] have independently derived the theoretical result of $\langle \hat{\tau}(\omega) \bullet \hat{\tau}(\omega + \Delta\omega) \rangle$:

$$\langle \hat{\tau}(\omega) \bullet \hat{\tau}(\omega + \Delta\omega) \rangle = \frac{3}{\Delta\omega^2} (1 - e^{-\langle \Delta\tau \rangle^2 \Delta\omega^2 / 3}) \quad (5.10)$$

In Figure 5.3 (c), we plot the simulation result and the theoretical result together. The simulation result is close to theory result as for $\langle \Delta\tau \rangle = 6ps$, except for fluctuations on the base. The simulation result has noticeable difference for $\langle \Delta\tau \rangle = 3ps$ from the theory. The difference is even larger for $\langle \Delta\tau \rangle = 1ps$. We notice that the larger is the fluctuation on the base of the curve from simulation, the larger is their difference from theoretical result, as shown in Figure 5.3 (d). These fluctuations indicate that the sample number is not enough to get good correlation. This problem would be more serious in experiment if we investigate to extract mean DGD from the second-order correlation of output PMD vectors.

5.3.3 Output SOP

Similarly to PMD vector, we apply second-order correlations on the output SOP vectors ($\hat{S} = (S_1, S_2, S_3)$) to get $\langle S_i(\omega) S_i(\omega + \Delta\omega) \rangle$ (where $S_i (i = 1, 2, 3)$ is the component of the SOP vector) and $\langle \hat{S}(\omega) \bullet \hat{S}(\omega + \Delta\omega) \rangle$ (the second-order correlation on the dot product of SOP vectors). The simulation results for $\langle \Delta\tau \rangle = 1ps, 3ps, 6ps$ are shown respectively in Figure 5.4. The correlations in (a) are very close to the correlations in (b), except that it has a little bit larger fluctuations on the base, just similar to the correlations of PMD vectors. In both (a) and (b), the larger is the mean DGD $\langle \Delta\tau \rangle$, the narrower is the peak width.

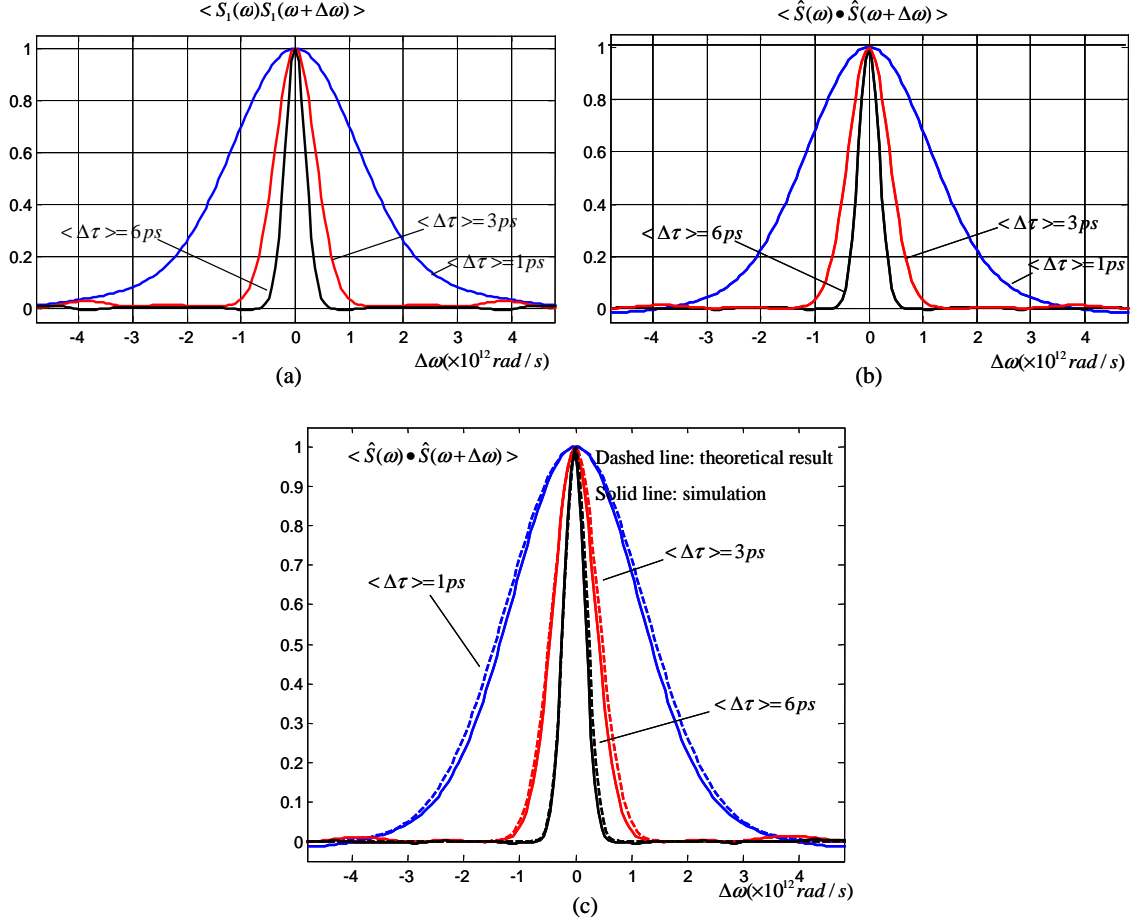


Figure 5.4 The second-order correlations. (a) $\langle S_1(\omega)S_1(\omega + \Delta\omega) \rangle$ (S_1 is the component of the SOP vector in stokes space) (b) $\langle \hat{S}(\omega) \bullet \hat{S}(\omega + \Delta\omega) \rangle$ (the second-order correlation on the dot product of SOP vectors.) (c) Simulation and theoretical result for $\langle \hat{S}(\omega) \bullet \hat{S}(\omega + \Delta\omega) \rangle$.

Magnus Karlsson also derives the theoretical result for $\langle \hat{S}(\omega) \bullet \hat{S}(\omega + \Delta\omega) \rangle$ [22]:

$$\langle \hat{S}(\omega) \bullet \hat{S}(\omega + \Delta\omega) \rangle \sim \exp(-\Delta\omega^2 \langle \Delta\tau \rangle^2 / 3) \quad (5.11)$$

Our simulation result agrees with this equation, as shown in Figure 5.4 (c). Moreover, the fluctuation on the base of the correlations from simulation is almost neglectable. Here the sample number is the same with the PMD vector correlation, but the result is much more close to the theory. Moreover, the output SOP is easier to be measured than the output PMD vector, so the correlation on output SOP vector is more practical to be used to determine $\langle \Delta\tau \rangle$.

5.4 The Properties of the X-direction component of the Output Optical Field

We investigate to use second-order and third-order correlation on the output x-direction component field intensity to extract the intensity temporal response. This is possible only if the output x-direction component field is zero-mean complex Gaussian distributed. So we study the properties of this field first. However, our simulation result shows that the field is not zero-mean-complex gaussian. In order to make a further confirmation, we derive the pdf of the x-direction component of the output optical field and intensity by some reasonable assumptions and knowledge of random variable. This result is consistent with C. D. Poole's research in [19]. So we have to withdraw the plan of applying third-order correlations. However, we make a simple PMD emulator, and measure the output x-direction component field intensity spectrum. In the data processing, the histogram of the intensity shows that it is more close to uniformly distributed than negative exponential distributed. We also apply second-order correlation on the intensity, and the result shows good agreement with the analysis in 5.3.

5.4.1 Simulation

We perform simulation to study the stochastic properties of the x-direction component output field of long fibers with stochastic PMD. The details of the simulation are as follows:

- (i) Fixed input SOP and intensity for all frequencies
- (ii) 5000 wave plates, 1000 simulations, $\langle \text{DGD} \rangle = 30\text{ps}$. Moreover, the stochastic properties of PMD vector from (5.1) to (5.4) are maintained.
- (iii) 4,096,000 points in total. (4096 frequencies in the span 1510nm~1590nm).
- (iv) The histograms on the field, intensity and phase are calculated to show the corresponding pdf.

The simulation results are shown in Figure 5.5. In (a), the pdf of the imaginary and real part of the field are close to each other. A Gaussian function with the same σ^2 ($\sigma^2 = \langle E_r^2 \rangle = \langle E_i^2 \rangle$): $p_x(x) = \frac{1}{\sqrt{2\pi}\sigma} \exp[-\frac{1}{2}\frac{x^2}{\sigma^2}]$ is also plotted, which is quite different from the other two curves. In (b), we show the pdf of the intensity, and it is close to the pdf $P_I(I) = 1, 0 \leq I \leq 1$ (which indicates the uniform distribution), but quite different from the negative exponential function shown in Equation (5.7). In (c), the pdf

of the phase is close to the pdf $P_\theta(\theta) = \frac{1}{2\pi}, -\pi \leq \theta \leq \pi$. In a summary, the output x-direction component field is not a zero-mean circular complex Gaussian distributed as described by equations (5.6)~(5.8).

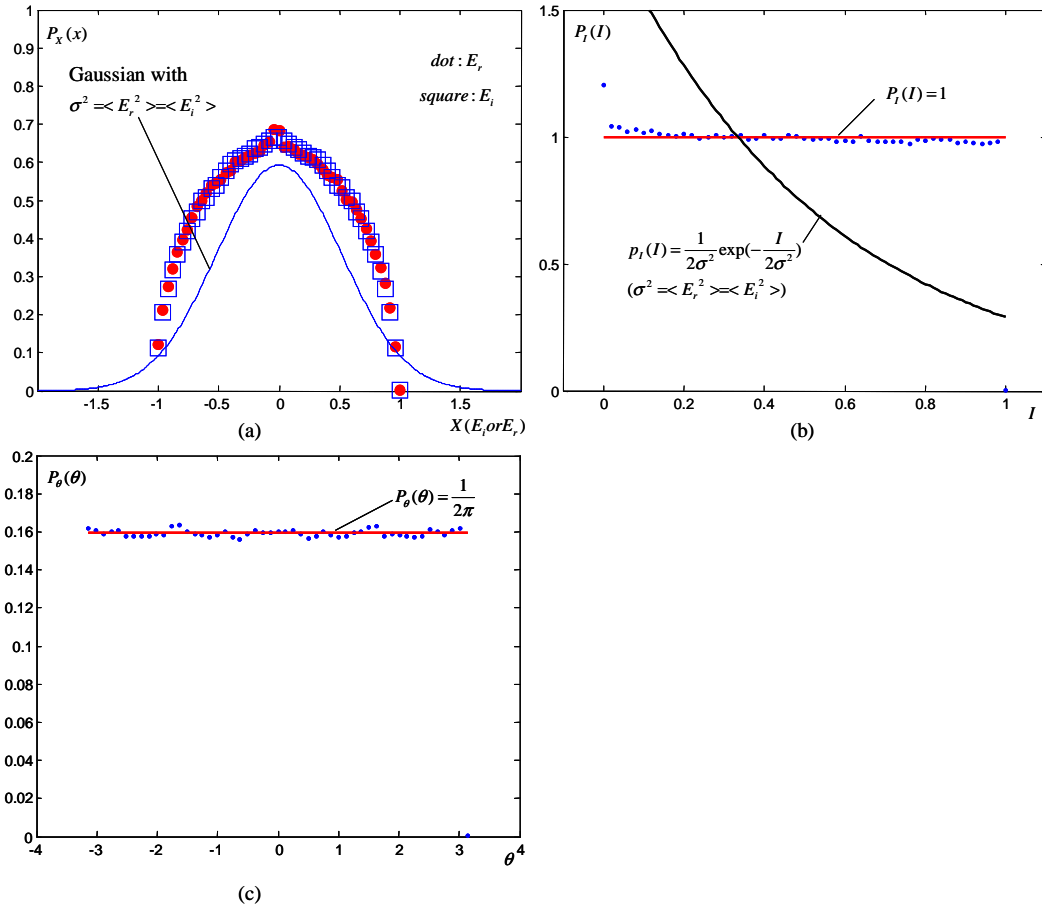


Figure 5.5 Simulation on the properties of the output x-direction component field. (a) pdf of the field: $P_x(x)$, $x = E_r \text{ or } E_i$ (b) pdf of the intensity: $P_I(I)$ (c) pdf of the phase: $P_\theta(\theta)$

5.4.2 pdf of x-direction component field

According to the simulation results, we just assume that:

- (i) pdf of the intensity is:

$$P_I(I) = 1, 0 \leq I \leq 1 \quad (5.12)$$

- (ii) pdf of the phase of the optical field is:

$$P_{\theta}(\theta) = \frac{1}{2\pi}, -\pi \leq \theta \leq \pi \quad (5.13)$$

(iii) the intensity and phase are independent.

We also know that the relation between the field $E = E_r + iE_i$ and the intensity I and θ are:

$$E_r = \sqrt{I} \cos \theta \quad (5.14)$$

$$E_i = \sqrt{I} \sin \theta \quad (5.15)$$

From these relations together with $P_I(I)$, $P_{\theta}(\theta)$ and the knowledge of random variables, we have the pdf of the field:

$$P_x(x) = \frac{2}{\pi} \sqrt{1-x^2}, -1 \leq x \leq 1, (x = E_r \text{ or } E_i) \quad (5.16)$$

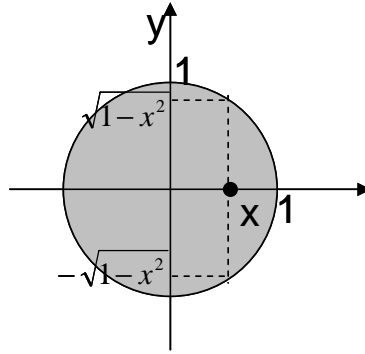


Figure 5.6 (x,y) is distributed in the unit circle

The details of the derivations are as follows [23]:

At first, let $x = E_r = \sqrt{I} \cos \theta$, and $y = E_i = \sqrt{I} \sin \theta$. Obviously, x and y are two functions of two random variables I and θ . We also have:

$$x^2 + y^2 = I \leq 1 \quad (5.17)$$

In the x-y plane, point (x,y) are distributed in the unit circle, as shown in Figure 5.6.

From (i) to (iii), we know that the joint pdf of I and θ is :

$$P_{I,\theta}(I, \theta) = P_I(I) \cdot P_{\theta}(\theta) = 1 \cdot \frac{1}{2\pi} = \frac{1}{2\pi} \quad (5.18)$$

The jacobian of the transformation is:

$$J(I, \theta) = \begin{vmatrix} \frac{\partial x}{\partial I} & \frac{\partial x}{\partial \theta} \\ \frac{\partial y}{\partial I} & \frac{\partial y}{\partial \theta} \end{vmatrix} = \begin{vmatrix} \frac{1}{2\sqrt{I}} \cos \theta & -\sqrt{I} \sin \theta \\ \frac{1}{2\sqrt{I}} \sin \theta & \sqrt{I} \cos \theta \end{vmatrix} = \frac{1}{2} \quad (5.19)$$

So the joint pdf of x and y is:

$$P_{x,y}(x, y) = \frac{P_{I,\theta}(I, \theta)}{|J(I, \theta)|} = \frac{\frac{1}{2\pi}}{\frac{1}{2}} = \frac{1}{\pi} \quad (5.20)$$

Thus we can calculate the pdf of x (y has the same result):

$$P_x(x) = \int_{-\sqrt{1-x^2}}^{\sqrt{1-x^2}} P_{x,y}(x, y) dy = \int_{-\sqrt{1-x^2}}^{\sqrt{1-x^2}} \frac{1}{\pi} dy = \frac{2}{\pi} \sqrt{1-x^2} \quad (5.21)$$

This is just the conclusion in the Equation (5.16), and the derivation is completed.

We plot pdf in Equation (5.16) together with the simulation result of the pdf of E_r and the pdf of E_i in Figure 5.7. They match very well. This not only shows that the assumptions from (i) to (iii) are reasonable, but also shows again that in the simulation, the pdf of the field is not zero-mean circular complex Gaussian, because for zero-mean circular complex Gaussian, the pdf of E_r or E_i should be Gaussian respectively.

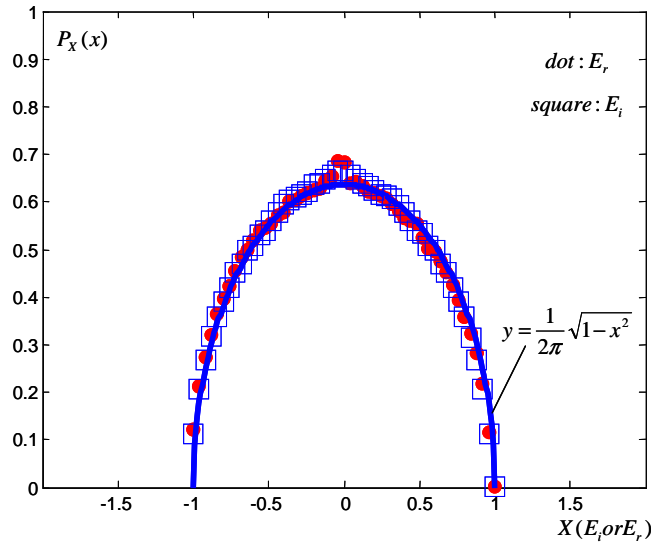


Figure 5.7 pdf of the field. (The dot and square are from the simulation, the solid line is from the derivation.)

We also notice that the PMD measurement scheme invented by C. D. Poole in [19] is based on the assumption that the output SOPs for all frequencies over a long time

period is evenly distributed on the Poincare sphere. By this assumption, the x-direction component field intensity is uniformly distributed [19]. Since this PMD measurement scheme is mature and widely used, the assumption is trustable, and thus $P_I(I) = 1, 0 \leq I \leq 1$ is also trustable. This also proves that the pdf of the x-direction component output field is not zero-mean circular complex Gaussian, because in the latter case $p_I(I) = \frac{1}{2\sigma^2} \exp(-\frac{I}{2\sigma^2}), I \geq 0$.

5.4.3 Experiment

We perform an experiment to study the statistical properties of x-direction component optical field. As shown in Figure 5.8, we use an ASE source and a polarizer to produce a fixed SOP for all the frequencies to a PMD emulator, and then use a horizontal polarizer and an optical spectrum analyzer (OSA) to measure the intensity spectrum for the output x-direction component field. Two collimator pairs in the experiment enable the light source propagate between optical fiber and free space, since the polarizers are free space cells and other components have single mode fiber leads. We also measure the intensity spectrum before the light goes to the PMD emulator, so that we can divide the output spectrum by the input spectrum. After this division, the output spectrum is constant for all frequencies provided that no PMD exists.

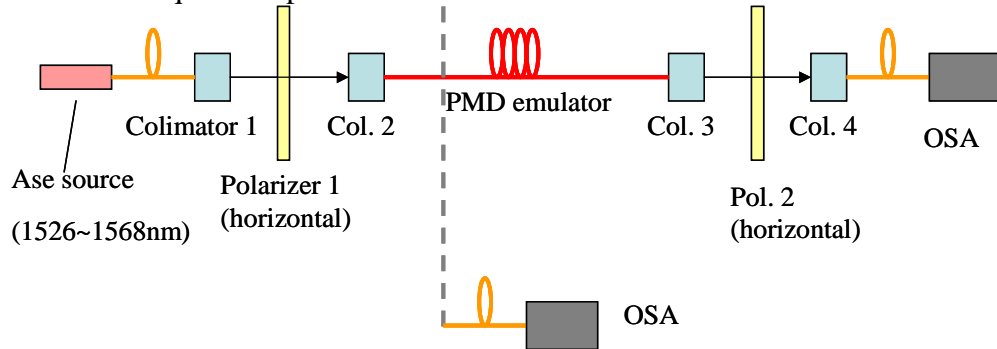


Figure 5.8 The intensity of x-direction component field measurement setup

Our PMD emulator [10] is shown in Figure 5.9. Two 8-piece PMF (slow axis randomly oriented) and one 15-piece PMF (slow axis randomly oriented) are connected by two in-line polarization controllers. The details of the PMF pieces are shown in Table 5.1. The polarization controller can rotate an arbitrary SOP to almost an arbitrary SOP. For a SOP trajectory (SOPs for all frequencies), the polarization controller rotate it as a

whole. This PMD emulator is far from an ideal one, which is supposed to have a large number of PMF sections and polarization controllers. However, when we operate these two polarization controllers randomly, and the PMD of this emulator changes randomly for each frequency, while the mean DGD of the PMD emulator only changed within 5% (estimated by simulation). Moreover, if we give a fixed SOP for all frequencies, the output SOP trajectory has a complicated shape, (as shown in figure 5.10 (a)). When we operate the polarization controller for 100 times randomly, we get 100 SOP trajectories, which cover the Poincare sphere almost evenly, (as shown in Figure 5.10 (b), 20 trajectories). Therefore, we can assume that the pdf of the output x-direction component field intensity is close to what we get in the case the output SOP is evenly distributed on the Poincare sphere.

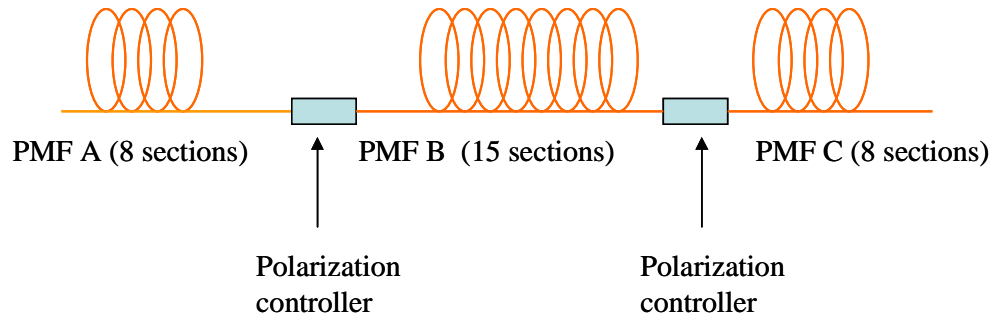


Figure 5.9 PMD emulator

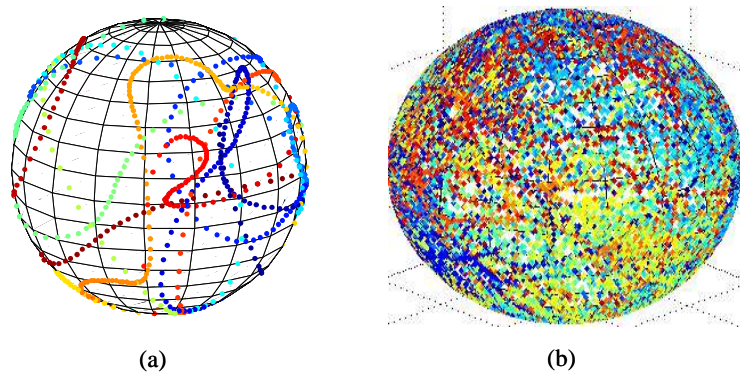


Figure 5.10 Simulation on the emulator (a)one output SOP trajectory (b)twenty output SOP trajectories.

Table 5.1
The details of the PMF sections in the PMD emulator.

PMF A (8 pieces)		
PMF piece	DGD (ps)	Angle offset (°)
1	0.37	-
2	0.45	133
3	0.41	162
4	0.35	73
5	0.48	166
6	0.25	148
7	0.25	39
8	0.22	152
PMF B (15 pieces)		
PMF piece	DGD (ps)	Angle offset (°)
1	0.80	-
2	0.98	122
3	1.50	88
4	1.24	131
5	1.41	169
6	0.75	29
7	1.19	33
8	0.67	156
9	0.85	19
10	1.17	16
11	1.31	112
12	0.91	83
13	0.97	173
14	1.09	56
15	0.57	102
PMF C (8 pieces)		
PMF piece	DGD (ps)	Angle offset (°)
1	0.58	-
2	0.32	77
3	0.39	122
4	0.61	115
5	0.41	138
6	0.50	123
7	0.63	60
8	0.22	94

We measure 1250 frequencies from 1526nm to 1568nm in a single measurement. We change the state of the PMD emulator for 100 times, and perform 100 measurements. As a result, we get 1.25×10^5 intensity measurement points for statistical treatment. Figure 5.11 shows the intensity spectrum of the output field. The blue solid curve and the red dashed curve are the measurements for two different emulator states. They are quite different from each other. From the 1.25×10^5 intensity measurement points in 100 intensity spectrums, we get the histogram of the intensity, as shown in Figure 5.12. This histogram shows that the pdf of the output x-direction component optical field intensity is more close to $P_I(I) = \frac{1}{a}, 0 < I < a$ rather than a negative exponential function.

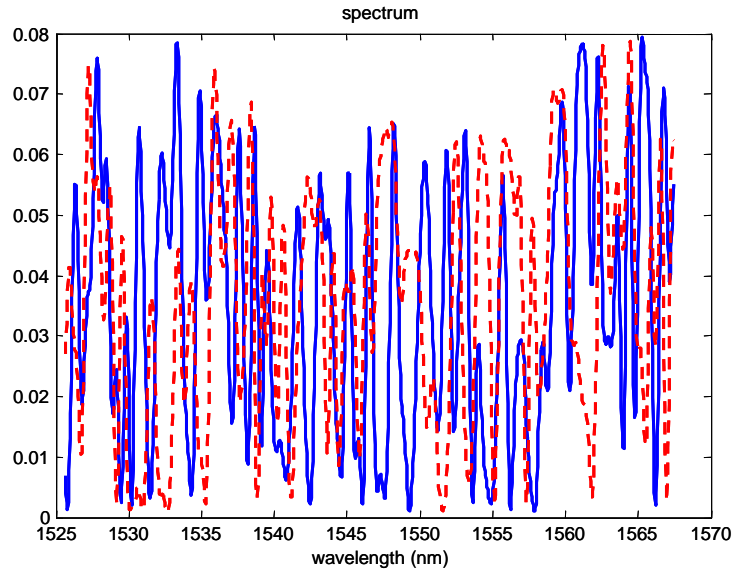


Figure 5.11 The intensity spectrum of the output x-direction component field (The blue solid curve and red dashed curve are measurements for two different emulator states).

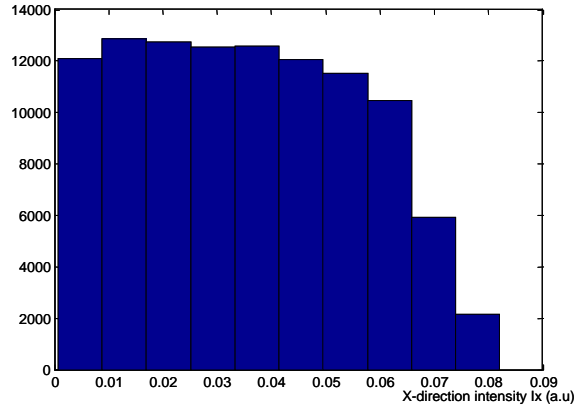


Figure 5.12 The histogram of the output x-direction component intensity

We also perform the second-order correlation on the x-direction component output field intensity, as shown in Figure 5.13. The correlation $\langle I(\omega)I(\omega + \Delta\omega) \rangle$ has a smooth narrow peak around $\Delta\omega = 0$. The FWHM of this pulse is $\Delta\omega_{FWHM} \sim 0.5 \times 10^{12} \text{ rad/s}$. We estimate the mean DGD to be $\sim 7.8 \text{ ps}$ by simulation (The Jones Matrices of PMF A, PMF B and PMF C are calculated according to Table 5.1. The Jones matrices of the Polarization controllers are randomly set for different value in each simulation. So we use concatenation and get the total Jones matrix, and thus obtain DGD for each frequencies in each simulation. By 1000 simulations, we calculate the mean DGD. The average is based on the DGD for all frequencies in 1000 simulations.) The product $\Delta\omega_{FWHM} \langle \Delta\tau \rangle$ is ~ 3.9 , which is of the magnitude ~ 1 as discussed in chapter 5.3.

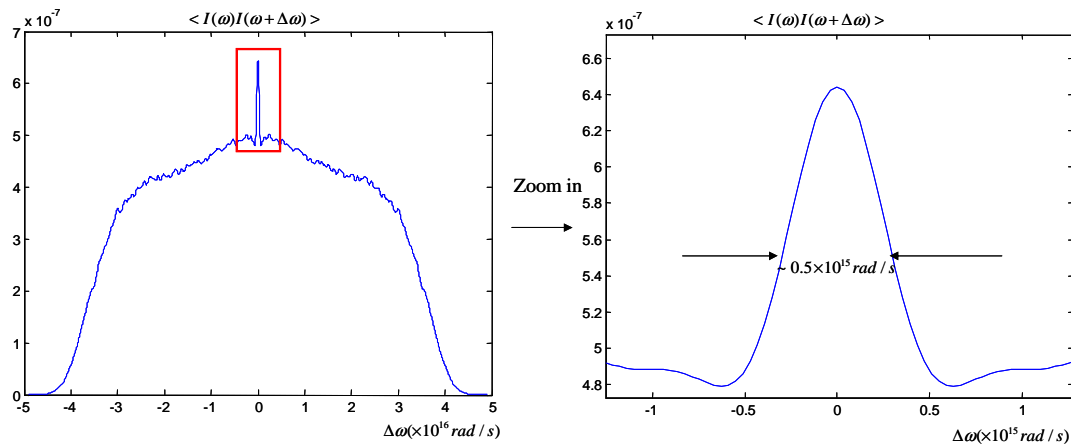


Figure 5.13 The second-order correlation of the x-direction component output field intensity.

6. CONCLUSION

Polarization Mode Dispersion (PMD) limits the bandwidth of high-speed optical fiber communication systems. PMD monitoring becomes important in PMD mitigation and compensation schemes. In this thesis, we demonstrate an efficient scheme to measure PMD vector as a function of frequency, which fully describe PMD of a device. We take advantage of our fast wavelength-parallel polarimeter and allow PMD monitoring on a millisecond scale. This measurement scheme uses our multi-input SOP method, and does not need to know the information of the input SOP. The measurement result has potential applications on the mean DGD measurement and all-order PMD compensation.

We also investigate to study PMD statistics by second order and third order frequency correlations in PMD simulation. We show that the second order correlation on the output field intensity of an arbitrary component (for example, x-direction component), output SOP, and output PMD vector contains the information on the mean DGD. Moreover, it is easier to extract mean DGD from second order correlations on output SOP than the second order correlations on output PMD vector. Furthermore, we study the properties of x-direction component of the output optical field, and conclude that third-order correlation on this field intensity does not give phase of the intensity temporal response.

LIST OF REFERENCES

LIST OF REFERENCES

- [1] F. Heismann, "Polarization Mode Dispersion: Fundamentals and Impact on Optical Communication Systems", *Tutorial*, Presented at European Conference on Optical communications, Sep. 1998.
- [2] X. Wang and A.M. Weiner, "Fast Wavelength-parallel polarimeter for broadband optical networks", *Optics Letters*, Vol. 29, No. 9, 2004, pp. 923-925.
- [3] C. D. Poole, Neal. S. Bergano, R. E. Wagner, and H. J. Schulte, "Polarization Dispersion and Principal States in a 147-km Undersea Lightwave Cable", *Journal of Lightwave Technology*, Vol.6, No.7, July 1988, pp. 1185-1190.
- [4] P. B. Phua, and Hermann A. Haus, "All-Frequency PMD Compensator in Feedforward Scheme", *Journal of Lightwave Technology*, Vol. 22, No.5, May 2004, pp. 1280-1289.
- [5] B.L. Heffner, "Automated Measurement of Polarization Mode Dispersion Using Jones Matrix Eigenanalysis", *Photonics Tech. Lett.*, Vol.4, No.9, 1992, pp. 1066-1069.
- [6] Mark A. Webster, Kevin J. Webb, and Andrew M. Weiner, "Temporal response of a random medium from speckle intensity frequency correlations", *J. Opt. Soc. Am. A*, Vol. 20, No. 11, Nov. 2003, pp. 2057-2070.
- [7] Mark. A. Webster, *Random Media Characterization From Laser Speckle Frequency Correlations*, Ph.D. thesis, ECE Dept. at Purdue University, December 2002.
- [8] C.L. Chen, *Elements of Optoelectronics & Fiber Optics*, Chapter 10, Richard D. Irwin, a Times Mirror Higher Education Group, Inc. company, 1996, pp. 533-583.
- [9] W.A. Shurcliff, "Modern Description of Polarized Light", *Polarized Light, Production and Use*, Harvard University Press, 1996, pp. 15-31.
- [10] Herwig Kogelnik, Robert M. Jopson, and Lynn E. Nelson, "Polarization-Mode Dispersion", *Optical Fiber Telecommunications*, Volume IVB, Chapter 15, Elsevier Science, 2002, pp. 725-860.

- [11] C.L. Chen, *Elements of Optoelectronics & Fiber Optics*, Chapter 8, Richard D. Irwin, a Times Mirror Higher Education Group, Inc. company, 1996, pp. 437-472.
- [12] N. Gisin and J. P. Pellaux, "Polarization mode dispersion: time versus frequency domains", *Optics Communications* 89 (1992) North-Holland, pp. 316-323.
- [13] C. D. Poole and R. E. Wagner, "Phenomenological approach to Polarization dispersion in long single-mode fibers," *Electron. Lett.*, Vol.22, 1986, pp. 1029-1030.
- [14] G. J. Foschini, and C.D. Poole, "statistical Theory of Polarization Dispersion in Single Mode Fibers", *Journal of Lightwave Technology*, Vol. 9, Nov, 1991, pp. 1439-1455.
- [15] J. P. Gordon and H. Kogelnik, "PMD fundamentals: Polarization mode dispersion in optical fibers," *Proc. Nat. Acad. Sci.*, Vol. 97, No. 9, Apr. 25, 2000, pp. 4541-4550.
- [16] S. T. Lagerwall, *Ferroelectric and Antiferroelectric Liquid Crystals* (Wiley-VCH, New York, 1999).
- [17] R.M. Jopson, "Measurement of Second-Order Polarization-Mode Dispersion Vectors in Optical Fibers", *Photonics Tech. Lett.*, Vol.11, No.12, 1999, pp. 1153-1155.
- [18] Mehmetcan Akbulut, *Broadband All order Polarization Mode Dispersion Compensation Using Liquid-Crystal Modulator Arrays*, Ph.D. thesis, ECE Dept. at Purdue University, Aug. 2005.
- [19] C.D. Poole, and David L. Favin, "Polarization-Mode Dispersion Measurements Based on Transmission Spectra Through a Polarizer", *Journal of Lightwave Technology*, Vol. 12, No. 6, June, 1994, pp. 917-929.
- [20] Magnus Karlsson, and Jonas Brentel, "Autocorrelation function of the polarization-mode dispersion vector", *Optics Letters*, Vol.24, No.14, July15, 1999, pp. 939-941.
- [21] Mark Shtaif, Antonio Mecozzi, and J. A. Nagel, "Mean-Square Magnitude of All Orders of Polarization Mode Dispersion and Relation with the Bandwidth of the Principal States", *Photonics Tech. Lett.*, Vol. 12, No. 1, January 2000, pp.53-55.
- [22] Magnus Karlsson, Jonas Brentel, and Peter A. Andrekson, "Long-Term Measurement of PMD and Polarization Drift in Installed Fibers", *Journal of Lightwave Technology*, Vol.18, No.7, July 2000, pp. 941-951.

- [23] Athanasios Papoulis, *Probability, Random Variables, and Stochastic Processes*, Third Edition, Chapter. 6, 1991, pp. 124-148